Fall 11-15-2022

Theoretical Studies of Molecule-Surface Interactions and Dynamics

Yingqi Wang
University of New Mexico - Main Campus

Yingqi Wang

Candidate

Chemistry and Chemical Biology

Department

This dissertation is approved, and it is acceptable in quality and form for publication:

Hua Guo

Martin L. Kirk

Abhaya K. Datye

Yi He

Theoretical Studies of Molecule-Surface Interactions and Dynamics

by

Yingqi Wang

B.S., Chemistry, Shandong University, 2017

DISSERTATION

Submitted in Partial Fulfillment of the
Requirements for the Degree of

Doctor of Philosophy

Chemistry

The University of New Mexico
Albuquerque, New Mexico

December, 2022

ACKNOWLEDGEMENTS

First and foremost, I would like to thank my advisor, Professor Hua Guo, for his continuous support and motivation throughout all these years. Thank you for being patient with me and giving me insightful comments and suggestions. I really learned a lot from you and your advice. I am also grateful for your effort on improving my communication skills, which is important in many aspects of life. Thank you also for creating such a kind and positive environment.

Moreover, I want to thank every member in Professor Guo's group. They helped me with my projects and gave me useful advice. I am really grateful for the fact that everyone is so kind and we all got along every well. I have been fortunate to study under such a relaxed and friendly atmosphere.

I further want to express my gratitude to all my experimental collaborators. They provided useful information and helped me understand the protect from another perspective. I am very lucky to able to participate in such interesting and changeling projects.

I also want to say thank you to all my committee members, Professor Martin Kirk, Professor Abhaya Datye and Professor Yi He. Each brought a different and important prospective to the conversation and made me a better scientist for it.

Last but not least, I am especially thankful to my family for their unconditional love and support.

Theoretical Studies of Molecule-Surface Interactions and Dynamics

by

Yingqi Wang

B.S., Chemistry, Shandong University, 2017

Ph.D., Chemistry, University of New Mexico, 2022

ABSTARCT

Gas-surface scattering involves the conversion of energy in different forms in the impinging molecule, possible bond breaking and forming, and the energy transfer across gas-solid interface. Possible energy dissipation channels include adiabatic energy transfer to the motion of surface phonons and non-adiabatic interactions with surface electron-hole pairs. A complete understanding of the interplay of energy dissipation and physical/chemical changes in the molecule is vital for many important applications such as materials fabrication and heterogenous catalysis.

Gas-surface encounters may occur where non-adiabatic effects are negligible. Two such systems were investigated, both with ample experimental data. One is concerned with the scattering of small molecules, i.e., H_2O, CO_2 and glycine, from a highly ordered pyrolytic graphite (HOPG) surface. Molecular dynamics (MD) simulations revealed that each of the three molecules scattered from the surface via three mechanisms: impulsive scattering, extended impulsive scattering, and trapping. The results showed that the scattering dynamics are heavily dependent on

the strength of molecule−surface interaction. Molecules with a stronger attraction tend to have longer residence times on the surface and consequently experience more translational energy dissipation and vibrational excitation. The other work investigated the interaction of the N atom with the HOPG surface, including the adsorption, diffusion of the N atom and the formation of N_2 through different mechanisms. While N_2 recombination does not have a barrier with Eley–Rideal (ER) pathway, the Langmuir–Hinshelwood (LH) pathway is limited by the diffusion barrier of the adsorbed N atom. The N_2 molecule formed by recombinative desorption is found to be bother translationally and internally hot. These possible pathways and mechanisms are helpful for understanding the hyperthermal collision experiment of atomic nitrogen from HOPG.

We also studied adiabatic and non-adiabatic mechanisms in O atom scattering from HOPG. DFT results suggest that the excited O(^{1}D) binds stronger with HOPG than its ground state counterpart O(^{3}P). As a result, the impinging O(^{3}P) could either stay on the triplet state or crosses over to the singlet state via spin-orbit coupling, leading to different scattering outcomes. To understand the adiabatic and nonadiabatic pathways, two spin fixed potential energy surfaces (PESs) were developed for interaction of the triplet and singlet O with HOPG. The experimental results on O(^{3}P) scattering agree well with MD calculations performed on the triplet PES, which implies that spin conversion is not likely to happen. However, experimental data indicated that the incoming O(^{1}D) beam scatters as O(^{3}P), implying facile spin flip. Our theoretical simulations suggest that O(^{1}D) needs to dissipate enough kinetic energy before it reaches the crossing seam and scatters. The comparisons with experiment help us to gain insight into the nature of interaction of the atomic oxygen with graphene.

In another investigation, we explored the scattering of atomic hydrogen from a semi-conductor surface. Recent experiments on H scattering from the reconstructed Ge(111)-c(2x8)

surface, which is a semiconductor with a band gap of 0.49 eV, found that there are two kinds of scattered H atom in terms of final kinetic energy. The fast channel originates from scattering of H which loses a small amount of energy during the collision, while the slow channel experiences much greater energy loss. We attributed the fast peak to the adiabatic scattering of H atom with surface Ge atoms and MD calculations indeed reproduce the experimental distribution quantitatively. As for the origin of the slow peak, its origin is likely to be related to electronic excitations across the band gap. Indeed, the large energy dissipation only appears when the incidence kinetic energy is larger than the band gap of the semiconductor (~0.49 eV). Hence, it is speculated that this channel is due to nonadiabatic creation of surface electron-hope pairs across the band gap. For such nonadiabatic transitions, the electronic friction model fails to capture the dynamics, as shown by our simulations. These results pose a challenge to the current theoretical models to describe energy transfer from fast nuclear motion to electronic motion.

TABLE OF CONTENTS

CHAPTER 1

INTRODUCTION

Gas-surface interactions play an extremely important role in many industrial applications such as heterogenous catalysis, semiconductor fabrication, and corrosion, which are of great technological relevance.[1] Through gas-surface interactions, different forms of energies are constantly converted into each other, which consequently influences the reaction dynamics such as rection rates.[2-3] Consider a case where an impinging molecule hits the surface, there are various relative or nonreactive paths, as shown in Figure 1. Even with the simplest outcome where the molecule is directly scattered from the surface, there is possible energy transfer between the surface and molecule. The translational and vibrational/rotational energies of the impinging molecule could potentially be transferred to the surface and converted to the vibration of the surface atoms.[4-5] If the molecule dissociates as it approaches the surface, the released reaction energy will immediately be converted into the kinetic energy of the newly formed atoms, which results in 'hot' atoms that have kinetic energy much higher than the surface temperature. This will further bring interesting problems like hot atom diffusion and reaction on the surface.[6-7] If instead of dissociation, the molecule adsorbs on the surface and traps there for a long time, most of its kinetic energy and vibrational energy will transfer to the surface, which leads to thermal desorption at surface temperature.[8] Other than surface phonons excitation, the non-adiabatic electron-hole pairs may also serve as an important channel for energy dissipation.[9-10]

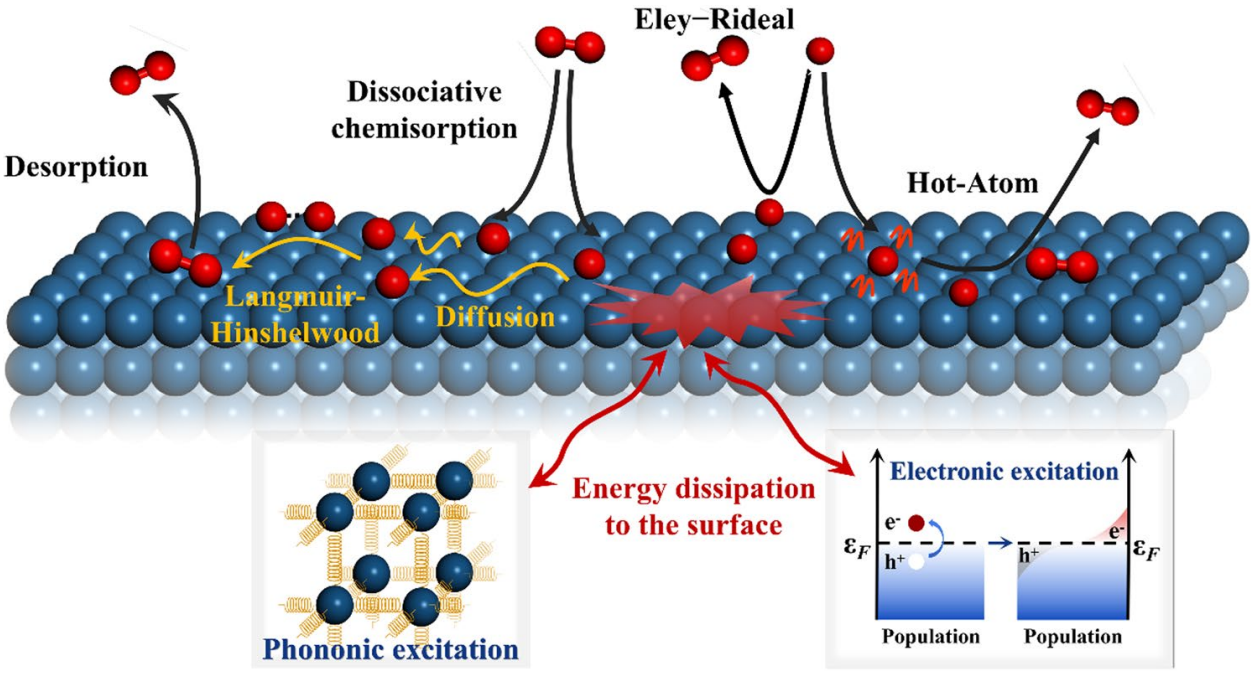

Figure 1. Various elementary processes and energy dissipation channels in gas-surface dynamics, reproduced from Ref. [11].

As mentioned above, adiabatic energy transfer channel is crucial in surface dynamics. At the same time, an increasing amount of experimental work have shown of the importance of non-adiabatic effects and how they can alter the reaction dynamics.[12-19] On metal surfaces, due to the dynamical coupling of the nuclear motion of the adsorbate and the continuous electronic states of metal atoms, the excitation of metal electrons may lead to the breakdown of the most fundamental Born-Oppenheimer (BO) approximation. While the non-adiabatic effect caused by electron-hole pairs is studied both experimentally and theoretically on metal surfaces,[10, 20-21], there are many phenomena related to non-adiabatic effects that cannot be explained by current theory, for example, on semi-conductor surfaces.

This calls for the cooperation between experimentalists and theorists. Even if the constantly developing experimental techniques enable measurements at an astonishingly high resolution, it remains difficult to pin down the exact behavior of each atom and determine the mechanism. This

is why first-principles-based electronic structure calculations and molecular dynamics simulations are particularly important in understanding the underlying mechanisms at the atomic level. One useful approach is to compare calculational results with experimental observations and validate/modify the hypothesis and conclusions based on how well or how bad they agree with each other.

For theorists, to study the energy transfer at gas-surface interfaces, ab initio molecular dynamics (AIMD) simulations based on density functional theory (DFT) is a very useful tool, especially when considering the vibrational degree of freedom of surface atoms. The methodology of AIMD, where the trajectories are generated using forces computed 'on-the-fly' from electronic structure (DFT) calculations, has a profound influence in theoretical research. It allows chemical processes to be studied in an accurate manner. However, as the increase of the size of the system studied and the simulation time, AIMD becomes seriously limited by computational resources since requires repeated DFT calculations. In order to be able to compare with experimental observations, enough trajectories need to be collected to obtain statistical results. This is not feasible for the AIMD approach because it may take a very long time to have all the calculations done. An alternative is to construct high-dimensional analytical potential energy surfaces (PESs) from the DFT data using machine learning. One outstanding advantage of an analytical PES is that the potential energy and forces do not need to be calculated by 'on-the-fly' solving of the Kohn-Sham equation, which saves a great amount of time and enables much faster trajectory calculations.

This thesis is arranged as followed: In Chapter 1, adiabatic dynamics and non-adiabatic effects are introduced. Chapter 2 gives the details of calculation methods used in studies mentioned in the thesis. Chapter 3 and 4 are two studies focusing on the adiabatic dynamics. Chapter 5 and 6 present two projects where on non-adiabatic effects play a decisive role. The thesis finishes with

Chapter 7 which summaries the conclusions of the previous work and provides some outlook about future work.

1.1 Why gas-surface dynamics is important

Chemical reactions at gas-surface interface usually involve different elementary steps, such as adsorption of reactants on the surface, diffusion, reaction and description of products, where molecule-surface interaction and energy flow play important roles. Any detailed understanding of surface reactions requires fundamental knowledge of dynamics and kinetics. Ample evidence exists that dynamics has a significant effect on the reaction activity, particularly in collisions. A good example is the direct dissociative chemisorption of small molecules like CH_4 and H_2O on metal surfaces.[22-24] Experimental evidence demonstrates that excitation in certain vibrational modes of the impinging molecule can more effectively promote the dissociation than other vibrational modes or translational mode, which is a clear sign of mode specific dynamics. For these processes, our knowledge of reactivity is incomplete without an in-depth understanding of dynamics.

Comparing with gas phase reactions, surface reactions are more complex because the surface offers multiple impact sites with different reactivities. The site-dependent reactivity has been reported in CO oxidation[25] and H_2 dissociative chemisorption[26] with state-of-the-art experimental techniques. CH_4 dissociative chemisorption was also found to have site- and incident angle-dependent activity on Pd(110)-(1x2)[27] and Pd(211).[28-29] Another crucial aspect of surface reactions is the energy transfer between the molecular species and surface. On one hand, the kinetic energy of impinging molecule can be mechanically transferred to surface atoms, which results in surface phonon excitations. This mechanical energy dissipation channel does not include excitation of surface electrons, thus within the adiabatic Born-Oppenheimer (BO) approximation.

On the other hand, when the surface electrons are excited by the gas-surface collisions which creates electron-hole pairs (EHPs) on the metal surface, the non-adiabatic energy dissipation channel gains more importance.

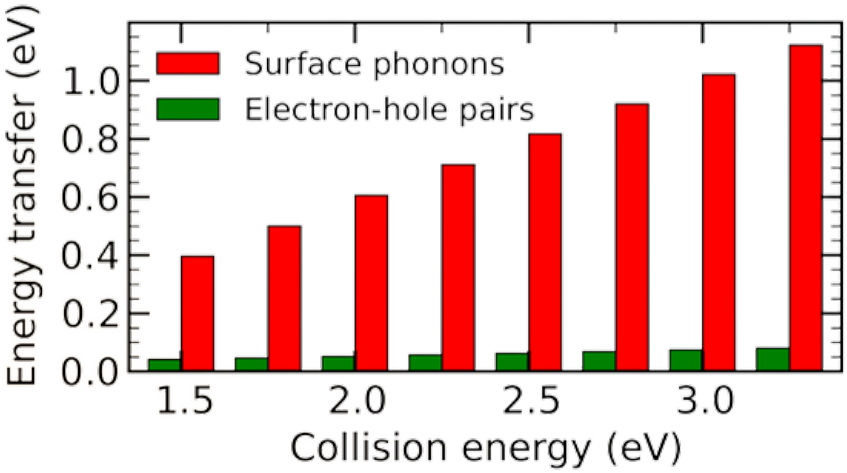

Figure 2. Energy dissipation through surface phonons and electron-hole pairs in the dissociative chemisorption of N_2 on Ru(0001), reproduced from Ref. [30].

Understanding the dynamics of energy exchange and how it affects surface reactions on the atomic level has been a major goal in the past few decades. The relative importance of the two energy dissipation channels varier from system to system. For the dissociative chemisorption of N_2 on Ru(0001) surface, for example, energy exchange with surface phonons has a much stronger influence than EHPs,[30-31] as shown in Figure 2. Energy dissipation to surface phonons also plays a dominant role in the nonreactive chemisorption of H_2 on Pd surfaces.[32-33] The non-adiabatic energy dissipation channel through the excitation of EPHs at metal surfaces was reported to contribute substantially in the inelastic scattering of highly vibrationally excited NO molecules.[34-35] Because of the large electron affinity of NO, the process may involve significant charge transfer and thus be governed by nonadiabatic transitions between the neutral and anionic NO states near the surface.[36-37] Hot H atom diffusion on metal surfaces was found to have their kinetic energies transferred to EPHs more efficiently than surface phonons.[9, 21]

1.2 Adiabatic dynamics

Modern chemistry is largely based on the concept of the adiabatic potential energy surface (PES). BO approximation, which separates the electronic and nuclear degrees of freedom, due to the fact that nuclei are much heavier than electrons, makes the concept of PES possible. The PES establishes a structure-energy relationship so that the potential energy of a molecular system can be mapped out in terms of nuclear coordinates. For many systems, BO approximation gives rather good descriptions. Through classical dynamics calculations on the PES, the evolution of atoms as a function of time gives rise to various measurable attributes such as spectra and reaction probabilities. Due to this reason, gas-surface interaction and dynamics within BO approximation have been studied extensively in the past.

1.2.1 Nonreactive scattering

For nonreactive scattering of molecules from surfaces, the outcome can be categorized into three types, which are single collision, multiple collisions with escape and multiple collisions without escape,[38-39] as shown in Figure 3. These outcomes are often correlated with incident angle, velocity and the coupling strength between the gas molecule and the surface, which are factors affect the energy transfer to the surface. Zhou et al. studied the diglycine collision with highly oriented pyrolytic graphite (HOPG).[40] As a polyatomic molecule, diglycine has several low frequency vibrational modes, which results in a strong attraction with HOPG. This leads to a long residence time on the surface and facile energy loss, particularly along the normal surface. Since the parallel momentum is partially conserved, the scattering angular distribution is found to be generally super specular and the final translational energies are much lower than the values predicted by the so-called hard-cube model.

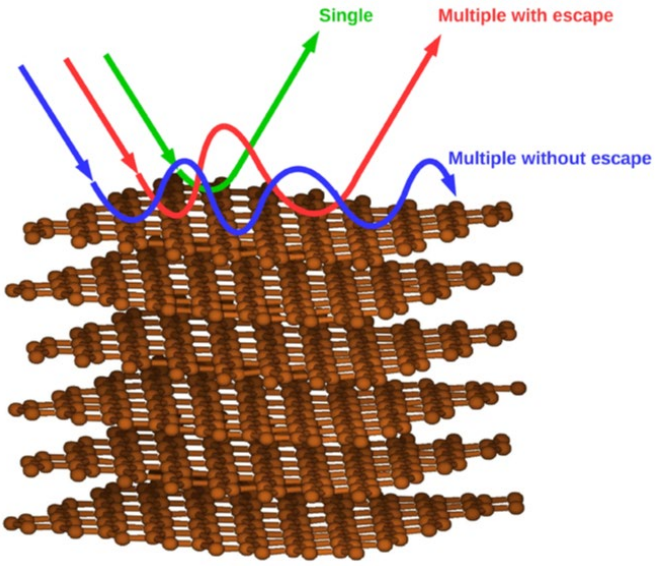

Figure 3. Three types of gas-surface interaction in the non-reactive scattering of N_2 on HOPG, reproduced from Ref. [38].

1.2.2 Eley-Rideal reactions

Bimolecular surface reactions can proceed via two mechanisms, i.e., Langmuir-Hinshelwood (LH) and Eley-Rideal (ER) mechanism. While reactants are thermalized with the surface before they react in the LH type of reaction, ER pathway involves a gas phase species and an adsorbate. It is not hard to see that ER reactions are more dominated by dynamics while LH reactions can generally be treated by statistical theories. In the ER mechanism, there are direct ER reactions where the impinging species engages in a single collision with the adsorbate and the so-called the Hot-Atom (HA) pathway where impinging species hits the surface before reacting. Studies have revealed that direct and HA mechanisms can lead to distinct dynamics signatures. For the D + CD_3* → CD_4 HA reaction,[41] because D atom attacks the adsorbed CD_3* in different directions in the direct and HA pathways, respectively, the produced CD_4 have very different distributions in the CD_4 umbrella vibration.[42]

1.2.3 Recombinative desorption

Dynamics can also be essential for system surpasses the transition state, especially in recombinative desorption. CO oxidation on metal surfaces is known to be a LH reaction between adsorbed CO and O. However, experimentalists have observed both thermal and hyperthermal (translationally and vibrationally hot) CO_2 from CO oxidation on Pt surfaces, which underscores the importance of dynamics.[25] A recent theoretical investigation shed light on the dynamical origin of the bimodal distribution of CO_2.[43] They found that the initially formed CO_2 has a chemisorption well on step sites, which does not exist on terrace sites, as shown in Figure 4a. The chemisorption well on a step site traps CO_2 for a period of time, which allows energy transfer between CO_2 molecule and the Pt surface, leading to low translational energies and a broad angular distribution. On the other hand, CO_2 produced on the terrace site desorbs directly after formation with high translational energies near surface normal. This is illustrated in Figure 4b. Sudden Vector Projection (SVP) model,[44-45] which predicts the energy disposal into a product mode by the overlap of the corresponding normal mode with the reaction coordinate at transition state, shows that CO_2 desorbs from step site is highly internally excited, which is indeed the case. The inner energy distribution is given in Figure 4c.

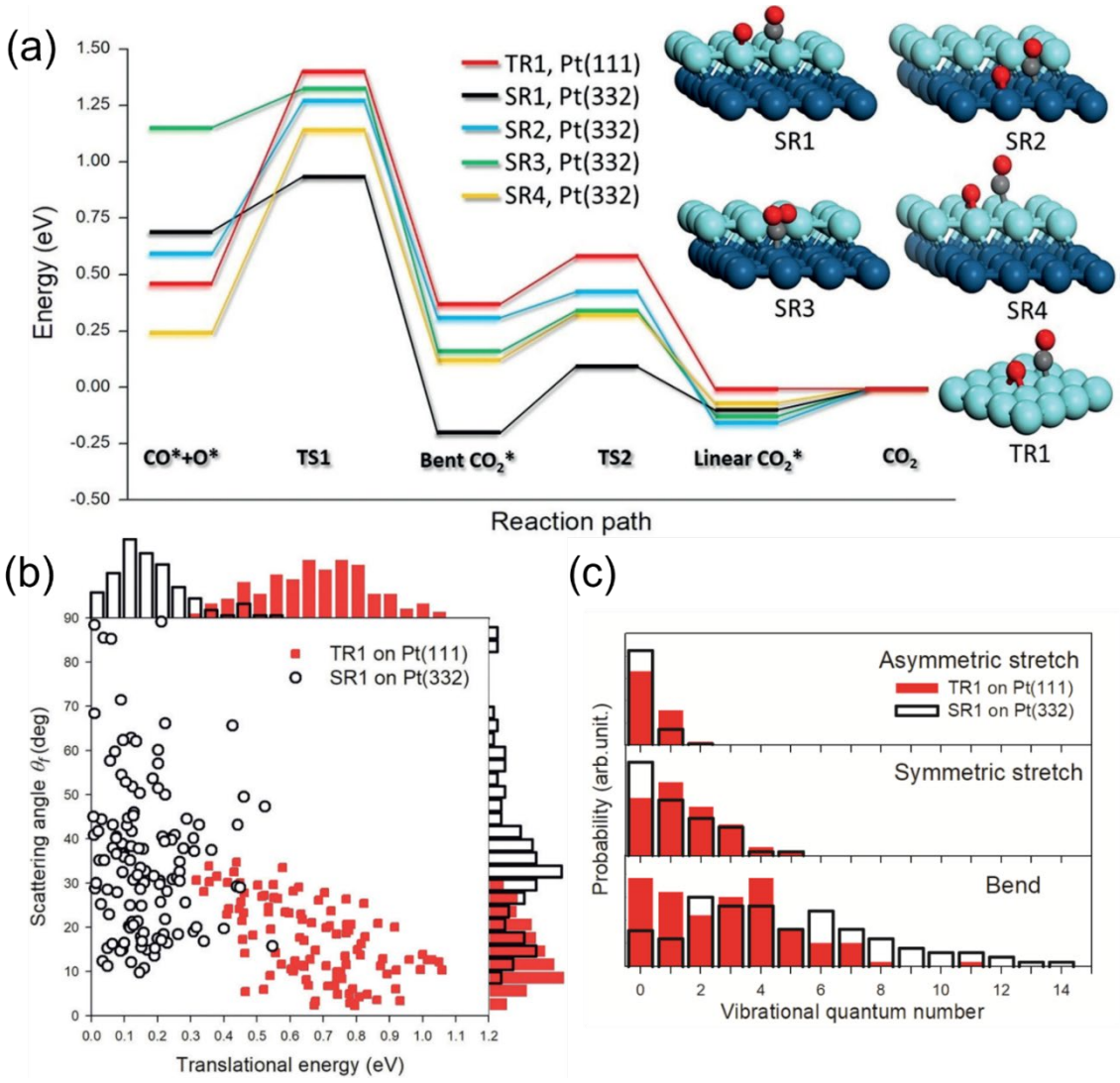

Figure 4. (a) Energetics of various reaction paths for the oxidation of CO on Pt surfaces (relative to CO_2 + Pt asymptotic limit). TR and SR are short for terrace and step reaction, respectively. (b) Translational and angular distributions of the CO_2 product. (c) CO_2 vibrational distributions. Reproduced from Ref. [43].

1.3 Non-adiabatic effects

Despite the fact that BO approximation works well in most cases, there is emerging evidence on the breakdown of BO approximation in gas phase atomic and molecular collisions. The most representative one happens in systems where there are multiple intersecting PESs. If the states have the same symmetry, the crossing is forbidden by quantum mechanics. Atom-atom

collision is usually the simplest situation since the PESs are one-dimensional curves. Consider the formation of NaI ion through the collision of two neutral atoms Na and I, e.g., $Na + I \rightarrow Na^+ + I^-$, whose potential energy curves are shown in Figure 5. When Na and I atom are far away from each other, the ionic curve is above the neutral curve. The collision process includes two curves, i.e., ionic and covalent curve. When the distance between Na and I atom is larger than 6.93 Å, they proceed on the neutral curve. When they reach the distance of 6.93 Å, they can either proceed adiabatically and switch to the ionic curve or proceed non-adiabatically and stay on the neutral curve. After reaching the inner turning point, they will again cross the avoided crossing at 6.93 Å, facing the same choice.

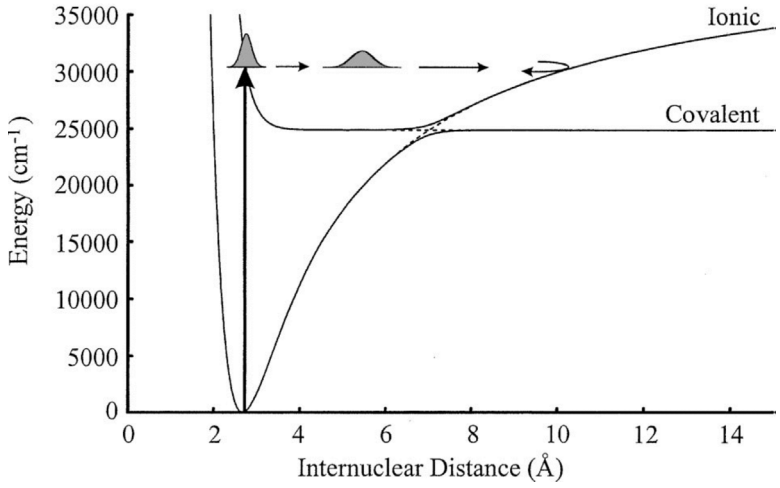

Figure 5. Potential energy curves for NaI, reproduced from Ref. [46].

An approximate expression for p, which is the probability of making the non-adiabatic transition at the crossing point, developed by Landau, Zener and Stueckelberg is given as,[47-48]

$$p = \frac{\frac{2\pi}{\hbar} H_{12}^2}{d/dR|V_{ion} - V_{neut}|v_R} \quad (1)$$

where H_{12} is the coupling matrix element between the neural and ionic curves, V_{ion} and V_{neut} are the ionic and neutral potential curves, and v_R is the radial velocity. This theory has been proved to generate consistent results with numerous measurements of charge transfer collisions.[49]

1.3.1 Electron-hole pairs

For metal surfaces, which have a continuum of electronic states and can generate electron hole-pairs near the Fermi level, Born-Oppenheimer approximation becomes questionable. The interaction between molecules and electron-hole pairs at metal surface results in a continuum of excited states. This leads to an infinite amount of curve crossings and non-adiabatic effects could play a key role.

Below in Figure 6 are two examples where the excitation of electron-hole pairs affects signicantly the gas-surface dyanmics on metal surfaces. The left panel exhibts the results of H atom scattering from bare (blue line) and Xenon-covered (red line) Au(111) surfaces. In the experiment, the H atom hits both surfaces with an incidnet enrgy of 2.7 eV, and the enrgy loss after collision with Xe-covered Au(111) surface is very little while that with clean Au(111) surface is much greater. This can be explained by the fact that the Xenon–covered surface can only take up energy in form of phonons, which results in final kinetic energy almost the same as incidence energy. For the bare Au(111) surface, however, the energy can also be transferred non-adiabatically to electron-hole pairs, which is proved to be rather strong since a large portion of translational energy is lost.[10]

In the right panel, the hot hydrogen atoms diffusion resulting from the dissociative chemisorption of H_2 was invertaiged on single Pt atom embedded Cu(111) surface, and the energy disspaition of H atom through surface phonons and electron-hole pairs E_{ehp} were plotted.[21] Specically, E_{ph}= E_{sk}+ E_{sp}, where E_{sk} and E_{sk} are the kinetic energy and potentail energy change

caused by the lattice distortions, respectively. It clearly shows that the strong interaction with surface electron−hole pairs contributes signicalntly in the rapid energy dissipation of hot H atom diffusion.

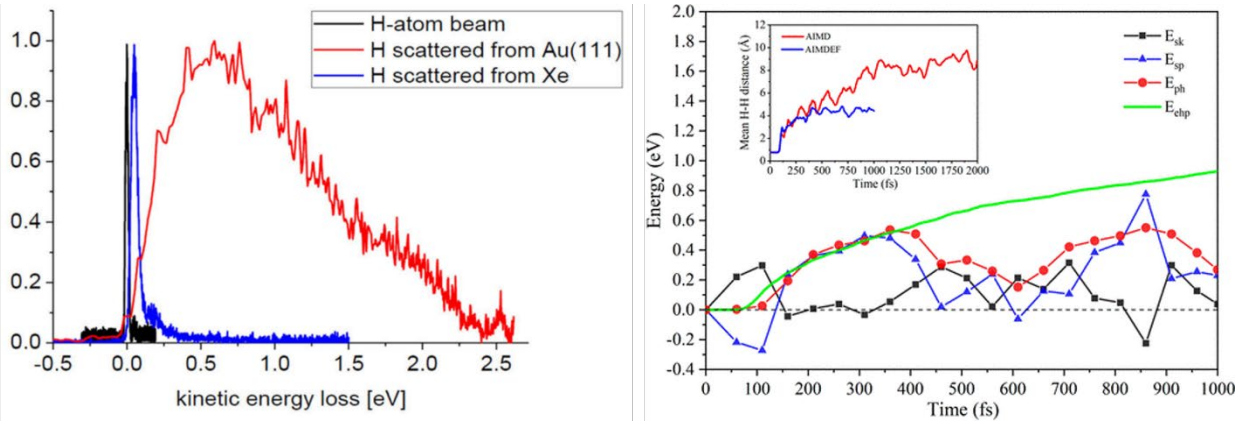

Figure 6. Two experiments showing how electron-hole pairs affect the surface dynamics on metals, reproduced from Refs. [10, 21].

Here I will introduce how to quantify the non-adiabatic effects caused by the electron-hole pairs using the widely accepted electron friction model.[50-51] When impinging molecule gets closer to the metal surface, its kinetic energy can easily excite electrons near Fermi level and create electron-hole pairs. The energy loss is modeled by a friction force. In this model, the classical dynamics is represented by the following generalized Langevin equation,[9]

$$m_i \frac{d^2 \boldsymbol{R}_i}{dt^2} = -\frac{\partial V(\boldsymbol{R}_i)}{\partial \boldsymbol{R}_i} - \eta_i(\boldsymbol{R}_i)\frac{d\boldsymbol{R}_i}{dt} + F_i \qquad (2)$$

where the second term on the left-hand side is the electron friction and third term is the random force, which accounts for the thermal fluctuation at the given temperature. As seen from the equation, the electron friction is controlled by two factors, one is the friction coefficient which is dependent on the coordinates of a nucleus and the other is its velocity. The atomic friction coefficient was calculated based on the local-density friction approximation (LDFA),[50, 52-53] where

the electron density at the atomic coordinate decides the coefficient. In the following equation, k_F is the Fermi momentum and ρ is the electron density of clean metal surface at position $\boldsymbol{R}_i$:

$$\eta_i = \frac{4\pi\rho}{k_F}\sum_{l=0}^{\infty}(l+1)sin^2[\delta_l^i(k_F) - \delta_{l+1}^i(k_F)] \quad (3)$$

The phase shifts were provided in a previous paper.[54]

1.3.2 Spin transitions

According to equation (1), if the velocities are low or the coupling is strong, the system will follow the adiabatic state. Nonetheless, with high velocities or weak coupling, the diabatic transitions can be significant. The importance of non-adiabatic transitions is not restricted to atomic collisions. It has been shown that the energy dependence of the initial sticking probability of molecular oxygen (O_2) on the Si surfaces may be explained by a hindered spin-flip from the triplet ground state of the free oxygen molecule to the singlet ground state of the adsorbed atoms, because the probability of a change of the spin state, which would be required for an adiabatic approach to the surface, is very low.[55-56]

In another example, O_2 dissociation on Al(111) was not well understood for a long time. Different experimental groups have obtained consistent results that the initial sticking probability of O_2 is rathe low (~2%). In experiment, the measured initial sticking probability distinctly displays a 'S' shape, suggesting that the underlying mechanism is activated.[57] That is to say, possible pathways that lead to dissociation are energetically hindered by a barrier. Adiabatic DFT calculations, on the other hand, found that the O_2 dissociation is a barrierless process on Al(111).[58] As a result, molecular dynamics studies yield a sticking coefficient of almost 100% based on such an adiabatic PES, which contradicts experimental observation.

If we consider the spin change during this process, when the O_2 molecule and the surface are separated, they are in an overall triplet state since the ground state of the O_2 molecule is triplet. When the surface is oxidized, the overall spin becomes singlet, this means a spin-transition must occur somewhere when O_2 approaches the surface. To study the role of O_2 spin on this system, Behler et al. built a triplet PES for this system using a constrained DFT method and found that there are clear barriers towards dissociation, as shown in the left panel of Figure 7.[59] Their molecular dynamics calculations successfully reproduced the 'S' shape of sticking coefficient based on this special PES by invoking the spin-flipping mechanism. The results are displayed in the right panel of Figure 7.

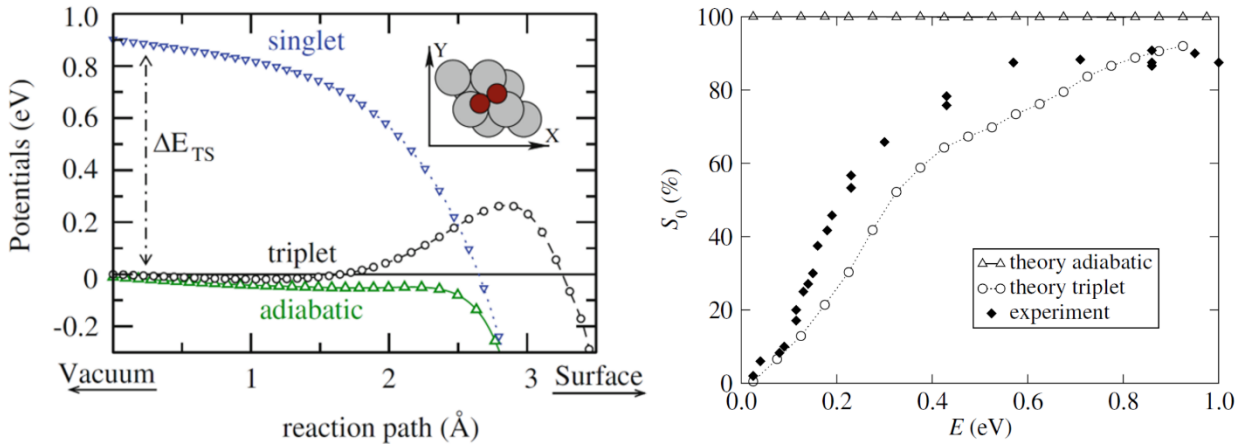

Figure 7. (left) The minimal energy pathway in the triplet state and the corresponding adiabatic and singlet potential over fcc site, reproduced from Ref. [60]. (right) The sticking coefficient calculated from molecular dynamics on the adiabatic and triplet PES, reproduced from Ref. [59].

Despite the good agreement with experiments, the spin-flip mechanism has been challenged by Carter and coworkers.[61] They found that, by applying embedded correlated electron wave functions, the physics of the interaction of O_2 with the metal surface can be correctly described and the correct barriers arise naturally on the adiabatic PES. With semiempirical potentials, it has been shown that there is non-adiabatic charge transfer from the surface to O_2.[62]

However, the intrinsic deficiencies within the generalized gradient approximation (GGA), such as the self-interaction error and the lack of derivative discontinuities,[63-64] produce over-delocalization of electrons and leads to an inaccurate description of the charge transfer between O_2 and Al surface. To better describe the charge transfer process, the correlated wave function methods need to be employed for the entire system, which is too computationally demanding. Consequently, an embedding theory was prosed,[65] where the interaction between O_2 and nearby Al atoms at possible adsorption sites, which is noted as 'embedded cluster' in the left panel of Figure 8, is treated by complete ab initial calculations, and the rest surface Al atoms, noted as 'extended surface', are treated by Kohn–Sham DFT. The correct evaluation of charge transfer with a correlated wave function theory manifests that there is no need to introduce a spin-flip model.

Following the static analysis of reaction pathways, dynamics study was carried out on the dissociative chemisorption of O_2 on Al(111) surface.[66] A full-dimensional PES was constructed with the embedded correlated wave function (ECW) method. The right panel of Figure 8 elucidates that the sticking probability generated from ECW method match well with experiment. In detail, they reproduced the observed translational energy dependence and the steric effects of O_2 molecule.

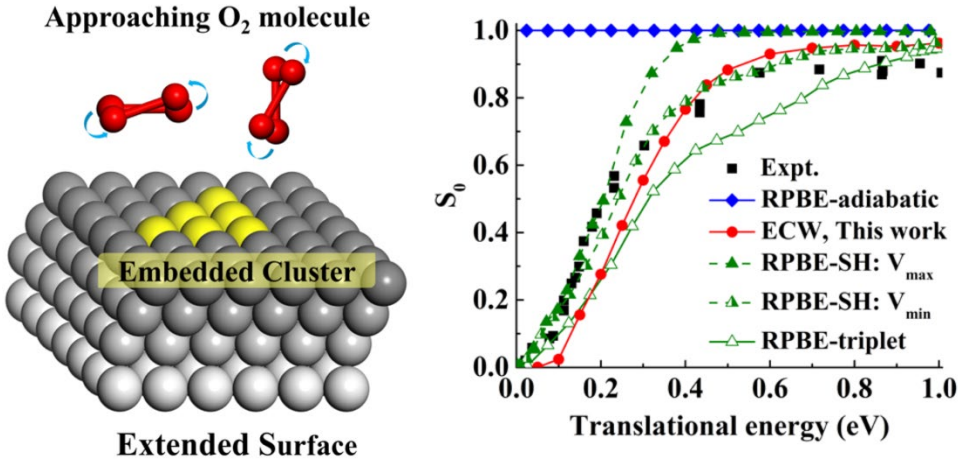

Figure 8. (left) Scheme of O_2/Al(111) system within ECW method. (right) The sticking probability from calculations using different methods and from experiment. Reproduced from Ref. [66].

CHAPTER 2

THEORY AND METHODS

2.1 Force Field

A major task for computational chemistry is to calculate the electronic energy for given geometry to build a potential energy surface (PES). Depending on the properties of the system, the level of accuracy desired, and the computational resources available, different methods were used to study the problem. The force field methods simplify this process by representing the PES using a parametric function of the coordinate of each atom in the system. Therefore, the basic units in force filed methods are atoms, rather than electrons, which means all the electronic quantum effects are neglected. To simulate atoms and the bonds that hold them together, a "ball and spring" model was employed.[67-68] Force fields are thus also called molecular mechanics (MM) methods.

The foundation of the force field method is the transferability of atom type, which originates from the fact that same chemical unit generally acts similarly in different molecules. For example, all C-H bonds have roughly the same bond length and the same stretch vibrational frequency in any molecules. For this reason, parameters for the same element in same chemical environment can be transferred in different molecules and do not need to be refitted every time a new system is studied, which saves a great deal of time and computational resources. The idea of molecules consisting of some suturally similar combinations of atoms which perform similarly is implemented in force field methods as atom type.

The force field energy of a system can be described as followed,

$$E_{system} = E_{str} + E_{bend} + E_{tors} + E_{vdw} + E_{el} + E_{cross} \quad (1)$$

where E_{str}, E_{bend} and E_{tors} are the energy function with respect to the stretch of a bond, bend, and rotation around a bond, E_{vdw} and E_{el} are non-bonded interactions, and the last term describes the coupling between the first three terms. The stretching and bending terms are often expressed as a Taylor expansion at the equilibrium bond length and bond angle, terminated at second order, as seen in the following equation. Take the stretching energy as an example, the energy function can be written as,

$$E_{str}(R^{AB} - R_0^{AB}) = E(0) + k_{AB}^1(R^{AB} - R_0^{AB}) + \frac{1}{2}k_{AB}^2(R^{AB} - R_0^{AB})^2 \quad (2)$$

where R^{AB} is the bond length between two atom types A and B, R_0^{AB} and $E(0)$ are the bond length and potential energy at equilibrium position, respectively.

Similarly, the bonding term can be expressed as,

$$E_{bend}(\theta^{ABC} - \theta_0^{ABC}) = \frac{1}{2}k_{ABC}(\theta^{ABC} - \theta_0^{ABC})^2 \quad (3)$$

This harmonic form is probably the simplest but most time sufficient to characterize the stretching and bonding properties of atoms at low temperatures. If significant error exists between calculations and experimental measurements, higher orders of Taylor expansion can be included to increase the accuracy and make up the gap.

For the torsion term, because molecular rotations often lead to periodic change of energy, Fourier series are often used to provide the periodicity,

$$E_{bend}(\omega) = \sum_{n=1} V_n \cos(n\omega) \quad (4)$$

where $n = 1$ represents a rotation that is periodic by 360° and $n = 2$ represents a rotation periodic by 180° and so on. V_n determines the barrier for rotating a certain degree around a certain bond. Take the ethane molecule as an example, there are two possible conformations in terms of internal rotation along the central C-C bond. One is staggered conformation, where the hydrogen atoms

are staggered relative to each other, corresponding to an energy minimum, and the other is eclipsed conformation, where hydrogen atoms from each carbon are overlapped, representing an energy maximum. For ethane, the $n = 3, 6, 9$ etc., since the three hydrogen atoms from each carbon are identical.

For the long-range van der Waals interaction, it is zero when two molecules or atoms are far enough, it starts to become attractive as two molecules or atoms approach each other, because of the induced dipole-dipole interaction, and then becomes reclusive when the distance is too small, due to the overlap of electron clouds (Pauli repulsion). A popular function that is suitable for the dispersion force is the Leonard-Jones potential, which can be written as,

$$E_{LJ}(R) = \varepsilon\left[(\frac{R_0}{R})^{12} - 2(\frac{R_0}{R})^{6}\right] \quad (5)$$

where R_0 is the intermolecular distance at the minimum energy ε.

The other part of the non-bonded energy is electrostatic energy, which comes from charges and permanent multipoles. The interaction between point charges is given by the Coulomb potential, which is modified in different versions of force field methods to better fit the experimental data.

Finally let us talk about the crossing term, which is common in many force fields. Take H_2O molecule as an example, when the angle is compressed, the optimal bond length will change accordingly, based on electronic structure calculations. It is therefore necessary to include this coupling term in the expression of total energy in force field methods. The main component of the crossing energy is the coupling between starching and bending, which can be written as,

$$E_{str/bend} = k^{ABC}(\theta^{ABC} - \theta_0^{ABC})[(R^{AB} - R_0^{AB}) - (R^{BC} - R_0^{BC})] \quad (6)$$

Reactive force field (ReaxFF)[69] is used in one of my projects discussed below. Unlike traditional force fields which are not able to describe the bond breaking and formation, ReaxFF

overcomes this disadvantage by introducing the concept of bond orders. For ReaxFF, the bond energy is directly related to the bonder order between a pair of atoms which is determined by the distance between the two atoms. Thanks to the concept of bond order dependent bond energy, ReaxFF can be used to describe the formation and dissociation of chemical bonds, where the bonding energy would not become unrealistically large when the bond distance is stretched apart, as in many nonreactive force fields where the harmonic oscillator model is used. For the nonbonded part of the potential, Coulomb and Morse potentials are employed to describe the Coulomb force and van der Waals force, respectively. When the bond distance is short as in bonded atoms, the repulsion caused by the two forces is excessively high, a shielded interaction is thus used at short range to avoid the problem.

2.2 Density Functional Theory

If we want to describe the PES in a global sense, force field methods are not appropriate. Given that electrons are very light particles, quantum mechanics is needed to describe the electron structure which determines the chemical properties. Throughout the past few decades, density functional theory (DFT) has been a powerful and widely used tool in quantum chemistry and computational physics. DFT computes the ground state energy from the electronic density of the system, which is a three-dimensional function, greatly reducing the degree of freedom in the calculation.

2.2.1 Many-body problem

For a molecular system, the main goal is to solve the Schrödinger equation,

$$\hat{H}\Psi = E\Psi \tag{7}$$

where Ψ is the wave function, $\hat{H}$ is the Hamiltonian operator and E is total energy of the system.

In atomic units, the total Hamiltonian for a system containing M nuclei and N electrons can be written as

$$\widehat{H} = -\frac{1}{2}\sum_{i=1}^{N}\nabla_i^2 - \frac{1}{2}\sum_{A=1}^{M}\frac{1}{M_A}\nabla_A^2 - \sum_{i=1}^{N}\sum_{A=1}^{M}\frac{Z_A}{\boldsymbol{r}_{iA}} + \sum_{i=1}^{N}\sum_{j>i}^{N}\frac{1}{\boldsymbol{r}_{ij}} + \sum_{A=1}^{M}\sum_{B>A}^{M}\frac{Z_A Z_B}{\boldsymbol{r}_{AB}} \qquad (8)$$

Briefly speaking, the first two terms represent the kinetic energy of all electrons and nuclei in the system, and the last three terms describe the potential energy between the particles, which include the electron-nucleus attraction, and the electron-electron and nucleus-nucleus repulsions.

From the expression of the Hamiltonian operator for a many-body system, it is easy to see that it is difficult to solve the *S*chrödinger equation analytically for systems containing more than two electrons. This is where Born-Oppenheimer (BO) approximation comes into play. The large difference in the masses of nuclei and electrons results in very different timescales of nuclear and electronic motions, which enables the separation of nuclear and electronic degrees of freedom. If we neglect the motions of nuclei and solve the electronic at some fixed coordinates, we get

$$\widehat{H}_{el}\Psi_{el}(\boldsymbol{r};\boldsymbol{R}) = E_{el}\Psi_{el}(\boldsymbol{r};\boldsymbol{R}) \qquad (9)$$

where $\widehat{H}_{el}$ is the electronic Hamiltonian, E_{el} is the electronic energy and $\Psi_{el}(\boldsymbol{r};\boldsymbol{R})$ is the electronic wave function which depends parametrically on the position of nuclei, $\boldsymbol{R}$.

The first numerical method to solve this equation used the Hartree-Fock approximation. Followed by that, there are more advanced wave function based approaches to solve the many-body problem, such as perturbation theory (MP2, MP4, ...),[70] configuration interaction (CI),[71] coupled cluster methods (CC)[71] and multi-configuration self-consistent field methods (MCSCF and CASSCF).[72] Alternatively, density functional theory provides a popular and successful approach to solve the problem.

2.2.2 The Thomas-Fermi Model

Thomas and Fermi used the electron density to calculate the total energy of a system for the first time in the 1920's.[73] Different from the wave function, electron density is an observable, and it contains all the information needed to describe the system. Cusps in the electron density mean the position of the nuclei, the value of ρ at nuclei gives information about the nuclear charge, and the integration of electron density gives the number of electrons, N.

$$\int \rho(\boldsymbol{r})\, d\boldsymbol{r} = N \tag{10}$$

The idea of expressing the energy of a system as functional of the electron density greatly reduces the dimensionally from 3N to 3 coordinates. According to Thomas-Fermi model, the energy consists of non-interacting kinetic energy and the classical terms for electron-electron and electron-nucleus interactions. By minimizing the energy with respect to density, the ground state energy of the system can be determined. One problem with the Thomas-Fermi approach is that the exchange and correlation energy are completely ignored, and the kinetic energy is calculated from non-interacting electrons where a homogeneous electron gas is considered. Despite of the defects, this model is historically important since it was the first attempt to establish an energy expression using only the electron density as the basic variable.

2.2.3 The Hohenberg-Kohn Theorems

Density Functional Theory was proposed on the basis of two theorems of Hohenberg and Kohn,[74] who demonstrated that the complex wave-function can indeed be replaced by the ground state electron density. The first theorem states that "*the ground state of any interacting many-particle system with a given fixed inter-particle interaction is a unique functional of the electron density* ρ." As a result, the ground state energy E_0 can be written as a functional of ground state density ρ_0,

$$E_0 = E[\rho_0] = T_e[\rho_0] + E_{ee}[\rho_0] + E_{ne}[\rho_0] = E_{ne}[\rho_0] + F_{HK}[\rho_0] \quad (11)$$

where $F_{HK}[\rho]$ is called the Hohenberg-Kohn functional. $F_{HK}[\rho]$ is a universal functional, which means that it is independent of the systems, but unfortunately the exact form of $F_{HK}[\rho]$ is unknown. Nevertheless, $E_{ee}[\rho]$ can be considered as the sum of two parts. One is the Hartree energy $E_H[\rho]$, where

$$E_H[\rho] = \frac{1}{2}\int \frac{\rho(\boldsymbol{r})\rho(\boldsymbol{r}')}{|\boldsymbol{r}-\boldsymbol{r}'|} d\boldsymbol{r}d\boldsymbol{r}' \quad (12)$$

and the other is $E_{ncl}[\rho]$, which is the non-classical term. To summarize, there is a one-to-one correspondence between the external potential and the ground state density of the system.

The second theorem states that, "*For any positive definite trial density* ρ_t, *such that* $\int \rho_t(\boldsymbol{r})d\boldsymbol{r} = N$ *then* $E[\rho_t] \geq E_0$" This enables the use of the variational principle to calculate the ground state energy if the energy functional is known. Any trial density that is different from ground state density yields an energy higher than the true ground state energy. It should be pointed out though that because $F_{HK}[\rho]$ is unknown and some approximations have to be made.

2.2.4 The Kohn-Sham Equations

Although Hohenberg-Kohn theorems set the foundation of density functional theory, it is still not a practical tool for calculating the ground state density and energy since an efficient scheme is missing. This was developed when Kohn and Sham (KS) introduced the concept of a non-interacting reference system.[75] With this approach, the unknown kinetic energy density functional $T_e[\rho]$ are separated into two parts, one is T_s which is the kinetic energy of a non-interacting system, and an unknown component T_c which contains the correlations resulting from the interaction of electrons. The non-interacting system kinetic energy T_s can be expressed as,

$$T_s = -\frac{1}{2}\sum_i \phi_i^* \nabla^2 \phi_i(r) d\boldsymbol{r} \tag{13}$$

where ϕ_i are single-particle Kohn-Sham orbitals, and they produce the same electron density as the interacting many-body system. KS orbitals are determined in a self-consistent way from the KS equations,

$$f_{KS}\phi_i(\boldsymbol{r}) = \varepsilon_i \phi_i(\boldsymbol{r}) \tag{14}$$

The Kohn-Sham operator f_{KS} is an effective one-electron operator, given by,

$$f_{KS} = -\frac{1}{2}\nabla^2 + V_{est}[\rho] + V_H[\rho] + V_{XC}[\rho] \tag{15}$$

where $V_{est}[\rho]$ is the external potential caused by the nuclei. In summary, the universal Hohenberg-Kohn functional is expressed as,

$$F_{HK} = T + E_H + E_{XC} \tag{16}$$

where E_{XC} is the correlation-exchange functional, which contains all the many-body effects and is unknown.

2.2.5 Exchange-Correlation Functionals

2.2.5.1 Local Density Approximation

Within the KS framework, the only term that is not clear is the exchange-correlation functional, which is critical for the obtaining reliable DFT results. Although approximations have been proposed in order to describe the exchange-correlation energies, there are no systematic ways on how to achieve more accurate results, as in wave function-based methods.

Homogenous electron gas was first used to find an explicit expression for $E_{XC}[\rho]$. Because electrons are charged particles, in order to maintain the charge neutrality of the system, positive charge is included through the Jellium model. Through this model, the positive charge is smeared out uniformly through the system, forming a positive background, which maintains the charge

neutrality but does not exert any field on the electrons. The basic assumption is that the exchange and correlation only depend on the local value of electron density, it is therefore called the local-density approximation (LDA). The exchange-correlation functional is given by,

$$E_{XC}^{LDA}[\rho(\boldsymbol{r})] = \int \rho(\boldsymbol{r})\, \varepsilon_{XC}(\rho(\boldsymbol{r}))d\boldsymbol{r} \tag{17}$$

where $\varepsilon_{XC}(\rho(\boldsymbol{r})$ is the exchange-correlation energy per particle of the homogenous electron gas. The analytical form of exchange part can be obtained from the homogenous electron gas,

$$E_{XC}^{LDA}[\rho(\boldsymbol{r})] = \int \rho(\boldsymbol{r})(-\frac{3}{4})\sqrt[3]{\frac{3\rho(\boldsymbol{r})}{\pi}}\, d\boldsymbol{r} \tag{18}$$

On the other hand, the analytical form of correlation energy is unknown and can only be parametrized using results from quantum Monte Carlo calculations.

2.2.5.2 Generalized Gradient Approximation

Although local-density approximation performs well for many systems compared with Hartree-Fock, it usually overestimates the binding energies and underestimates the bond lengths. It also becomes a poor assumption for systems with less homogenous electron densities. Improvements were made based on LDA by including the first gradients of the electron density, which yields the generalized gradient approximation (GGA). Under GGA, the exchange-correlation functional is given by,

$$E_{XC}^{GGA}[\rho(\boldsymbol{r})] = \int f(\rho(\boldsymbol{r}), \nabla\rho(\boldsymbol{r}))d\boldsymbol{r} \tag{19}$$

Including the density gradients gives much reliable binding energy than LDA, which makes GGA the most popular class of functionals in DFT calculations. Nowadays the development of more accurate exchange correlation functionals is still an important field of research.

2.2.6 Plane-wave DFT

According to Bloch's theorem,[76] plane-wave basis set are a convenient way to represent the wave function of systems with periodic boundary conditions.,

$$\psi_j(\boldsymbol{r}, \boldsymbol{k}) = N \sum_{\boldsymbol{G}} c_{j\boldsymbol{G}\boldsymbol{k}}\, e^{i(\boldsymbol{k}+\boldsymbol{G})\boldsymbol{r}} \tag{20}$$

where j runs over the KS orbitals, $\boldsymbol{k}$ is a vector in the first Brillouin zone, $\boldsymbol{G}$ is a reciprocal lattice vector defined through $\boldsymbol{G} \cdot \boldsymbol{R} = 2\pi m$, where $\boldsymbol{R}$ is the real space lattice vector and m is an integer, $c_{j\boldsymbol{G}\boldsymbol{k}}$ are the plane-wave expansion coefficients, and N is a normalization factor. In order to have a tractable number of plane waves, the Brillouin zone is discretized with a *k*-point grid and equation (19) is truncated with a kinetic energy cut-off for the plane waves,

$$\frac{1}{2}|\boldsymbol{k} + \boldsymbol{G}|^2 \leq E_{cut} \tag{21}$$

Each of the coefficients for the plane waves has a kinetic energy, and the ones with higher kinetic energies usually conation less important information than those with lower kinetic energies. As a consequence, an energy cutoff of the plane-wave was introduced to reduce the basis set to a finite size. It can be imagined that the kinetic energy cutoff will lead to some error in the calculations, it is thus important to test the convergence of the cutoff energy and choose an appropriate value for the system studied.

2.2.7 Pseudopotentials

Although plane wave basis used to expand the electron wavefunctions in the KS equations can be truncated, the inclusion of all electrons and the full Coulombic podetial with nuclei make the computation very expensive, especially for large systems with transition metals. Considering the chemistry most relates to the valance electrons while core electrons are much more tightly bound to nuclei and are almost independent of the environment, pseudopotential approximation

was proposed. In this approximation, a pseudopotential is used to replace the core electrons and ionic potential, which significantly reduces the computational cost.

A main drawback of pseudopotential method is that all information on the full wave function close to the nuclei are lost. This can influence the calculation of certain properties. The projector-augmented wave (PAW)[77] method was proposed to provide more accurate results, in which the rapidly oscillating wavefunctions near cores transformed into smooth wavefunctions, and all-electron properties can be calculated from these smooth functions.

2.2.8 Optimization Algorithm

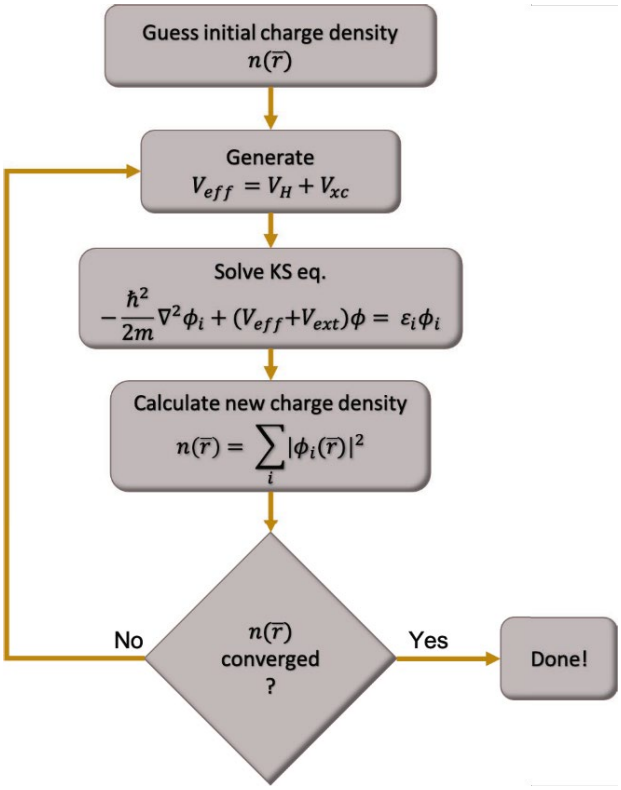

Figure 1. Flowchart of the self-consistent KS-DFT method, reproduced from Ref. [78].

The ground state density energy is determined in a self-consistent manner. As shown in Figure 1, it starts with an initial guess for the electron density, which can be used to solve the KS equations. This generates a set of new KS orbitals which corresponds to a new electron density.

By repeating this process, the new electron density gets closer to the exact ground state electron density. When the difference between the old and new electron density is less than the numerical convergence limit, the calculation can be considered converged, and the ground state energy can be obtained. The local minimum is usually located based on the conjugate gradient scheme.[79-80]

2.3 Nudged Elastic Band Theory

An important and common problem in theoretical chemistry is to find the transition state of a chemical reaction. Among the methods available, the most popular technique is known as the "nudged elastic band" (NEB) method.[81] The reaction pathway is constructed by a set of images between the initial and final states. Each image is optimized by finding its lowest energy possible while maintaining equal distance to neighboring images. The force on each image depends on its neighboring images: at each step the forces parallel to the reaction path are eliminated and a so-called spring force is added that tries to keep each image in the middle between its neighbors.

In the improved Climbing Image Nudged Elastic Band Theory (CINEB) method,[82-83] the highest energy image is driven up to the saddle point. This image does not feel the spring forces along the band. Instead, the true force at this image along the tangent is inverted. In this way, the image tries to maximize its energy along the band, and to minimize in all other directions. This ensures that the image will be at the exact saddle point when it converges.

2.4 Neural Network Potential Energy Surface

Nowadays neural networks (NN) have become a promising method to construct PESs for a wide range of systems. NNs are means of doing machine learning, in which computer learns to perform some tasks by analyzing training examples. Below I will give a brief introduction on the general structure of NNs and the embedded atom neural network method used in the work mentioned in the thesis.

2.4.1 Neural Networks

Inspired by the structure of human brain, the basic unit in an NN is a neuron (or node), through which inputs and outputs are connected together. Figure 2 shows a simple feed-forward NN defining a relationship between the inputs, which are coordinates G_1 to G_4 describing the atomic configuration, and the output, which is the potential energy E. Layers in between input and output layers are called hidden layers, where all the computations are done. Each node in one layer is connected to all the nodes in adjacent layers by weights and biases, which are the fitting parameters. Like in human brains, where neurons are activated when enough stimuli are encountered, an activation function is applied to the nodes to determine whether the node is fired, or in other words, whether the information the node carries is important enough for the fitting. If the weighted sum with some bias adding to it is below a threshold value, the node passes no data to the next layer. If the results exceed the threshold value, the node is activated and will pass the data to the next layer. The activation functions are usually nonlinear, aiming to introduce some non-linearity to the fitting to make it capable to learn and perform complex tasks.

The initial weights and biases are randomly given so they are not likely to produce very good results. The process where the weights and biases are optimized with respect to the difference between the value predicted by NN and true value is called training. To access the fitting error, there are different types of loss functions, and they have their advantages and disadvantages. One of the most commonly used loss function is the root mean squared error (RMSE),

$$\mathrm{RMSE} = \sqrt{\frac{1}{N}\sum_{i=1}^{N}\left(E_{i,ref} - E_{i,NN}\right)^2} \tag{22}$$

where in this case $E_{i,ref}$ is the energy calculated from ab initio methods and $E_{i,NN}$ is the energy fitted from the NN.

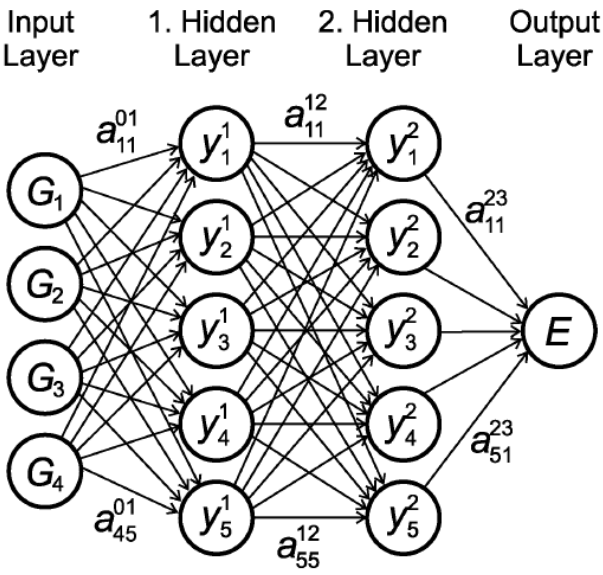

Figure 2. Scheme of a feed-forward neural netwok, reproduced from Ref. [84].

There are many algorithms to minimize the error, one that is frequently used is backpropagation. By defemination, backpropagation means that the error is propagated backwards through the network so the weights and biases can be updated.[85] The backpropagation is performed iteratively until the fitting error is within the tolerance and the fitting stops.

One problem occurring commonly in NN training is overfitting, that is, the NN fits the training dataset very well, but does a bad job predicting the energy of a structure that is not present in the training set. In order to avoid that, it is necessary to have a validation dataset that is not used in training the parameters. What people usually do is to divide the training data into two parts, i.e., training set and validation set. The latter provides an unbiased evaluation of the NN fit on the training data, which can then be used to terminate the training thus avoid overfitting.

2.4.2 Embedded Atom Neural Network

PESs in this thesis were fitted using embedded atom neural network (EANN),[86] which is explained in Figure 3. Developed from the well-known embedded atom method[87-88], EANN assumes the energy of an impurity in a host is a functional of the electron density of the host

without impurity. The total energy of a system containing N atoms is the sum over the energy of each atom, written as,

$$E = \sum_{i=1}^{N} E_i = \sum_{i=1}^{N} NN_i(\boldsymbol{\rho}^i) \tag{23}$$

For simplicity, the electron density of embedded atoms $\boldsymbol{\rho}^i$ can be described by the square of the linear combination of Gaussian-type atomic orbitals (GTOs) centered at adjacent atoms,[89]

$$\rho^i_{L,\alpha,r_s} = \sum_{l_x,l_y,l_z}^{l_x+l_y+l_z=L} \frac{L!}{l_x!\, l_y!\, l_z!} \Big(\sum_{j=1}^{n_{atom}} c_j \varphi^{\alpha,r_s}_{l_x l_y l_z}(\boldsymbol{r}_{ij})\, f_c(r_{ij}) \Big)^2 \tag{24}$$

where n_{atom} is the number of neighboring atoms within the cutoff radius r_c. f_c is a frequently used cosine type cutoff function to decay the interaction to zero smoothly when approaching r_c,[84]

$$f_c(r_{ij}) = \begin{cases} 0.5 \cdot \left[\cos\left(\pi r_{ij}/r_c\right) + 1\right] & for\ r_{ij} \le r_c \\ 0 & for\ r_{ij} > r_c \end{cases} \tag{25}$$

where r_{ij} is the distance between atom i and j.

The expression for Gaussian orbital GTOs can be written as

$$\varphi^{\alpha,r_s}_{l_x l_y l_z}(\boldsymbol{r}) = x^{l_x} y^{l_y} z^{l_z} \exp\left(-\alpha |r - r_s|^2\right) \tag{26}$$

where $\boldsymbol{r} = (x, y, z)$ is the cartesian coordinate of the embedded atom, r is the norm of the vector $\boldsymbol{r}$, l_x, l_y and l_z represents the components of the angular momentum in x, y and z direction, and $l_x + l_y + l_z = L$ determines the orbital angular momentum. α, r_s are parameters relevant to radial distributions of atomic orbitals. This EANN approach has been proved to be computationally efficient and successfully applied in the study of several representative gas-surface reactions.[90-91]

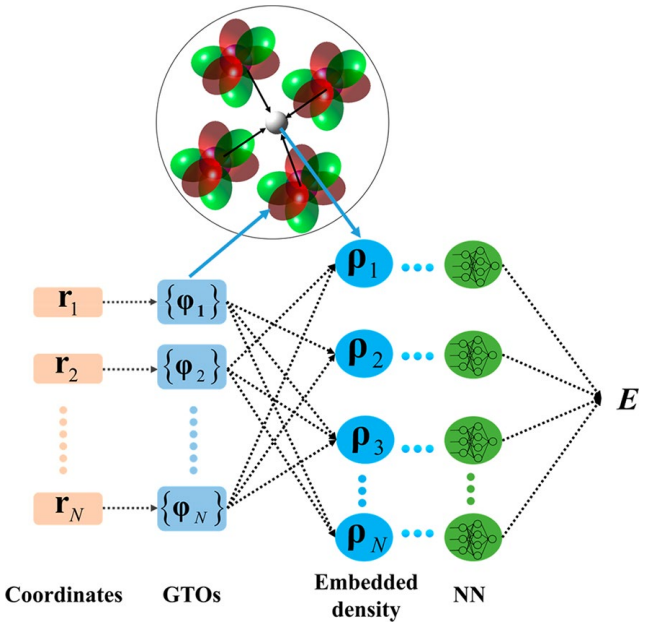

Figure 3. Scheme of the embedded atom neural network, reproduced from Ref. [86].

2.4.3 Protocol for NN Fitting of PESs

The construction of a PES using machine learning tools such as NNs often proceeds in an iterative manner, as depicted in Figure 4. First, we need electronic energies from ab initial calculations (such as DFT) for many different configurations, which cover the space where chemistry happens. The initial dataset can be obtained from AIMD trajectories or manually generated configurations. One common problem with the original dataset is that the points could be rather dense and not evenly distributed, which may influence the performance of NN fitting. To remove points that are too close to each other, the generalized Euclidean distance (GLD) is employed to determine the difference between two geometries:

$$d_{jk} = \sqrt{\sum_{i=1}^{n_{bond}} (r_i^j - r_i^k)^2} \tag{27}$$

In the equation above, n_{bond} represents the number of intermolecular bonds, r_i^j and r_i^k are the jth and kth points, respectively.

After screening the initial dataset, a rough PES can be trained from that. MD trajectories performed on the preliminary PES can be used to find out if there is any 'holes' in the PES and the points there are the current PES does not cover will be added to the initial dataset. A refined PES is built from the new dataset until the completeness is reached.

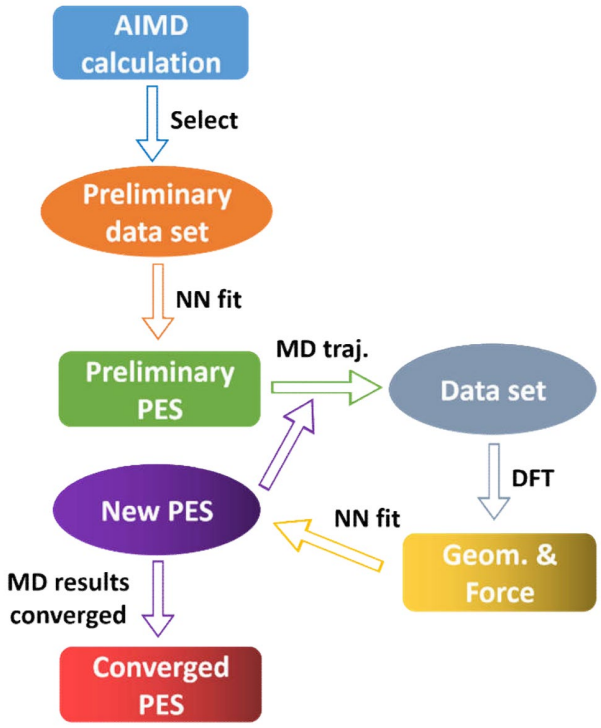

Figure 4. Fitting process of a potential energy surface, reprocured from Ref. [92].

2.5 Molecular Dynamics

2.5.1 Integration Algorithm

In this thesis, the classical dynamics is described by solving Newton's equations of motion. In AIMD calculations using the Vienna Ab initio Simulation Package (VASP),[93-94] the equation of motion is integrated with leapfrog algorithm. In quasi-classical trajectory calculations using analytic NN PESs, it is integrated with velocity Verlet algorithm.

2.5.1.1 Velocity Verlet

In the velocity Verlet algorithm,[95] which is introduced below, first the velocity is updated every half a timestep and then the position is updated every full timestep. Finally, the velocity is updated at another half timestep.

$$\boldsymbol{v}(t + \Delta t/2) = \boldsymbol{v}(t) + \boldsymbol{a}(t)\Delta t/2 \tag{28}$$

$$\boldsymbol{x}(t + \Delta t) = \boldsymbol{x}(t) + \boldsymbol{v}(t + \Delta t/2)\Delta t \tag{29}$$

$$\boldsymbol{v}(t + \Delta t) = \boldsymbol{v}(t + \Delta t/2) + \boldsymbol{a}(t + \Delta t)\Delta t/2 \tag{30}$$

2.5.1.2 Leapfrog

While the leapfrog algorithm is similar to the velocity Verlet algorithm, the velocity and position are updated at staggered time points in the leapfrog algorithm. The advantages of leapfrog over velocity Verlet algorithm are that it requires only one energy evaluation per step, requires only modest memory and allows a relatively large timestep to be used.

$$\boldsymbol{v}(t + \Delta t/2) = \boldsymbol{v}(t - \Delta t/2) + \boldsymbol{a}(t)\Delta t \tag{31}$$

$$\boldsymbol{x}(t + \Delta t) = \boldsymbol{x}(t) + \boldsymbol{v}(t + \Delta t/2)\Delta t \tag{32}$$

2.5.2 Initial Condition Sampling

The initial velocities of surface atoms at a given temperature are generated according to the Maxwell-Boltzmann distribution. When the surface does not start with an equilibrium configuration, the kinetic energy of the surface converts to potential energy as minimized structure changes to the equilibrium structure, which results in a change in temperature. To maintain the desired temperature, the velocities of surface atoms need to be adjusted appropriately. Some temperature-control mechanism, such as velocity rescaling[96] and Berendsen thermostat[97], needs to be employed.

The gas atom or molecule is initially placed far above the surface where the interaction is considered weak and can be neglected. The initial translational energy is given based on the experimental conditions, more specially, incidence energy and angle.

2.5.3 Final State Calculation

The final state of scattered gas atom or molecule contains important information about the dynamics. Commonly used indicators are the angular and energy distribution. The scattering angle θ_f is defined as,

$$\theta_f = \frac{v_z}{\sqrt{v_x^2 + v_y^2 + v_z^2}} \tag{33}$$

where v_x , v_y and v_z are the velocity of the center of mass in x, y and z direction, respectively. The translational energy is simply obtained from the equation below,

$$E_{trans} = \frac{1}{2} m(v_x^2 + v_y^2 + v_z^2) \tag{34}$$

The internal energy is calculated as,

$$E_{int} = E_{elec} + E_{vib} + E_{rot} \tag{35}$$

where E_{elec}, E_{vib} and E_{rot} are electronic, vibrational and rotational energy, respectively.

CHAPTER 3

CO_2, H_2O AND GLYCINE SCATTERING FROM HOPG SURFACE

The materials discussed in this chapter is based on the publications: Murray, V. J.; Zhou, L.; Xu, C.; Wang, Y.; Guo, H.; Minton, T. K. Scattering dynamics of glycine, H_2O, and CO_2 on highly oriented pyrolytic graphite. *J. Phys. Chem. C* **2019**, *123*, 3605-3621; and Zhou, L.-s.; Wang, Y.-q.; Guo, H. Dynamics studies of diglycine scattering from highly oriented pyrolytic graphite. *Chin. J. Chem. Phys.* **2020**, *33*, 196-202.

3.1 Introduction

The characterization of neutral compounds in rarefied atmospheres is a challenging endeavor that is complicated by the extremely low number density (10^{10}–10^3 cm^{-3}) for molecules of interest, which include life-signature organic molecules. Mass spectrometry has been used in the past to study the composition of tenuous atmospheres around planetary bodies;[98-100] however, low concentrations result in poor signal-to-noise ratios, which can make the determination of the atmospheric composition both imprecise and inaccurate. A neutral-gas concentrator designed for the purpose of identifying tenuous atmospheres has been proposed to mitigate the challenges arising from low number densities.[101] This device, referred to as a concentrator, is composed of a funnel-shaped inlet with a large entrance and small exit, which is coupled to a spherical accommodation chamber that has a large exit leading to a mass spectrometer. The geometry of the concentrator is such that it approximates a unidirectional valve. Incoming molecules that scatter down the length of the concentrator will accumulate in the accommodation chamber, which increases the density of the gas that is sampled by the mass spectrometer.

The details of the gas−surface interactions between the incoming molecules and the concentrator surfaces will ultimately determine the flux of molecules that enter the accommodation chamber. It was determined that impulsive collisions that result in specular, or even super specular, angular distributions will lead to the largest number of molecules arriving in the accommodation chamber and yield a higher concentration factor.[101] Surfaces that promote broad angular distributions or trapping desorption reduce the concentration factor of the device. A test particle model that utilized the experimental results of molecular beam-surface scattering experiments, referred to as the Statistical Program for Aerodynamics and Radiation Pressure Coefficient Simulation,[102] pyrolytic graphite (HOPG) will perform well because O, O_2, and Ar undergo nearly elastic collisions and scatter from the surface with well-defined angular distributions that are directed beyond the specular angle.[101] Subsequent experimental work has shown that methyl formate and nitromethane survive collisions with HOPG without dissociating during the gas−surface interaction despite having a relatively high average incidence energy, $\langle E_i \rangle$, near 100 kJ mol^{-1}.[103] However, the details of the scattering dynamics of life-signature organic molecules, for example, the amino acid glycine (GLY), must be better understood before the concentrator can be considered as a viable mass spectrometer inlet for the analysis of tenuous atmospheres.

The scattering dynamics of polyatomic molecules are more complicated than those for atoms and diatomic molecules, because the incidence energy can be transferred into vibrational and rotational modes as well as into the surface.[104] Studies of the impulsive scattering of NH_3 from Au(111) demonstrated that the amount of vibrational excitation increased with the normal incidence energy of the molecule ($E_{n,i} = E_i \cos^2\theta_i$).[105] In addition, large organic molecules can break apart if too much energy is transferred to internal modes during the collision, a process referred to as shattering.[106] Even if the molecule does not dissociate during its interaction with the

surface, its electron impact (EI) ionization fragmentation pattern can change with increasing internal excitation,[107-110] which could lead to the misidentification of molecules when using a mass spectrometer that employs an EI ionizer to analyze tenuous atmospheres. Energy transfer to the internal modes of the molecule can be reduced by maintaining a large (grazing) incidence angle, θ_i, between the molecule and the surface so that $E_{n,i}$ is minimized.[111-112]

Although a grazing θ_i reduces the internal excitation of the molecule, it increases the probability for the molecule to undergo multiple collisions with the surface.[38-39, 113] Each subsequent collision might be expected to increase the translational energy transfer and result in an increased trapping probability. However, the incident parallel momentum of N_2 and O_2 colliding with HOPG was conserved even though the molecules suffered multiple collisions before scattering.[39, 113] Parallel momentum conservation after multiple atom-surface interactions was also observed for Ar scattering from a hot Pt(111) surface by Head-Gordon et al.[114] and more recently for methyl formate and nitromethane scattering from HOPG by some of the current authors.[103] The results of the latter experiments suggest that a portion of these polyatomic molecules transfer a significant amount of energy during the molecule−surface interaction. However, the nitromethane and methyl formate scatter before coming fully into thermal equilibrium with the surface, presumably because the residence times of these molecules are too short for their parallel momentum to fully dissipate. This scattering mechanism, referred to as quasi-trapping, produced lobular angular distributions directed beyond the specular angle despite a significant amount of translational energy transfer. There was some evidence that the molecules became vibrationally excited during this process,[103, 110] which could lead to molecular dissociation or change the EI fragmentation pattern in the mass spectrum of a particular molecular species.

The work presented in this article explores the scattering dynamics of H_2O, CO_2, and GLY on an HOPG surface. The objective was to understand the scattering dynamics of a life signature organic molecule (with GLY being a simple, experimentally tractable example) from HOPG, the surface previously chosen for a concentrator intended for the study of tenuous atmospheres. H_2O and CO_2 were byproducts of the method used to produce GLY, and these smaller molecules may also be present in planetary atmospheres, so their scattering dynamics were studied, too. Detailed MD simulations utilizing an empirical reactive force field, ReaxFF, were carried out, and they provide an in-depth, molecular level understanding of the scattering dynamics observed in the experiment. H_2O and CO_2 were found to scatter from the surface predominantly through an impulsive scattering mechanism where the molecules experienced a single collision with the surface; the simulations revealed that only a small fraction suffered multiple collisions with the surface. Moreover, successive collisions did not significantly affect the scattering dynamics of these triatomic molecules. While GLY molecules scattered from the surface with narrow angular distributions, these molecules exchanged a significant amount of energy during collisions with the surface. The simulations showed that the majority of the GLY molecules interacted with the surface for several picoseconds before scattering into the vacuum. The long residence time enhanced the transfer of translational energy and promoted vibrational excitation of GLY. The diverse scattering dynamics apparent for H_2O, CO_2, and GLY can be attributed to the different interaction potentials between each molecule and the HOPG surface, as well as the different numbers of internal degrees of freedom in the molecules. A stronger molecule−surface interaction results in a longer average residence time on the surface which facilitates energy transfer to and from the molecule.

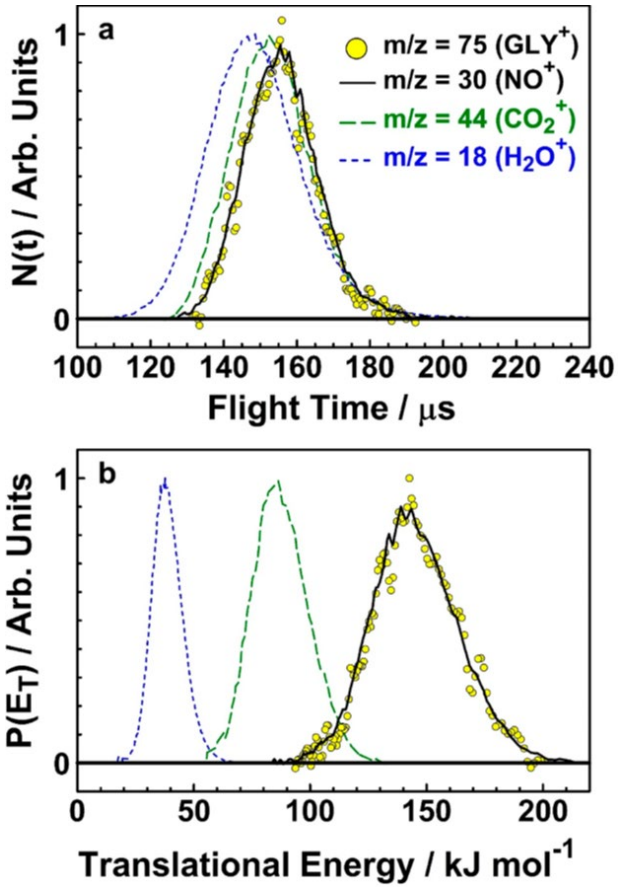

Figure 1. (a) Time-of-flight (TOF) distributions and (b) translational energy distributions, P(E_T), for m/z = 18 (H_2O^+), 44 (CO_2^+), 30(NO^+), and 75 (GLY^+). The $P(E_T)$ distributions for m/z = 30 (NO^+), the dominant fragment of GLY produced in the electron impact ionizer, were obtained by assuming the mass of the parent was 75 amu prior to dissociative ionization. The distributions have been normalized to a value of 1.0 for ease of comparison.

3.2 Experimental methods

The experiments were conducted with the use of a crossed molecular beams machine reconfigured for beam-surface scattering. A description of this apparatus has been presented in detail in earlier publications,[38, 103] and only the relevant information will be presented here. A continuous molecular beam of H_2O, CO_2, and GLY seeded in He was directed at a sample of ZYA quality HOPG (Momentive Inc., mosaic spread of 0.4 ± 0.1°). The sample was mounted on a manipulator that could be rotated to change the incidence angle, θ_i, between the sample and the incident molecular beam. When θ_i = 0°, the molecular beam is aligned with the surface normal.

The temperature of the sample surface (T_s) was held at 677 K. Previous results from our group have demonstrated that HOPG is free of contamination at this temperature despite the relatively high operating pressure (2×10^{-6} Torr) in the main scattering chamber.[103] The extremely narrow angular distributions observed for GLY, presented in section 4, confirm that the surface is clean.

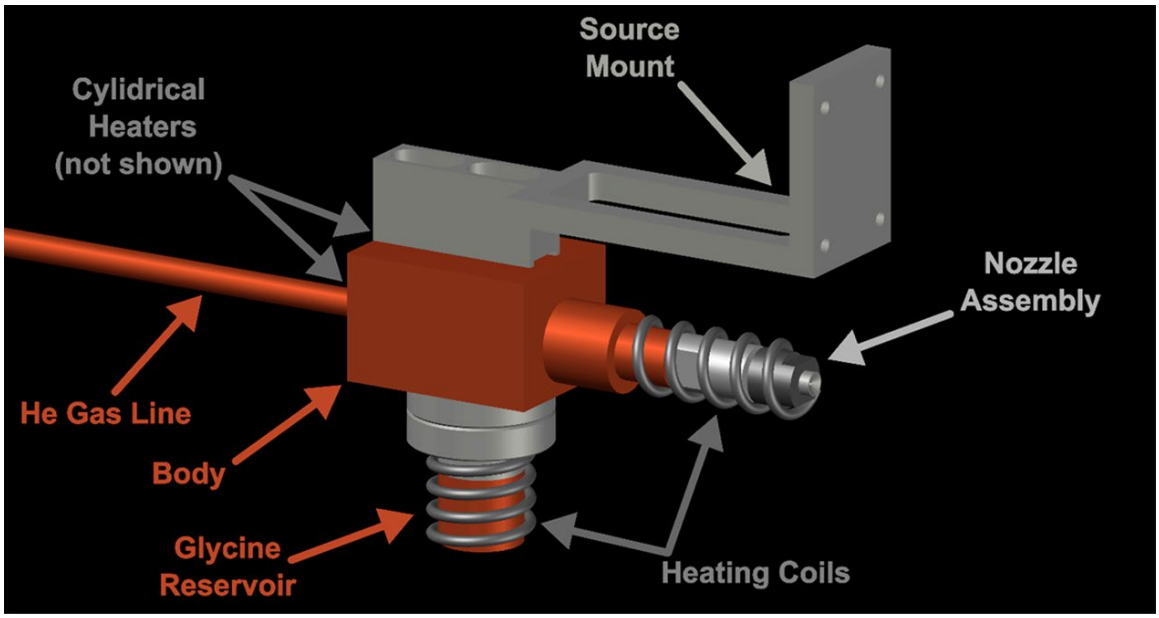

Figure 2. Schematic diagram of the supersonic glycine (GLY) source

The continuous molecular beam and the products that scattered from the HOPG surface were monitored by a rotatable, mass spectrometer detector that used an EI ionizer,[115] a quadrupole mass filter, and a Daly type ion counter operated in pulsed counting mode.[116] A mechanical chopper wheel, with three equally spaced slots of 1.5 mm width and rotating at a frequency of 150 Hz, was mounted just in front of the entrance to the detector. This chopper wheel was used to modulate molecules that traveled toward the detector. A multichannel scaler was used to record the number density distributions, N(t), of molecules as a function of their arrival time, t, at the ionizer, 30.4 mm downstream from the chopper wheel. These distributions, referred to as time-of-flight (TOF) distributions, were collected for the molecules that scattered from the surface, and such distributions were also collected for molecules in the incident beam by lowering the sample

out of the beam path and directing the beam straight into the detector (Figure 1a). The TOF distributions were used to derive translational energy distributions, $P(E_T)$, using the relationship $P(E_T) \propto t^2 N(t)$ where $E_T = \frac{1}{2}m(\frac{d}{t})^2$, d is the distance from the chopper wheel to the ionizer (30.4 mm), and m is the mass of the molecule. The $P(E_T)$ distributions for the molecules in the incident beam are shown in Figure 1b. The average translational energy, denoted as $\langle E_T \rangle$ for the molecules scattering from the surface, was determined from the $P(E_T)$ distributions. The GLY had an average incidence energy, $\langle E_i \rangle$, of 149.5 kJ mol^{-1}. For H_2O and CO_2 in the molecular beam, $\langle E_i \rangle$ = 38.9 and 87.5 kJ mol^{-1}, respectively.

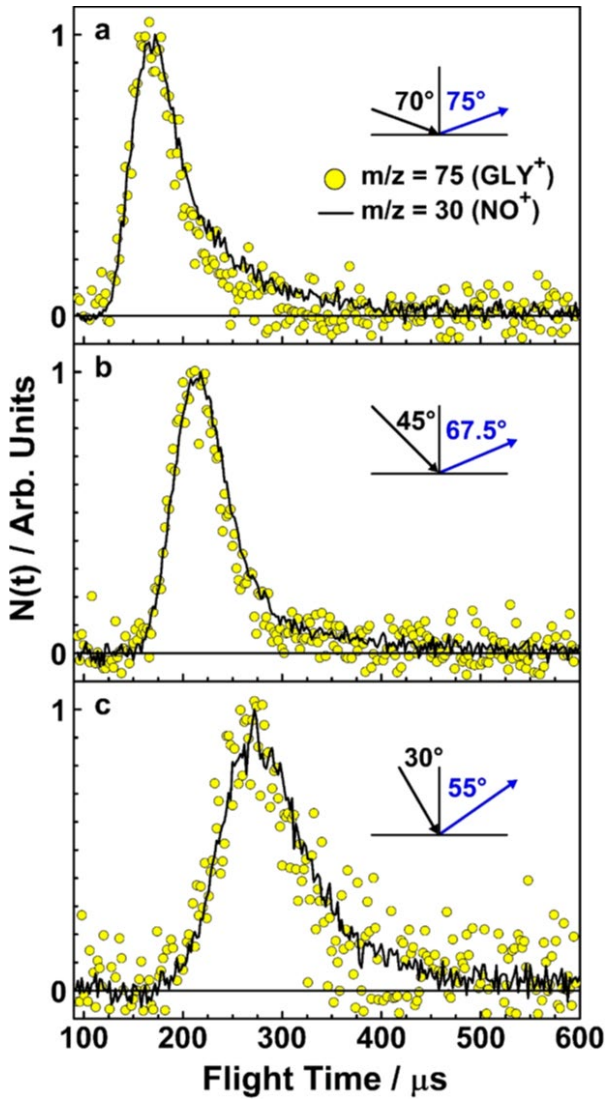

Figure 3. Representative TOF distributions collected at m/z = 75 (GLY^+) and 30 (NO^+), following bombardment of the HOPG surface by the molecular beam with $\langle E_i \rangle$ = 149.5 kJ mol^{-1}. Incidence (θ_i) and final (θ_f) angles corresponding to each TOF distribution are shown. The distributions have been normalized to a value of 1.0 to facilitate comparison.

The supersonic beam was prepared with the use of a custom built GLY sublimation molecular beam source (Figure 2) that consisted of a copper reservoir and body attached to a stainless steel nozzle. Both the reservoir and nozzle were heated with coaxial heaters, while the body of the source was heated with two cylindrical heaters. The temperatures of the three components of the source assembly were measured separately with three type K thermocouples. HPLC grade GLY powder (Sigma-Aldrich) was loaded into the reservoir and heated to a temperature of 423 K. At this temperature, thermal decomposition of GLY in the gas phase, which occurs around 523 K, is expected to be negligible.[117-119] While a direct measurement was not possible, it was estimated that GLY had a vapor pressure of less than 1 Torr at the reservoir temperature employed in this study. 250 Torr of helium (99.9999%) was swept over the top of the reservoir, and the mixture was expanded through a 150 μm pinhole in a small platinum plate at the end of the nozzle assembly. The body and the nozzle were held at temperatures of 428 and 431 K, respectively, to prevent GLY condensation. The beam was collimated by a 0.56 mm diameter skimmer and a 1.3 high × 0.44 mm wide slit that were, respectively, 5.8 and 44.7 mm downstream from the nozzle. The absence of dimers in the molecular beam was confirmed by the lack of signal at a mass-to-charge ratio (m/z) of 105 ($GLY\text{-}NO^+$) when the molecular beam was interrogated directly by collecting TOF distributions of species in the beam. The molecular beam contained molecules detected at . While GLY produces daughter ions at m/z = 18 (H_2O^+) and 44 (CO_2^+), the beam TOF distributions collected at these m/z ratios were shifted to shorter flight times than the distributions for GLY, indicating that H_2O and CO_2 were not formed from dissociative ionization

of the GLY molecule in the EI ionizer (Figure 1a). It is possible that the majority of the H_2O present in the molecular beam originates from H_2O that is adsorbed on the hydrophilic GLY powder. Attempts to dry the GLY powder were made by gently heating the reservoir at a temperature of 323 K overnight while pumping through the nozzle of the beam source (base chamber pressure 10^{-7} Torr). However, H_2O was still present in significant quantities in the molecular beam despite these efforts. Though the source temperature was kept sufficiently low enough that GLY in the gas phase was not expected to undergo thermal decomposition,[117-119] it has been shown that GLY readily dissociates to CO_2 and H_2O in the presence of platinum at the nozzle temperatures employed in this study.[120] Therefore, the CO_2 and some of the H_2O present in the molecular beam are assumed to originate from a GLY decomposition reaction mediated by the metal surfaces of the source. The composition of the molecular beam (excluding He) was approximately 90.7% H_2O, 4.9% CO_2, and 4.4% GLY. Given that the mass-spectral intensities of the EI fragments of GLY at m/z = 75 (GLY+), 44 (CO_2^+), and 18 (H_2O^+) are expected to be similar and the observed intensity of the signal detected m/z = 75 was much smaller than the signals at m/z = 44 and 18, the TOF distributions for m/z = 44 and 18 were assumed to come from CO_2 and H_2O in the beam and were therefore not corrected for the dissociative ionization of GLY.

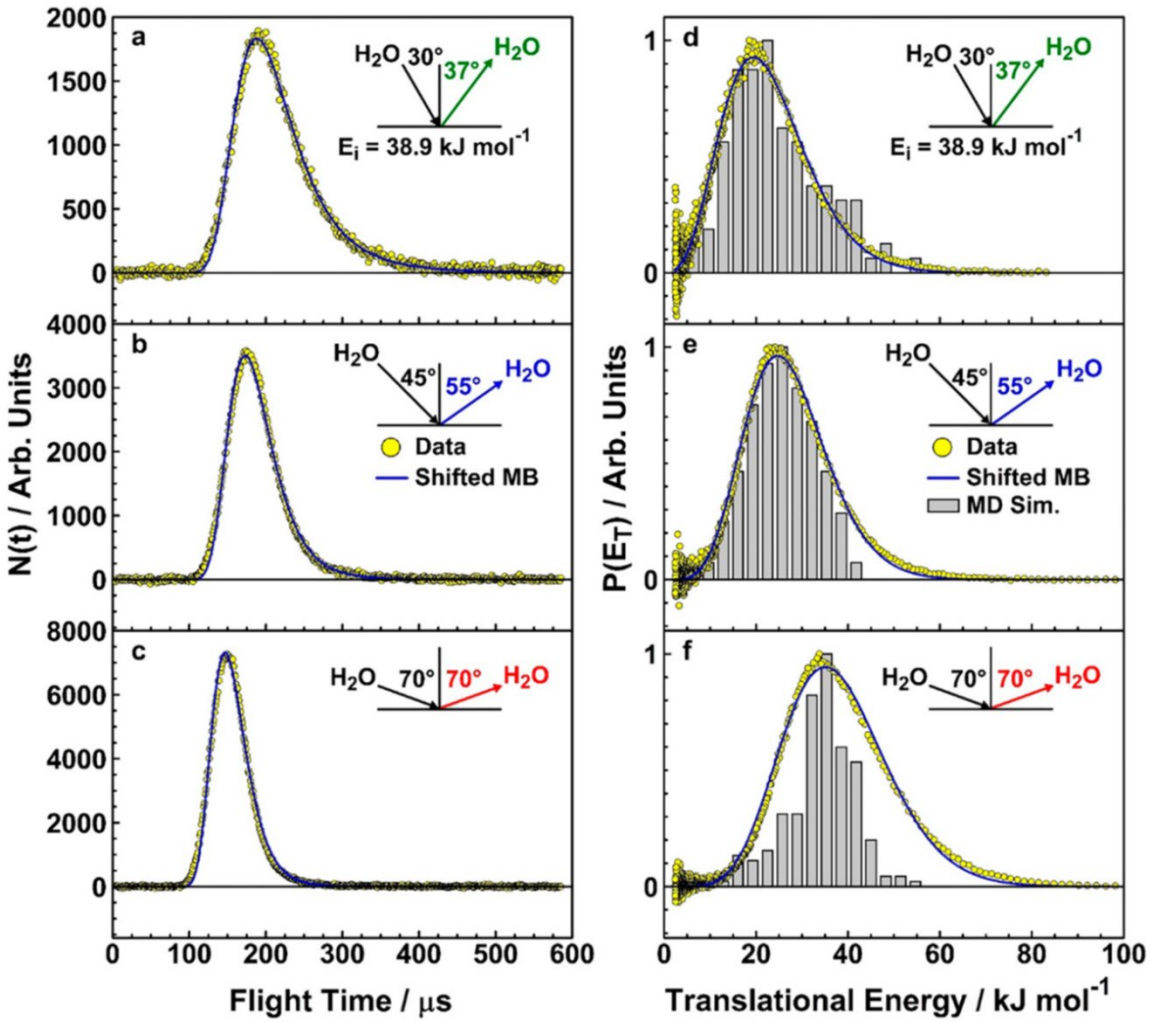

Figure 4. Representative TOF (a−c) and $P(E_T)$ (d−f) distributions for scattered H_2O, with $\langle E_i \rangle$ = 38.9 kJ mol^{-1}. Incidence (θ_i) and final (θ_f) angles corresponding to each distribution are shown. The yellow symbols represent the experimental data, and the blue lines represent the shifted, flux weighted MB distribution used to fit the IS component. The gray bars in the right column represent the simulated $P(E_T)$ distributions obtained from the MD simulations, where the trajectories were averaged over an angular range of ±3° in θ_f and ±3° from the scattering plane.

The dominant ion formed when GLY is ionized is m/z = 30 (NO^+). The flux ratio of the GLY parent ion, m/z = 75 (GLY^+), to the daughter ion, m/z = 30 (NO^+), was 0.04. While NO has not been observed as a reaction product for either thermal decomposition or surface reactions of GLY,[120] measurements were performed to confirm that m/z = 30 (NO^+) was formed in the EI ionizer and not from a shattering mechanism or gas− surface reaction occurring when the GLY

molecule collided with the HOPG. TOF distributions for selected combinations of incidence and final angles (θ_i and θ_f, respectively, where θ_f is located on the opposite side of the surface normal from θ_i) were collected for m/z = 75 and 30. The TOF distributions for m/z = 30 and m/z = 75 were identical for these selected sets of angles (Figure 3), suggesting that NO^+ is indeed a daughter ion of GLY. The experimental scattering dynamics for NO^+ suggest that the GLY molecules do not shatter on the surface, similar to our previous results for nitromethane and methyl formate scattering from HOPG.[103] This result is not unexpected, considering that the dissociation energy for the various bonds in GLY are between 307.9 and 330.5 kJ mol^{-1}.[121] Even if all the incidence energy were partitioned into internal modes of the molecule, there would not be enough energy to dissociate the molecule. Furthermore, the HOPG surface is relatively inert and is not expected to catalyze the dissociation of GLY. Hence, the scattering dynamics observed for m/z = 30 (NO^+) are an accurate representation for the scattering dynamics of GLY. The TOF distributions collected for m/z = 30 were corrected for the ion flight time and were analyzed assuming that the detected molecule had a mass of 75 amu. For the remainder of the paper, when we discuss results pertaining to GLY, we are referring to the scattering dynamics derived from TOF distributions collected at m/z = 30. The scattering dynamics for H_2O, CO_2, and GLY were interrogated by collecting TOF distributions over a range of accessible θ_f angles corresponding to θ_i = 70, 45, and 30°. For θ_i = 70 and 45°, θ_f was varied from 5−80°. When θ_i=30°, the range of θ_f was constrained to 20−80° by the geometry of the machine. For GLY, angular distributions were collected for only θ_i = 70 and 45° because of the low signals and the rise in He pressure in the detector that occurred during long data acquisition times. Long-term drift during the experiment was accounted for by incrementing θ_f from low to high and then high to low, until two TOF distributions were collected for m/z = 18 (H_2O^+) and 44 (CO_2^+) and six TOF distributions were collected for m/z = 30 (NO^+) for each θ_f.

Prior to analysis, the individual TOF distributions were summed together and corrected for electronic offsets associated with the chopper wheel and the ion flight time of the molecules through the quadrupole mass filter. Angular distributions were obtained by appropriate integration of the TOF distributions collected at each θ_f and plotting the flux of the scattered molecules as a function of θ_f. The average post collision translational energy, $\langle E_T \rangle$, of the scattered molecules was also derived from the TOF distributions as a function of θ_f.

3.3 Calculational methods

We used the ReaxFF force field in the MD simulations for both the molecule and the graphene substrate,[69, 122] which describes bonded and nonbonded interactions determined by bond orders calculated from interatomic distances that are updated at every MD step. The ReaxFF parameters used in the present simulations for H_2O and CO_2 were obtained from Chenoweth et al.[123] for hydrocarbon combustion and hyperthermal collisions of atomic oxygen with graphene.[124] The ReaxFF parameters for GLY are from Rahaman et al.[125] The HOPG surface was modeled by the (0001) surface of graphite, which was simulated with a periodic slab consisting of 6 graphene layers with a (8×8) surface cell that contains 128 carbon atoms per layer. The surface model employed in this study was used recently to study the scattering of N_2 from HOPG.[38] The experimental surface temperature (T_s = 677 K) was simulated with the initial conditions that the velocities of surface atoms, except for the bottom layer, is assigned with a Maxwell−Boltzmann distribution at 677 K, followed by 20 ps equilibration with an isobaric−isothermal (NPT) ensemble, in which the periodic cell was held at a constant pressure of 1 atm using the Berendsen barostat with a damping constant of 50 fs and a Berendsen thermostat with a coupling of 10 fs.[97] This equilibration step was followed by an extra 30 ps microcanonical (constant number, volume, and energy, NVE) MD simulation. During the last 10 ps of the NVE simulations, 1000 snapshots of

the slab were taken at every time step (10 fs), which provided the initial configurations of the thermalized slab in the subsequent MD simulations.

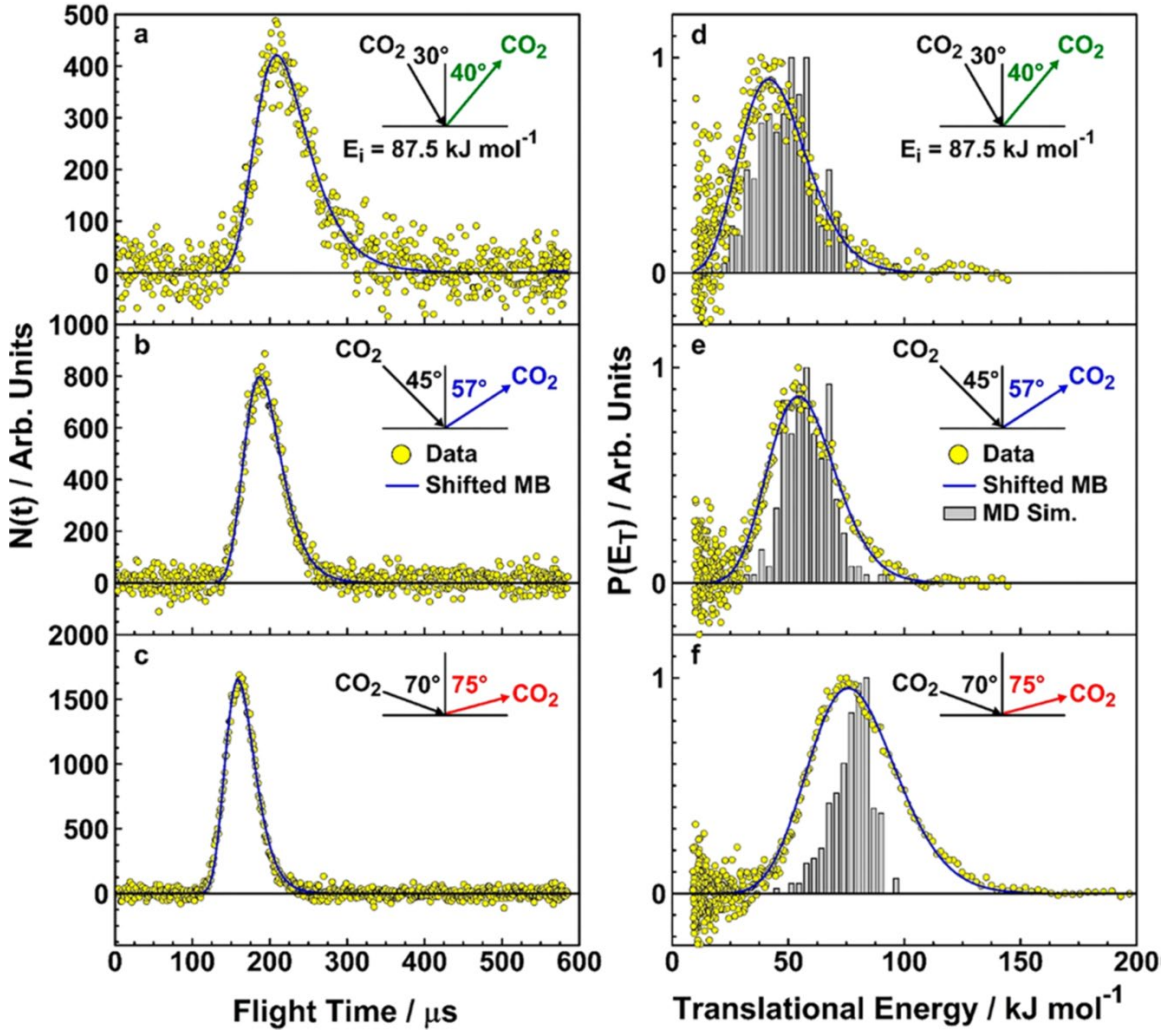

Figure 5. Representative TOF (a−c) and $P(E_T)$ (d−f) distributions for scattered CO_2, with $\langle E_i \rangle$ = 87.5 kJ mol^{-1}. Incidence (θ_i) and final (θ_f) angles corresponding to each distribution are shown. The yellow symbols represent the experimental data, and the blue lines represent the shifted, flux weighted MB distribution used to fit the IS component. The gray bars in the right column represent the simulated $P(E_T)$ distributions obtained from the MD simulations, where the trajectories were averaged over an angular range of ±3° in θ_f and ±3° from the scattering plane.

The trajectories were initiated with the gas molecules located far above the surface (Z_0 = 12.0 Å for H_2O and CO_2; Z_0 = 15.0 Å for GLY), where the molecule−surface interaction energy

is zero. The initial lateral (X and Y) position of the incident molecules within the surface unit cell was randomly chosen, and they were assumed to be in their equilibrium positions with the zero-point vibrational energy of the molecules ignored. The initial polar incidence angles, where the polar angle is defined as the angle between the initial velocity and the negative Z axis, were identical to those used in the experiment (θ_i = 30, 45, and 70° for H_2O and CO_2, θ_i = 45 and 70° for GLY). In addition, the incidence energies, E_i = 38.9, 87.5, and 149.5 kJ mol^{-1} for H_2O, CO_2, and GLY, respectively, were the same as the average incidence energies in the experiment. The incidence azimuthal angle was sampled randomly in the [0, 360°] range. The propagation time step was selected to be 0.2 fs for CO_2 and H_2O and 0.1 fs for GLY. Most trajectories conserved total energy within ~40 meV for CO_2 and H_2O and ~60 meV for GLY.

The trajectories were terminated after the scattered molecules reached a distance of Z_0 above the surface or after a maximum propagation time of 20 ps for CO_2 and H_2O and 40 ps for GLY. At the end of each scattering trajectory, the final translational energy, polar angle (θ_f, with respect to the surface normal), and the change in azimuthal angle, $\Delta\phi$, of the scattered molecule were evaluated. The rotational and vibrational energies of each scattered molecule were also determined. The rotation−vibration coupling was neglected in these calculations. The Cartesian coordinates $\vec{r_i}$ and momenta $\vec{p_i}$ in the center-of-mass (c.m.) frame were obtained directly from the classical trajectories. The angular velocity $\vec{\omega_i}$ was calculated by $\vec{\omega_i} = \mathrm{I}^{-1}\vec{L}$, where I is the moment of inertia tensor at $\vec{r_i}$ and $\vec{L} = \sum_i \vec{r_i} \times \vec{p_i}$ is the angular momentum. The vibrational energy consists of kinetic and potential energies. The former was determined by the vibrational velocities $\vec{v}^{nr} = \vec{v_i} - \vec{\omega_i} \times \vec{r_i}$ after the c.m. velocities were removed, while the latter was from the ReaxFF force field.

Three types of scattering mechanisms were identified and classified by the number of inner turning points (ITPs),[38-39, 113] defined as the negative to positive reversal of the normal component of the molecule's c.m. motion: impulsive scattering (IS, one ITP), extended impulsive scattering (EIS, more than one ITP), and trapping (T, still on the surface at the maximum simulation time). All the MD calculations were performed using the large-scale atomic/molecular massively parallel simulator (LAMMPS) software.[126] A total of 1000 trajectories were computed for each set of initial conditions for all three molecules.

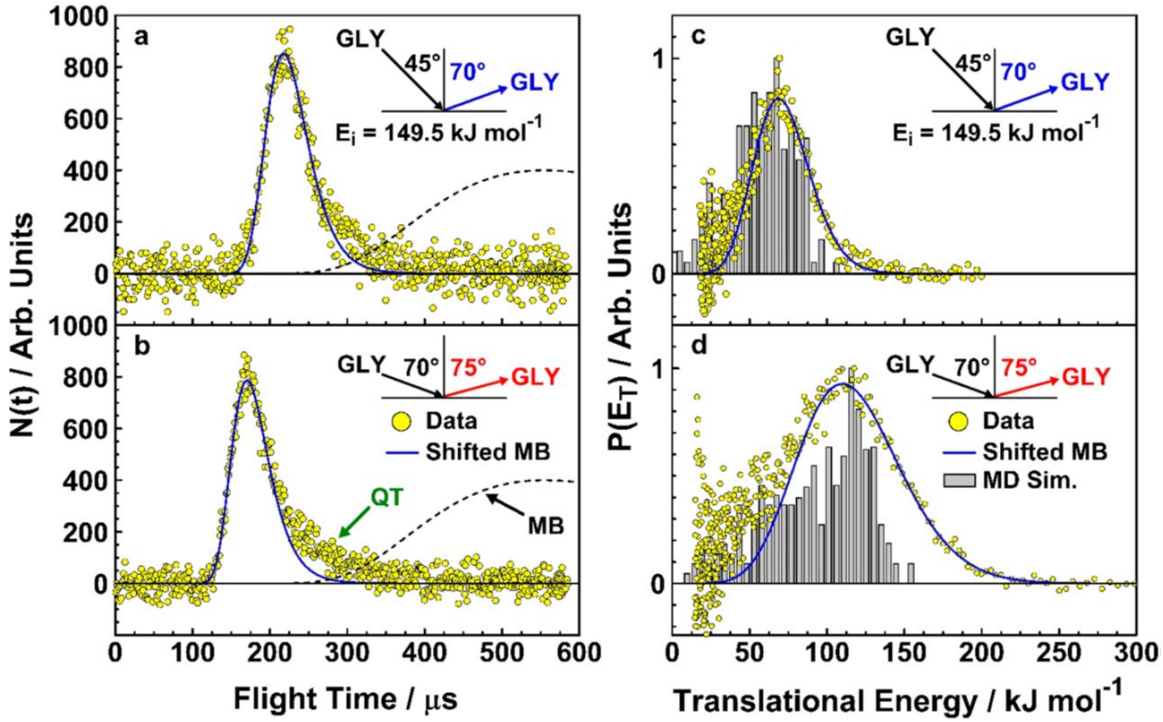

Figure 6. Representative TOF (a, b) and $P(E_T)$ (c, d) distributions for scattered GLY, with $\langle E_i \rangle$ = 149.5 kJ mol^{-1}. Incidence (θ_i) and final (θ_f) angles corresponding to each distribution are shown. The yellow symbols represent the experimental data, and the blue lines represent the shifted, flux weighted a MB distribution used to fit the IS component. The black, dashed lines represent MB distribution with T_s = 677 K. The green arrow in part b indicates the quasi-trapping (QT) component discussed in the text. The gray bars in the right column represent the simulated $P(E_T)$ distributions obtained from the MD simulations, where the trajectories were averaged over an angular range of ±3° in θ_f and ±3° from the scattering plane.

3.4 Experimental results

Figures 4−6 display representative TOF and P(E_T) distributions for H_2O, CO_2, and GLY, respectively. For every combination of θ_i and θ_f, the TOF and P(E_T) distributions of H_2O and CO_2 (Figures 4 and 5, respectively) contain only a single peak at short flight times ($100 < t < 200$ μs). This feature can be fit by a shifted, flux-weighted Maxwell−Boltzmann (MB) distribution,[103] which is represented by the blue lines in Figures 4 and 5. However, a shifted MB distribution cannot capture the entire TOF distribution for the scattered GLY (Figure 6), particularly for distributions collected with $\theta_i = 70°$. There is an additional component at long flight times ($t > 200$ μs) that grows in intensity and shifts to shorter flight times as θ_f increases (not shown). While this component represents GLY molecules that transfer a significant amount of translational energy during their interactions with the HOPG surface, the molecules do not come fully into thermal equilibrium with the surface and cannot be described by a MB distribution characterized by Ts (Figure 6, black dashed line). Similar behavior was observed recently for the scattering of nitromethane and methyl formate on HOPG (T_s = 677 K) and was classified as "quasi-trapping" (QT). In a QT interaction, the molecule's normal momentum is quickly accommodated to the surface temperature; however, the residence time of the molecule on the surface is too short for its parallel momentum to dissipate fully.[114] Consequently, the molecule scatters with a lobular angular distribution oriented away from the surface normal, and the ratio of average final translational energy to incidence energy, $\langle E_T \rangle / \langle E_i \rangle$, increases with θ_f. Because $\langle E_i \rangle$ of GLY was high (149.5 kJ mol^{-1}), the fraction of molecules that scattered via the QT mechanism (roughly 10 and 15% for θ_i = 45 and 70°, respectively) was considerably lower than the fraction of methyl formate and nitromethane molecules that scattered from HOPG by the QT mechanism (approximately 15 and 30% for $\theta_i = 45$ and 70°, respectively, with $\langle E_i \rangle \approx 100$ kJ mol^{-1}), making it difficult to distinguish the QT component clearly in the TOF distributions for GLY. The high $\langle E_i \rangle$ of GLY also resulted

in considerable overlap between the IS and QT components, further complicating their separation. Therefore, while there is evidence that some GLY molecules scatter via a QT mechanism, we will only consider the dynamics of the total scattered flux in our analysis. Thus, the fits shown in Figures 4−6 are for demonstrative purposes only.

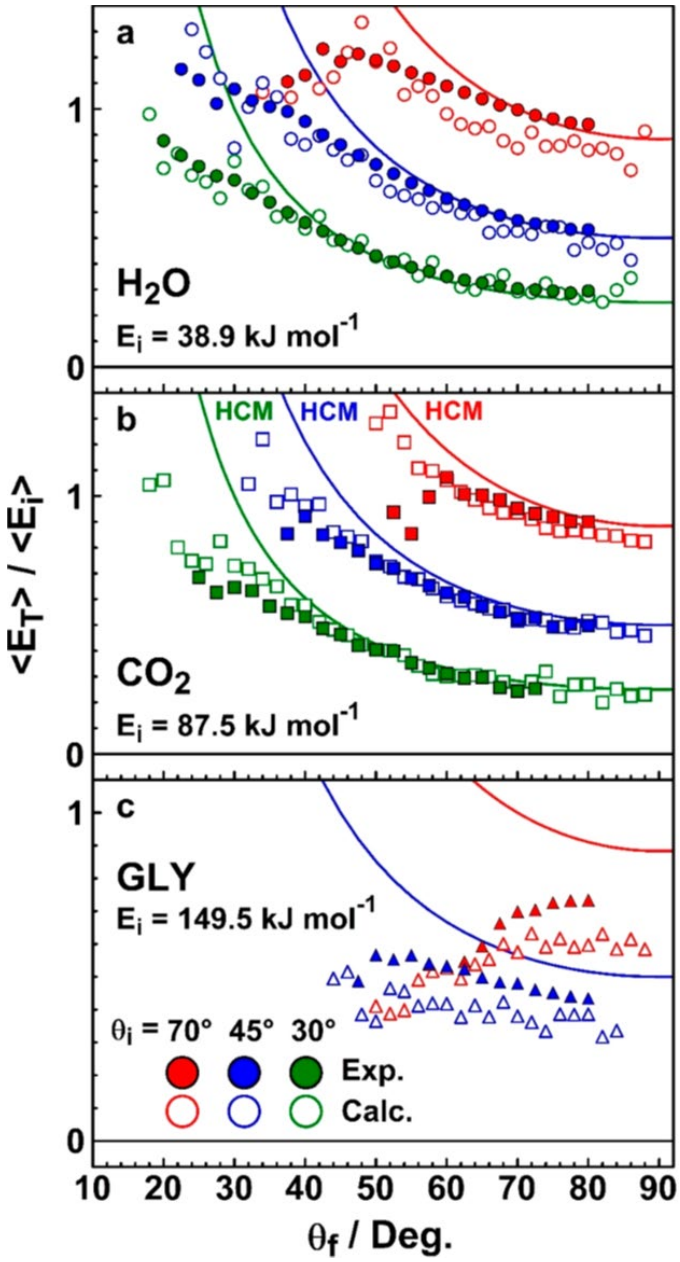

Figure 7. Ratios of average final energy to average incidence energy, $\langle E_T \rangle / \langle E_i \rangle$, as a function of θ_f for the total in-plane flux of scattered H_2O (a, circles), CO_2 (b, squares), and GLY (c, triangles), with $\theta_i = 70°$ (red symbols), 45° (blue symbols), and 30° (green symbols). The filled and open symbols represent the

experimental and simulated results, respectively. The solid lines indicate the values of $\langle E_T \rangle / \langle E_i \rangle$ when the incident parallel momentum of the molecule is conserved with $\theta_i = 70°$ (red line), 45° (blue line), and 30° (green line).

The experimental values of $\langle E_T \rangle / \langle E_i \rangle$ as a function of θ_f are shown in Figure 7 for H_2O (top panel, circles), CO_2 (middle panel, squares), and GLY (bottom panel, triangles). The solid lines represent the values of $\langle E_T \rangle / \langle E_i \rangle$ predicted by the hard cube model (HCM), which assumes that the incident parallel momentum of the molecule is conserved during the collision.[127] According to the HCM, the functional form of $\langle E_T \rangle / \langle E_i \rangle$ is $\sin^2\theta_i / \sin^2\theta_f$ when parallel momentum is conserved. For H_2O and CO_2, the angular dependence of $\langle E_T \rangle / \langle E_i \rangle$ follows the values predicted by the HCM at larger θ_f, suggesting that the incident parallel momentum of the molecule is retained during the collision. The experimental values of $\langle E_T \rangle / \langle E_i \rangle$ for H_2O are slightly higher than the predictions of the HCM, while the experimental values for CO_2 are slightly lower than the HCM predictions. For GLY, however, the dependence of $\langle E_T \rangle / \langle E_i \rangle$ on θ_f deviates significantly from the HCM prediction. When $\theta_i = 45°$, the experimental $\langle E_T \rangle / \langle E_i \rangle$ values agree with the general shape of, but fall below, the curve obtained from the HCM. When $\theta_i = 70°$, $\langle E_T \rangle / \langle E_i \rangle$ increases with θ_f, which is contrary to the results for H_2O and CO_2. Deviations in the predictions of the HCM were observed for the scattering of methyl formate and nitromethane from HOPG, which were attributed to scattering through the QT mechanism. In QT, each molecule−surface interaction likely increases the energy transfer to the surface, leading to lower values of $\langle E_T \rangle / \langle E_i \rangle$. However, even if the QT component is removed and only the energy of the IS molecules is considered, the dependence of $\langle E_T \rangle / \langle E_i \rangle$ on θ_f still falls below the HCM prediction (not shown).

Angular distributions as a function of scattered flux for H_2O (circles), CO_2 (squares), and GLY (triangles) are shown in Figure 8 for $\theta_i = 70$ (red symbols), 45 (blue symbols), and 30° (green symbols). The relative flux of scattered molecules with a given mass, I(molecule), can be

determined by integrating the quotient, N(t)/t, where N(t) is the relative number density (measured in a TOF distribution) and t is the flight time from the chopper wheel to the EI ionizer. To facilitate the comparison of their shapes, the angular distributions have been normalized to a value of 1.0. The θ_f at which the maximum flux occurs, θ_f^{max}, and the full width at half-maximum, FWHM, for each of the angular distributions are listed in Table 1. The angular distributions for H_2O have the lowest θ_f^{max} and the largest FWHM, presumably because the $\langle E_i \rangle$ for H_2O is the lowest of the three molecules studied.[128] The surface temperature therefore has a greater impact on the angular distributions of H_2O, shifting the scattered flux toward lower θ_f as energy transfer from the surface into translation of the exiting molecule helps to direct the H_2O molecules toward the surface normal. Still, θ_f^{max} is equal to the specular angle ($\theta_{spec} = \theta_i$) for $\theta_i = 70°$ and super specular ($\theta_f^{max} > \theta_{spec}$) for $\theta_i = 45$ and 30° despite the low $\langle E_i \rangle$. For CO_2, the angular distributions grow narrower, and θ_f^{max} values are super specular for all three θ_i. The angular distributions obtained for GLY have the narrowest angular distributions and the largest θ_f max of the three molecules studied.

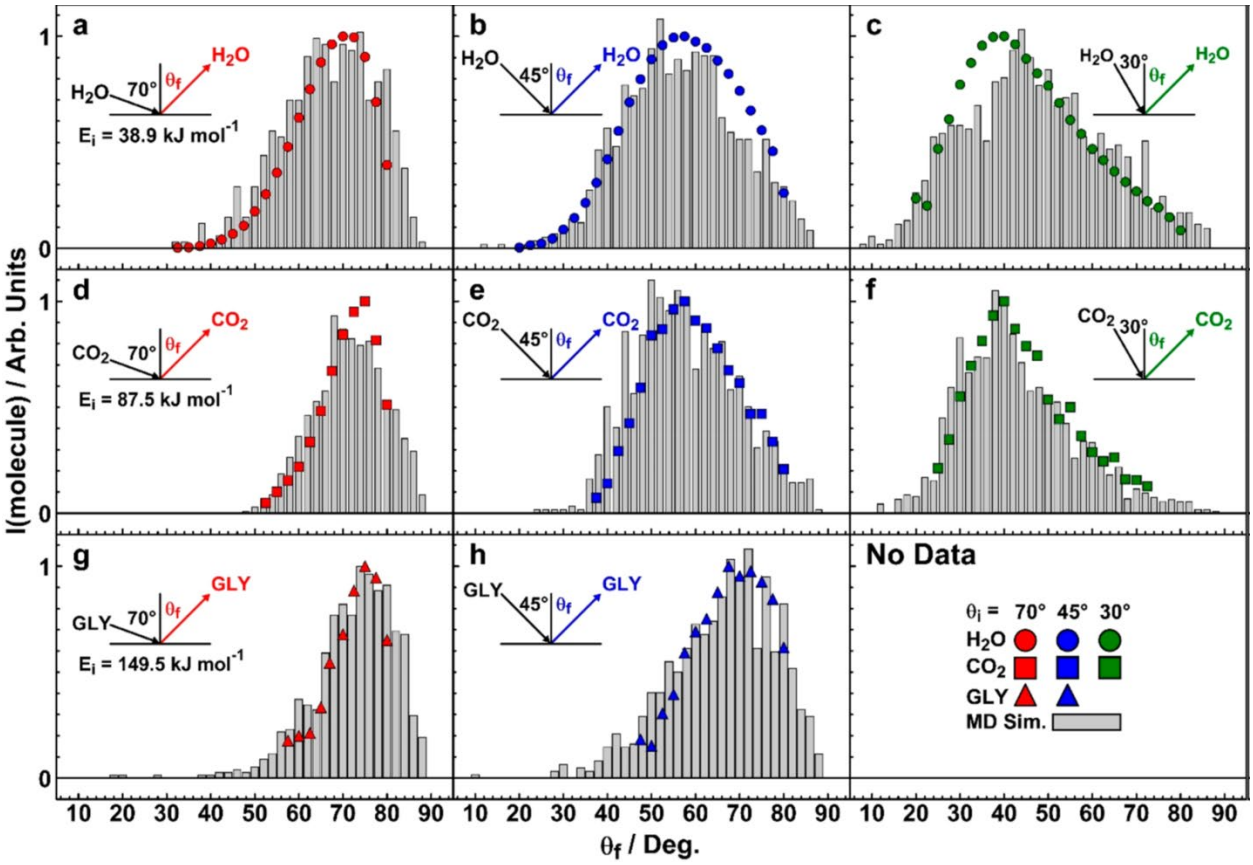

Figure 8. Experimental angular distributions for the total in-plane flux of scattered H_2O (a−c, circles), CO_2 (d−f, squares), and GLY (g, h, triangles), with θ_i = 70° (a, d, g, red symbols), 45° (b, e, h, blue symbols), and 30° (c, f, green symbols). The gray bars in the right column represent the simulated $P(E_T)$ distributions obtained from the MD simulations, where the trajectories were averaged over an angular range of ±3° in θ_f and ±3° from the scattering plane.

Table 1. θ_f^{max} and Full Width at Half Maximum, FWHM, of the Measured Angular Distributions Shown in Figure 8[a]

	θ_f^{max}/FWHM		
	θ_i = 70°	θ_i = 45°	θ_i = 30°
H_2O	70/21.2	57.5/34.9	38/33.3
CO_2	75/14.7	57.5/26.8	40.0/~23
GLY	75/~14.0	70/~24.1	-/-

[a]All values are given in degrees

3.5 Computational results

The interaction potentials between the incident molecules and the surface for different molecular orientations are shown in Figure 9. For H_2O (Figure 9a), the strongest interaction (−15.1 kJ mol^{-1}) corresponds to the two-leg structure with two hydrogens oriented toward the surface at an O-surface perpendicular distance of 3.01 Å. The one-leg structure with a single OH bond directed at the surface has a smaller adsorption energy of −12.5 kJ mol^{-1} and an O-surface perpendicular distance of 3.10 Å. The O-down structure with two H−O bonds pointing up is the least energetically favorable (−5.9 kJ mol^{-1}). The adsorption energy and geometry are in good agreement with a previous DFT calculation.[129] The adsorption energy is also comparable to the experimental water-surface interaction energy of −19.0 kJ mol^{-1} measured with microcalorimetry.[130] The preference for the two-leg adsorption structure is also consistent with previous calculations using various quantum chemical methods.[129, 131] The preferred H-down configurations are presumably a result of hydrogen bond-like interactions with the π electrons of graphene. For CO_2 (Figure 9b), the interaction is dominated by the adsorption configuration where CO_2 is parallel to the graphene plane. The depth of the interaction well is −19.0 kJ mol^{-1} for this orientation, which is consistent with the experimental values of −26.2 and −17.2 kJ mol^{-1} obtained from temperature-programmed desorption experiments.[132-133] The parallel structure has a larger adsorption energy than the perpendicular structure because of dispersion interactions between CO_2 and the surface. The interaction between GLY and graphene is more complex, because GLY can interact via different functional groups including the amino nitrogen (NH_2), the methylene (CH_2), the carbonyl oxygen (CO), the hydroxyl oxygen (OH), and parallel structures (PAR1 and PAR2), as shown in Figure 9c. The strongest interaction is for the PAR2 configuration with GLY oriented parallel to the surface and one N−H bond directed toward the surface; this configuration has an adsorption energy of −37.6 kJ mol^{-1}. This adsorption structure found using ReaxFF is similar to

the result from a previous DFT calculation, which found a somewhat larger adsorption energy of −47.3 kJ mol^{-1}.[134] It should be noted that the position of the repulsive wall in the PES is most important for capturing the correct scattering dynamics; however, the ReaxFF force field was not extensively tested in such regions. Consequently, we rely on extensive comparison with experimentally measured attributes to validate this approach.

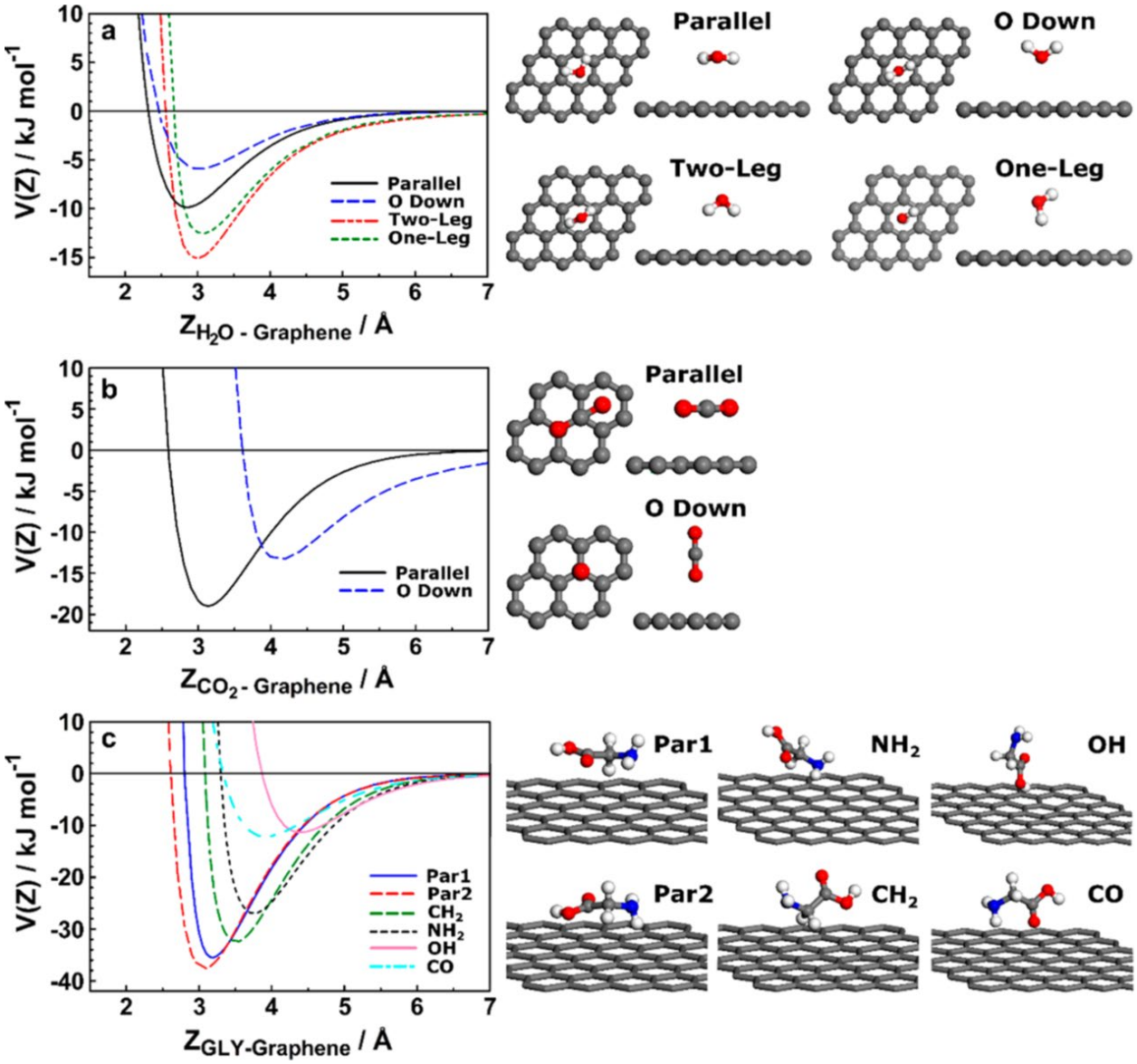

Figure 9. (a) ReaxFF interaction energy of H_2O with graphene as a function of H_2O-graphene distance for two-leg, one-leg, parallel, and O-down configurations. The Z distance is defined as the vertical distance between the averaged C position of the upmost graphene sheet and the O atom of the water molecule. (b)

ReaxFF interaction energy of CO_2 with graphene as a function of CO_2−graphene distance for parallel and O-down configurations. The Z distance is defined as the vertical distance between the graphene sheet and the C atom of the CO_2 molecule. (c) ReaxFF interaction energy of GLY with graphene as a function of GLY-graphene distance for different configurations. The Z distance is defined as the vertical distance between the graphene sheet and the c.m. of the GLY molecule.

The molecule−surface interaction potentials have a profound impact on the scattering dynamics, especially for GLY, whose interaction with the surface is highly anisotropic. As mentioned in section 4, IS trajectories involve a single collision with the surface, whereas EIS trajectories correspond to molecules that experience multiple collisions with the surface and escape before reaching thermal equilibrium. Some of the molecules do not exit the surface before the end of the simulations, which were run for 20 ps for H_2O and CO_2 and 40 ps for GLY. For the purposes of the simulations, these molecules are considered to be "trapped" (T) on the surface. Examples of the three types of trajectories are illustrated in Figure S1 of the Supporting Information for the three molecules studied. However, the exceedingly narrow experimental angular distributions for all three molecules are not consistent with the accumulation of molecules on the surface during the experiments. Thus, the molecules that are "trapped" on a 20−40 ps time scale would undoubtedly exit the surface if the simulations were extended to sufficiently long times. Additionally, the experimental $P(E_T)$ distributions show no indication of molecules that desorb thermally from the surface (with translational energies described by a MB distribution at the surface temperature), leading to the conclusion that "trapped" molecules do not reach thermal equilibrium with the surface before they eventually desorb. Nonthermal desorption after loss of incident perpendicular momentum, or momentary "trapping", on a surface has been referred to as QT and has been the focus of earlier studies.[103] Unfortunately, it is too costly to run the MD simulations beyond the current maximum time limits in order to identify the QT events, especially

for GLY. Figure 10 shows the percentages of the three trajectory types for H_2O, CO_2, and GLY. It is clear that the partitioning between the different trajectory types depends on θ_i. The percentage of IS scattering decreases with increasing θ_i, while EIS and T increase with increasing θ_i. This trend is similar to that of N_2 and O_2 scattering from HOPG.[38-39] For H_2O and CO_2, the IS mechanism dominates at when θ_i = 30 and 45°, and the EIS mechanism becomes important when θ_i = 70° . In contrast, EIS is dominant for GLY at both 45 and 70°. Within the maximum simulation time of 20 ps for H_2O and CO_2, and 40 ps for GLY, there are still small T percentages for CO_2 and GLY, but no T for H_2O even though it has the lowest E_i.

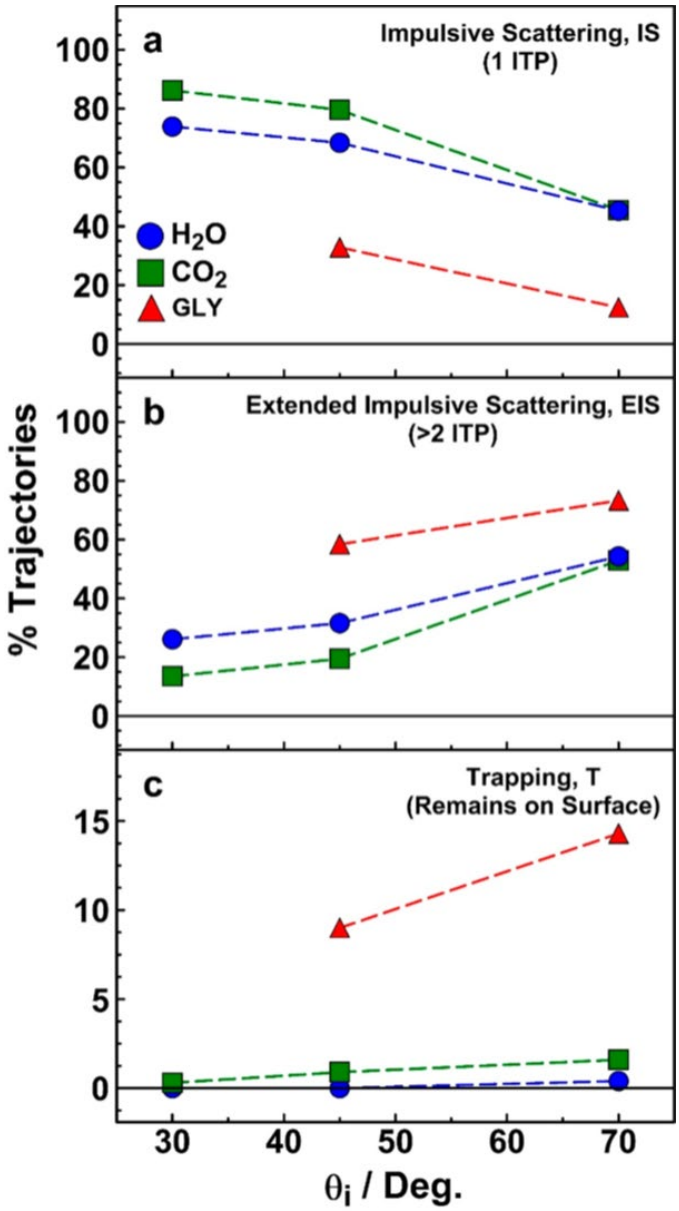

Figure 10. Percentage of molecules that undergo (a) impulsive scattering, IS, (b) extended impulsive scattering, EIS, and (c) trapping, T, obtained from the MD simulations for H_2O (blue circles), CO_2 (green squares), and GLY (red triangles).

Table 2. Calculated Average Polar and Azimuthal Angles, $\langle\theta_f\rangle$ and $\langle\Delta\phi\rangle$, and Full Width at Half Maximum, FWHM, of the Angular Distributions of Each Trajectory Type[a]

		IS			EIS			Total		
	θ_i	$\langle\theta_f\rangle$	FWHM	$\langle\Delta\phi\rangle$	$\langle\theta_f\rangle$	FWHM	$\langle\Delta\phi\rangle$	$\langle\theta_f\rangle$	FWHM	$\langle\Delta\phi\rangle$
H_2O	30	45.3	31.6	15.8	56.3	33.7	20.8	48.1	39.0	17.1
	45	55.6	27.7	10.0	61.9	27.6	13.8	57.6	29.4	11.2

	70	67.0	31.2	3.4	68.4	29.0	8.8	67.8	30.5	6.3
CO_2	30	45.0	24.2	9.8	58.3	19.9	16.6	46.8	25.6	10.7
	45	56.6	24.1	4.1	67.7	26.2	5.3	58.8	28.8	4.3
	70	70.6	18.5	2.0	74.1	18.1	3.0	72.5	20.3	2.6
GLY	45	67.8	27.9	6.0	67.0	24.8	19.2	67.3	28.2	14.4
	70	76.6	15.3	2.7	72.8	19.5	10.7	73.4	19.8	9.6

[a]All values are given in degrees

The $P(E_T)$ and angular distributions calculated for all three molecules are compared with the experiment results in Figures 4−6. The agreement is good and suggests that the MD models based on ReaxFF provide a reliable characterization of the scattering processes. It should be noted that the MD simulations assumed monoenergetic incident beams of molecules, whereas the molecules in the experimental beams had distributions of incident energies (Figure 2). This difference is probably responsible for the narrower $P(E_T)$ distributions from the calculations vs the experiments. The average polar angles $\langle\theta_f\rangle$ and average changes of the azimuthal angle $\langle\Delta\phi\rangle$ for the scattered molecules are listed in Table 2 for the IS and EIS mechanisms individually, and for all the scattered molecules, designated hereafter as "Total". Here $\Delta\phi = |\phi_f - \phi_i|$ is the final azimuthal angle with respect to the scattering plane. Most of the angular distributions are super specular ($\langle\theta_f\rangle > \theta_{spec}$), indicative of scattering events where some normal momentum is accommodated during the collision with the surface and parallel momentum is retained to some degree. As shown in Figure 8, the experimental angular distributions are well reproduced by theory, further validating the simulations based on ReaxFF. Because the experiment can only measure the angular distribution of the scattered molecules within the plane defined by the incident beam and the surface normal, no information is available for the product distribution as a function of the azimuthal angle. Nevertheless, such distributions were computed from MD simulations and they can be found in Figure S2. Most of the flux of the scattered molecules is within 2−20° of the scattering plane.

The calculated translational and rotational energy distributions of the scattered H_2O and CO_2 are displayed in Figure 11 for different θ_i. For the triatomic molecules, there is essentially no energy transferred into the vibrational modes. Additionally, their rotational excitation is small, as shown by the black, dotted lines in Figure 11. The minimal rotational excitation is the result of the flat surface which does not add a torque to the molecules as they collide with it.[135] The situation is more complex for GLY, the energy distributions of which are shown in Figure 12. Although rotational excitation in the scattered GLY remains small (black, dotted lines), there is significant vibrational excitation (blue, dashed lines). From the middle panel of Figure 12, it is clear that IS scattering of GLY contains relatively little vibrational energy. However, when GLY scatters via the EIS mechanism, a highly probable event, it possesses substantial vibrational energy. The vibrational energy of the GLY molecule continually increases while it interacts with the surface (see Figure S3). The vibrational energy initially increases at a faster rate than the translational energy decreases, suggesting that some of the vibrational excitation of the GLY originates from the surface. Indeed, the average total energy of the scattered GLY is larger than its E_i (denoted by the green, dashed-dotted lines in Figure 12), demonstrating that energy can flow from the hot surface to the molecule during multiple molecule−surface encounters.

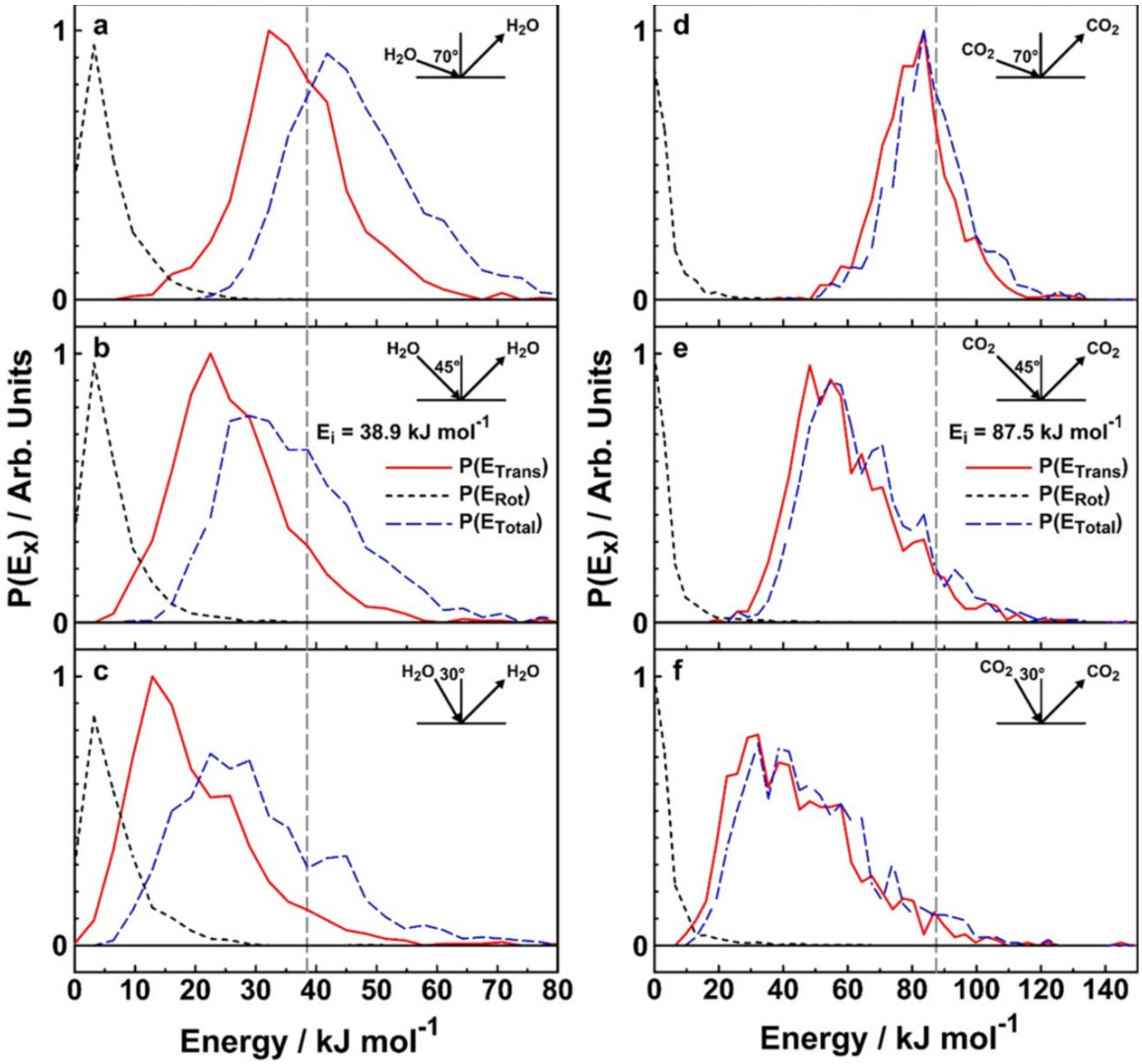

Figure 11. Simulated translational, $P(E_T)$, rotational, $P(E_{Rot})$, and total energy, $P(E_{Total}) = P(E_T) + P(E_{Rot})$, distributions, averaged over all scattered molecules, for H_2O (a−c) and CO_2 (d−f), with $\theta_i = 70°$ (a, d), 45° (b, e), and 30° (c, f). The gray dash lines denote the incident energies of the impinging H_2O and CO_2 molecules. No vibrational excitation was observed for H_2O or CO_2 that scattered from the surface.

In Table 3, the average translational energy ($\bar{E}_T$), internal energy ($\bar{E}_{int}$) of the scattered molecule, and average energy exchange between the molecule and surface ($\bar{E}_{ex} = E_i - \bar{E}_T - \bar{E}_{int}$) are presented as percentages of E_i. Note that when considering average energies, brackets are used to indicate average incidence energy in the experiment, $\langle E_i \rangle$, and average final translational energy, $\langle E_T \rangle$, at a given final angle, θ_f (see Figure 7, for example), whereas symbols with a bar overtop

indicate quantities that have been obtained by averaging over all the scattered molecules for all polar and azimuthal angles (e.g., $\bar{E}_T$, $\bar{E}_{int}$, $\bar{E}_{ex}$). A positive $\bar{E}_{ex}$ indicates that the molecule has transferred energy to the surface, while a negative $\bar{E}_{ex}$ indicates that the surface has transferred energy to the molecule. $\bar{E}_T$ increases rapidly with the increasing θ_i, while the $\bar{E}_{int}$ depends weakly on this angle. For IS, as discussed above, most of the incidence energy remains in translation. $\bar{E}_T$ for EIS is much lower than that for IS and more energy is partitioned into the internal modes of the molecule. Interestingly, some $\bar{E}_{ex}$ values are negative for large θ_i, particularly for GLY. As stated before, this result suggests that some energy flows from the surface to the molecule.

The distributions of the surface residence time, defined as the time required for a trajectory to enter and exit the scattering zone, are displayed in Figure 13. Here, the scattering zone is defined by the vertical distance of 4.5 Å between the molecule's c.m. and the surface plane (the topmost graphene layer). For IS trajectories, the typical residence time is a few hundred fs, depending on the E_i. However, the EIS molecules may reside on the surface for an extended time, as shown in Table 4. The residence time increases with θ_i, indicating that accommodation of $E_{n,i}$ is important. Interestingly, GLY has many trajectories that have very long residence times on the surface, up to 30 ps.

3.6 Discussion

The MD results based on ReaxFF are in good agreement with the experimental $P(E_T)$, angular, and $\langle E_T \rangle / \langle E_i \rangle$ distributions (Figures 4−8), giving confidence in the rich details of the scattering trajectories that are illuminated by the MD simulations. Similar to previous studies, the simulations have identified three distinct trajectory types for molecules scattering from the surface, which we designate as IS, EIS, and T.

The partitioning between the three mechanisms depends on θ_i (Figure 10) or, more specifically, $E_{n,i}$. As θ_i increases, the fraction of molecules that scatter via the IS mechanism decreases and the probability of observing molecules scattered by the EIS and T mechanisms increases. This dependence on θ_i is linked to the extent to which $E_{n,i}$ is retained during a molecule's interaction with the surface. Focusing for the time being on the scattering dynamics of the triatomics, H_2O and CO_2, the calculated average final translational energies, $\bar{E}_T$, for the IS and EIS trajectories of both molecules differ by less than 20%, even though the molecules that scatter via the latter mechanism undergo multiple interactions with the surface before leaving it (Table 3). As can be seen in Table 5, CO_2 and H_2O that scatter by the IS and EIS mechanisms retain 80−95% of their parallel energy, depending on θ_i, which is indicative of scattering events that tend to conserve parallel momentum. With the smooth HOPG surface and the consequently weak in-plane forces acting on an incident molecule, even if it interacts with the surface more than once, conservation of parallel momentum is not surprising. Therefore, the HCM, which assumes that the incident parallel momentum of the molecule is conserved during the gas−surface interaction, well describes the experimental energy transfer data displayed for H_2O and CO_2 in Figure 7. When parallel momentum is essentially conserved and normal momentum is not, then the angular distribution of the scattered molecules is expected to be super specular ($\langle\theta_f\rangle > \theta_{spec}$). Indeed, angular distributions of IS and EIS H_2O and CO_2 are super specular, suggesting that these molecules lose a significant fraction of their $E_{n,i}$ during their interactions with the surface. Furthermore, the angular distributions of H_2O and CO_2 that scatter by the EIS channel are oriented farther beyond the specular angle than those that scatter by the IS mechanism (Table 2), implying that molecules undergoing multiple collisions with the surface transfer more normal energy than molecules that scatter after a single collision. For H_2O and CO_2, the translational energy and angular distributions

of the molecules that scatter by the EIS mechanism are not clearly distinguishable from those that scatter via the IS channel. Consequently, it is not possible to identify these scattering mechanisms in the experimental results, and we must look to the MD simulations for the details.

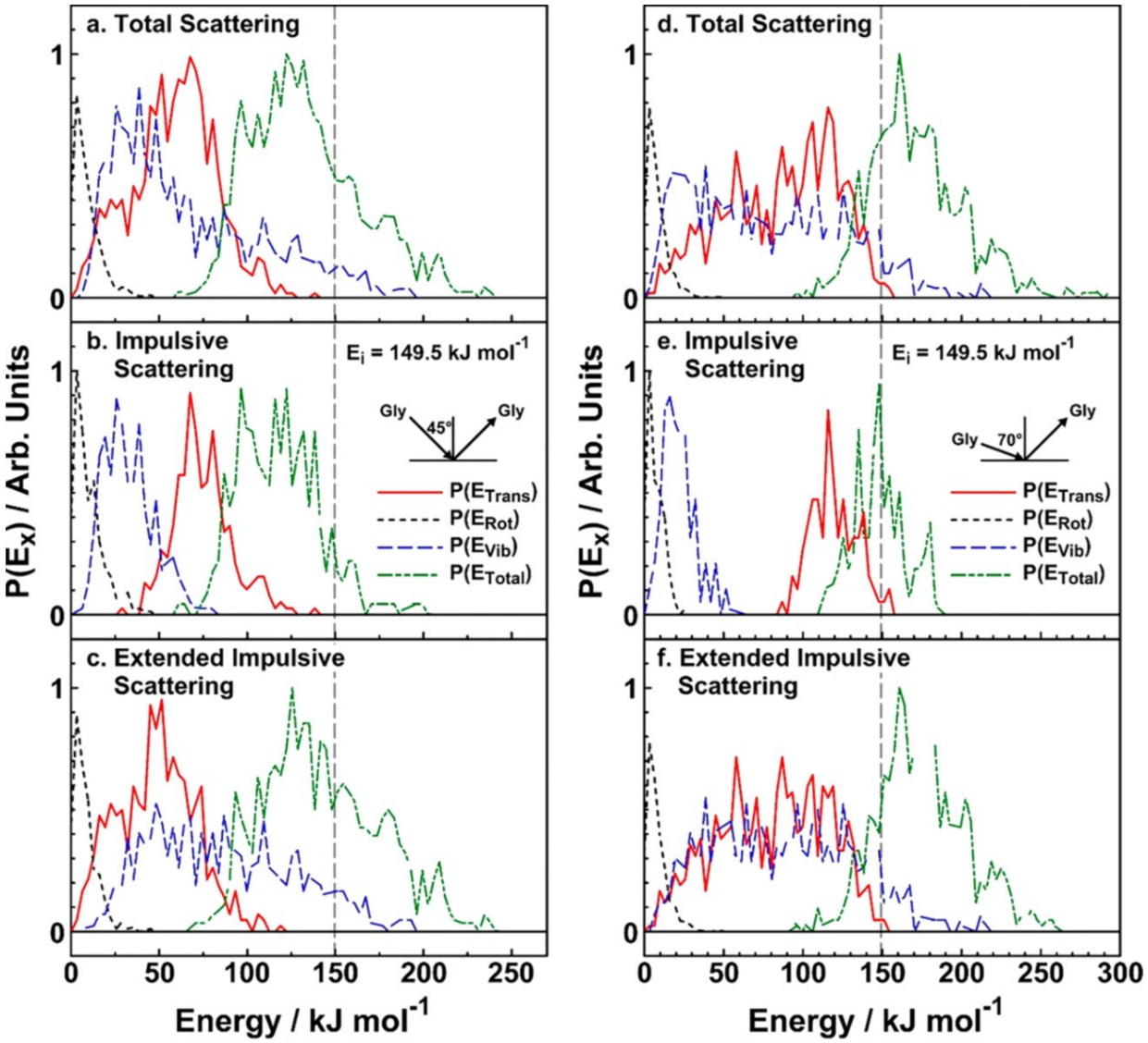

Figure 12. Simulated translational ($P(E_T)$, solid red lines), rotational ($P(E_{Rot})$, dotted black lines), vibrational ($P(E_{vib})$, blue dashed lines), and total energy ($P(E_{Total}) = P(E_T) + P(E_{Rot}) + P(E_{Vib})$, green dash-dotted lines) distributions averaged over all scattered GLY molecules, with $\theta_i = 45°$ (a−c) and 70° (d−f). The gray dashed lines denote the incident energy of the impinging GLY molecules.

Table 3. Calculated Average Translational and Internal Energies ($\bar{E}_T$ and $\bar{E}_{int}$) for the Scattered Molecules and Average Energy Exchange ($\bar{E}_{ex}$), As Percentages of E_i, for Different Scattering Mechanisms[a]

		IS			EIS			Total		
	θ_i	$\bar{E}_T$	$\bar{E}_{int}$	$\bar{E}_{ex}$	$\bar{E}_T$	$\bar{E}_{int}$	$\bar{E}_{ex}$	$\bar{E}_T$	$\bar{E}_{int}$	$\bar{E}_{ex}$
H_2O	30	55.8	17.9	26.3	36.8	34.6	28.6	50.8	22.3	26.9
	45	72.0	15.2	12.8	57.0	33.5	9.5	67.4	21.0	11.4
	70	101.2	12.9	−14.1	86.8	32.6	−19.4	93.4	23.7	−17.1
CO_2	30	53.3	6.0	40.7	33.4	7.1	59.5	50.6	6.1	43.3
	45	71.4	5.7	22.9	55.0	6.5	38.5	68.2	5.9	25.9
	70	97.9	5.3	−3.2	88.6	5.4	6.0	92.9	5.3	1.7
GLY	45	50.0	30.9	19.1	32.4	69.7	−2.1	38.7	55.7	5.6
	70	79.9	20.6	−0.5	53.7	65.6	−19.3	57.4	59.1	−16.7

[a] θ_i values are given in degrees and E values in kJ mol^{-1}.

The experiment is, however, able to distinguish a QT scattering component that would presumably include trajectories designated in the simulations as EIS and T (see Figure 6). While some GLY molecules recoil from the surface after a single collision (Figure 10), the majority of these molecules tumble along the surface for several picoseconds before scattering into the vacuum, transferring a significant amount of energy in the process. Despite the long residence time, EIS GLY molecules do not come into thermal equilibrium with the surface, and they scatter with a lobular angular distribution (Table 2). The average final angles of the angular distributions of the EIS GLY molecules are 4° lower than those for IS GLY, because the GLY molecules that interact with the surface repeatedly transfer more parallel energy than those that recoil after a single collision (Table 5). This result is contrary to the results for H_2O and CO_2, where $\langle\theta_f\rangle$ for the EIS trajectories is larger than those for the IS trajectories. However, even though the energy transfer for EIS GLY is large, the translational energy distributions for EIS and IS GLY still overlap substantially (Figure 12), which is probably the reason why two distinct scattering mechanisms cannot be clearly distinguished in the experimental TOF and $P(E_T)$ distributions (Figure 6). Nevertheless, the angular dependence of the energy ratio, $\langle E_T\rangle/\langle E_i\rangle$, does suggest that the GLY molecules interact strongly, and presumably repeatedly, with the surface (Figure 7c). Thus, the

experimental and closely matching computational results both yield $\langle E_T \rangle / \langle E_i \rangle$ ratios that are significantly below the ratios predicted by the HCM. As indicated by Table 5, the parallel energy of GLY is not conserved during the molecule−surface interaction, particularly for the EIS channel, which is the dominant scattering mechanism for GLY. The energy loss in the parallel direction is likely the result of the strong anisotropy of the GLY molecule, which interacts with the HOPG through different functional groups, as shown in Figure 9c. Clearly, the scattering dynamics of GLY on HOPG are more complex than those for H_2O and CO_2.

The angular dependencies of the $\langle E_T \rangle / \langle E_i \rangle$ ratios for H_2O and CO_2 roughly follow the predictions of the HCM at larger θ_f, while those for GLY are qualitatively different than the HCM prediction at all θ_f. H_2O retains the most translational energy of the three molecules, and its $\langle E_T \rangle / \langle E_i \rangle$ ratios slightly exceed the ratios predicted by the HCM when θ_f is large (Figure 7a). Moreover, the calculated $\bar{E}_T$ exceeds Ei for H_2O when $\theta_i = 70°$ (Table 3). Similar results have also been observed for H_2O scattering from graphite ($\langle E_i \rangle$ = 3.38 kJ mol^{-1}; $\theta_i = 40°$; T_s = 300 K) and N_2 scattering from HOPG ($\langle E_i \rangle$ = 30.3 and 67.9 kJ mol^{-1}; θ_i = 30, 45, and 70°; T_s = 677 K).[38] This unusual result arises because the normal incidence energy of H_2O is low ($E_{n,i}$ = 4.55 kJ mol^{-1}; θ_i = 70°) in comparison to the energy of the surface ($2RT_s$ = 11.3 kJ mol^{-1}). Consequently, energy is transferred from the hot surface into the translational energy of the molecule along the surface normal as is evident by the $\bar{E}_\perp > 100\%$ in Table 5. The significant normal energy transfer to scattered H_2O with $\theta_i = 70°$ results in the average final angles for both IS and EIS mechanisms being slightly lower than θ_{spec} (Table 2). Normal energy transfer from the surface also occurs for CO_2 that scatters via the IS mechanism when $\theta_i = 70°$ (Tables 3 and 5), although the magnitude of this energy transfer is lower than for H_2O because the normal incidence energy of CO_2 is a higher fraction of 2RTs. In general, the $\langle E_T \rangle / \langle E_i \rangle$ ratios for CO_2 are slightly lower at large values of θ_f

than those predicted by the HCM (Figure 7b). In contrast to the $\langle E_T \rangle / \langle E_i \rangle$ ratios for H_2O and CO_2, these ratios for GLY are significantly lower than those predicted by the HCM (Figure 7c) even though the angular distributions are still super spectacular.

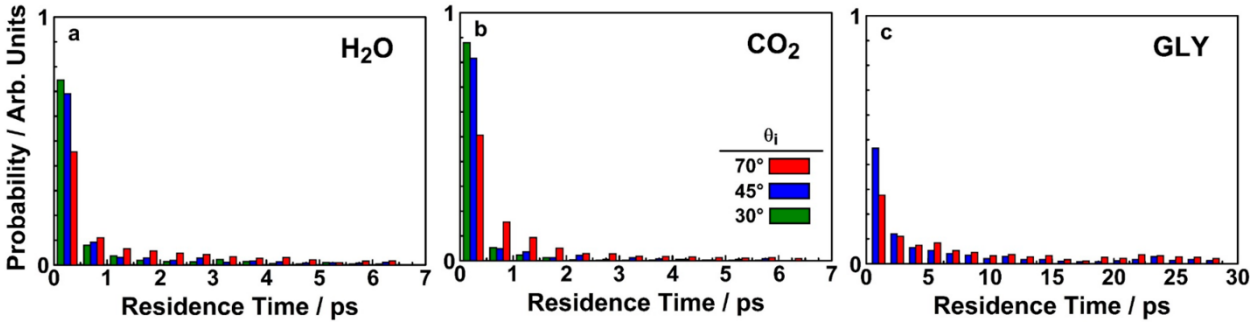

Figure 13. Distributions of residence times for (a) H_2O, (b) CO_2, and (c) GLY scattering, with $\theta_i = 70°$ (red bars), 45° (blue bars), and 30° (green bars). Molecules that scattered by the IS and EIS mechanisms are included.

Table 4. Average EIS Residence Times (ps) for H_2O, CO_2, and GLY

	$\theta_i = 30°$	$\theta_i = 45°$	$\theta_i = 70°$
H_2O	0.89	1.12	1.87
CO_2	0.47	0.72	1.40
GLY	–	5.68	8.53

Table 5. Average Normal and Parallel Translational Energies (kJ mol^{-1}) As Percentages of Incidence Normal and Parallel Translational Energy, Respectively, for CO_2, H_2O, and GLY[a]

		IS		EIS		Total	
	θ_i	$\bar{E}_\perp$	$\bar{E}_\parallel$	$\bar{E}_\perp$	$\bar{E}_\parallel$	$\bar{E}_\perp$	$\bar{E}_\parallel$
H_2O	30	39.9	94.9	18.1	93.4	34.2	94.6
	45	52.0	89.3	30.2	84.0	45.2	87.6
	70	165.1	90.9	125.1	78.5	143.3	84.2
CO_2	30	59.5	93.3	15.1	88.7	36.4	92.7
	45	50.2	92.9	19.8	90.3	44.3	92.4
	70	113.0	95.9	71.3	90.8	90.7	93.1
GLY	45	18.6	81.6	11.5	54.4	14.1	63.7
	70	49.1	84.3	45.6	55.0	46.1	59.3

[a] θ_i is given in degrees.

The $\langle E_T \rangle / \langle E_i \rangle$ ratios demonstrate the sensitivity of the scattering dynamics to the interaction potential of the system. It has been suggested that molecules with a deeper potential well are accelerated faster toward the surface and subsequently exchange more translational energy during the collision.[103, 136] H_2O would thus be expected to experience the least energy transfer because it has the weakest interaction with the surface. Indeed, Figure 9, Figure 7, and Table 3 show that H_2O does retain a slightly higher fraction of its translational energy than does CO_2. Our previous results also support this simple picture, as the energy transfer for N_2 scattering from HOPG was even less than found here for H_2O, presumably because the N_2−HOPG potential has a very shallow well depth of only 0.605 kJ mol^{-1}.[38] GLY has a much stronger interaction with the surface than do H_2O and CO_2 and would thus be expected to transfer more energy than either of these smaller molecules. This prediction is also supported by the data presented in Figure 7 and Table 3. While the correlation between the increased energy transfer and a stronger molecule−surface interaction provides an intuitive approach for predicting relative energy transfer, it oversimplifies the energy transfer mechanisms revealed by the simulations. The simulations show that scattered H_2O has the highest translational energies relative to E_i because the normal energy of the incident molecule is low in comparison to the energy available from the surface and energy is transferred from the surface to the exiting molecule. The energy difference between the $E_{n,i}$ and the energy available from the surface thus impacts the energy transfer dynamics significantly. Additionally, the simulations show that the high degree of translational energy transfer observed for GLY occurs because the molecule cannot escape the potential well immediately after the initial molecule−surface encounter and tumbles along the surface, increasing the likelihood of energy transfer before the molecule eventually scatters back into the vacuum.

Previous work conducted by the Hase group found that the residence time of O_2 colliding with HOPG decreased with increasing $\langle E_i \rangle$.[113] The MD simulations performed in the present study extend the results of Hase and co-workers and show that for a given $\langle E_i \rangle$ the residence time increases with θ_i, suggesting that the residence time is a function of the $E_{n,i}$ of the impinging molecule (Table 4). However, contrary to the findings of the Hase group, GLY has the longest residence time despite having the highest $\langle E_i \rangle$. This observation is a direct result of the molecule−surface interaction potential, which determines the residence time (τ) through the relationship $\tau \propto \exp(\varepsilon/RTs)$,[137] where ε is the depth of the attractive well. Thus, for a given T_s, a stronger molecule−surface interaction will result in a longer residence time. However, H_2O has a longer residence time than CO_2 despite having a weaker attraction with the surface, most likely because it has a lower E_i. It is reasonable to assume that there is a competition between the E_i dependence reported previously by Hase and co-workers and the influence of the interaction potential on surface interaction time.

The extended interaction time has interesting consequences for the energy transfer dynamics of the GLY-HOPG system. Internal excitation of the scattered molecule is more efficient for EIS vs IS GLY; nevertheless, internal excitation is only weakly dependent on θ_i, as shown in Table 3, indicating that it is mediated more by the surface than by the E_i of the beam. In our previous studies of nitromethane and methyl formate scattering from HOPG, vibrational excitation was suggested to be more efficient for the quasi-trapping (QT) mechanism, where the molecule interacts with the surface for an extended period of time, than for the IS mechanism. Likewise, the current MD simulations show that vibrational excitation is more efficient when the molecule has a long interaction time with the surface (Figure 12 and Table 3). Such energy transfer has been reported for gas phase collisions between peptide ions and rare gas atoms at low impact parameter,

which deposits some energy in low frequency backbone bending modes of the peptide ions.[138] In our case, it is possible that the low frequency vibrational modes of GLY are excited by the phonon modes of the graphene surface, which extend to ~1500 cm^{-1}.[139] It has been suggested that this is possible when the vibrational modes of the molecule have similar frequencies as the phonon modes of the surface.[140] However, if energy transfer from phonon modes were the dominant mechanism for excitation, we would expect to see vibrational excitation of CO_2, which has a relatively low frequency bending mode, yet vibrational excitation of CO_2 was not observed in the simulations. From Figure S3, it can be seen that the vibrational energy of GLY continually increases as the molecule interacts with the surface. The longer the molecule is in contract with the surface, the higher the probability that energy will flow from the surface into the internal modes of the molecule. Therefore, it seems that the residence times of EIS H_2O and CO_2 are too short for vibrational excitation. Because the triatomic molecules are weakly attracted to surface, they have short residence times, which would thus be expected to limit energy transfer into internal modes.

The large energy transfers for both the translational and vibrational degrees of freedom in GLY that scatters by the EIS mechanism arise because the graphene surface is soft and the adsorption energy is large. The extended residence time of the EIS channel allows the GLY to dissipate its hyperthermal translational energy into both molecular internal modes and surface phonons. Additionally, the vibrational modes of GLY gain energy from the hot surface, as the internal energy of the molecule increases faster than its translational energy decreases (Figure S3). However, the energy transfer processes are unclear, as it is impossible to track precisely where the energy flows in the system. To complicate matters further, it is possible that the EIS GLY is excited directly during its initial interaction with the surface. Thus, the normal component, and possibly

even the parallel component, of E_i can play a role in excitation of GLY that scatters via the EIS mechanism.

It is interesting to note that IS GLY is also highly vibrationally excited (Table 3 and Figure 12). In addition, the amount of vibrational excitation for the IS GLY increases as θ_i decreases (Table 3). Such a dependence on energy transfer was first reported by Kay et al.[105] and was determined to originate from a "squeezed atom" mechanism which resulted in direct translational to vibrational (T→V) energy transfer.[141] Vibrational excitation of the umbrella mode of NH_3 scattering from Au(111) was found to increase linearly when $E_{n,i}$ was above a threshold energy that corresponded to the energy of the vibrational level being excited. The lower the energy of the vibrational level, the lower the threshold energy.[141] This process was not affected by T_s. Direct T →V energy transfer has also been observed for high incidence energy (E_i > 1000 kJ mol^{-1}) protonated amino acids colliding with diamond and F-SAM surfaces.[104] A similar mechanism may play a role in the vibrational excitation of GLY. There are several low energy vibrational modes in GLY and the incidence energy is high enough to lead to direct T → V transfer. An exclusively T → V transition requires the surface to be rigid, or the surface atoms must at least be very heavy in comparison to the mass of the incident molecule. However, the graphene surface is flexible, and the GLY and carbon atoms of the surface have similar masses. Therefore, vibrational excitation in GLY might not be exclusively the result of direct T→V transfer, as the surface certainly participates in the energy transfer. Although direct excitation of the vibrational modes undoubtedly occurs when GLY strikes the surface, it cannot be easily separated in simulations where the surface is allowed to move. This difficulty occurs because C is too light and does not participate in the momentum transfer, even if there is only a single collision. To examine the effect of surface motion on T → V energy transfer, we carried out a simulation of GLY scattering from a rigid graphene

surface with E_i = 149.5 kJ mol^{-1} and θ_i = 70°. The results, presented in Figure S4, indicate that T → V energy transfer is quite facile, suggesting that direct T → V energy transfer may be important for GLY scattering via the IS mechanism.

The experimentally validated MD simulations presented here illuminate the subtle details of the scattering dynamics for a relatively complex organic molecule, such as GLY. This information adds to our knowledge base of molecule−surface scattering dynamics and can be applied to the development an efficient neutral-gas concentrator. Previously, it was determined that collisions that lead to a narrow and specular or super specular angular distribution will result in a higher concentration factor.[101] However, results from the current study demonstrate that even if the angular distribution is favorable, the energy transfer experienced by polyatomic molecules may introduce further complications that can affect the efficiency of the concentrator. Molecules with a stronger attraction to the concentrator surface will transfer more translational energy, either into the surface or into internal excitation of the molecules. As these molecules propagate down the length of the concentrator, they will slow down and trap more easily upon successive collisions, which will lead to rapid thermal equilibration of the molecules and consequent lowering of their concentration factor through thermal desorption of the molecules in a cos(θ_f) distribution. In addition, partitioning of energy into the vibrational modes of a molecule might result in its dissociation,[106] resulting in a loss of identity of the molecule that entered the concentrator. Even if the incoming molecules do not dissociate, if they retain high internal excitation up to the point where they are ionized by electron impact, then the fragmentation pattern would change and further complicate the identification of a tenuous atmosphere by mass spectrometry. In light of the new results presented here, a full picture of the scattering dynamics for atoms and molecules, especially

larger life-signature molecules such as amino acids and polypeptides, needs to be considered when designing and modeling an effective and efficient neutral gas concentrator.

3.7 Conclusion

The scattering dynamics of H_2O, CO_2, and GLY on an HOPG surface held at T_s = 677 K have been investigated with the use of a combination of beam-surface scattering techniques and MD simulations based on ReaxFF. This study was undertaken as part of a larger effort aimed at evaluating the efficacy of a neutral-gas concentrator intended for the study of tenuous atmospheres by mass spectrometry. For θ_i = 30, 45, and 70°, there was no evidence that the molecules exited the surface via a thermal desorption mechanism, though a small fraction (~10%) of the GLY molecules scattered via a quasi-trapping mechanism. All three molecules scattered from the surface with narrow angular distributions. The angular dependencies of the energy ratio, $\langle E_T \rangle / \langle E_i \rangle$, for H_2O and CO_2 were well described by the hard cube model at large final angles, suggesting that the molecules retained their parallel momentum during their interactions with the surface. In contrast, the energy transfer for GLY deviated significantly from the hard-cube model, suggesting that its parallel momentum was not retained.

The simulated $P(E_T)$ distributions, angular distributions of the $\langle E_T \rangle / \langle E_i \rangle$ ratios, and angular distributions of scattered flux agreed well with the corresponding experimental distributions, thus validating MD as a predictive tool for molecular scattering dynamics from HOPG. Analysis of the individual trajectories revealed that the molecules scatter from the surface via three mechanisms that can be distinguished by the number of inner turning points: impulsive scattering (IS, one ITP), extended impulsive scattering (EIS, multiple ITPs), and trapping (T, does not exit the surface before the end of the simulation). H_2O and CO_2 scattered predominantly by the IS mechanism when θ_i was 30°, and the EIS mechanism became increasingly important when θ_i went from 45 to

70°. The EIS mechanism was dominant for GLY regardless of θ_i. For H_2O and CO_2, the scattering dynamics of the IS and the EIS pathways were difficult to distinguish without visualizing the trajectories. By contrast, the IS and EIS mechanisms for GLY were subtly distinct in the MD simulations. The GLY that scattered by the EIS mechanism resided on the surface for several picoseconds, which enhanced translational energy transfer from the molecule to the surface and allowed the molecule to become vibrationally excited. No vibrational excitation was observed for H_2O and CO_2 that scattered from the surface.

The differences in the observed scattering dynamics for the three molecules studied demonstrate the importance of the molecule−surface interaction potential to the concentration of gases for characterization of tenuous atmospheres. A stronger molecule−surface interaction, as would be expected for larger molecules, will result in more energy transfer during the molecule−surface interaction and a longer residence time of the molecule on the surface. In the case of GLY, the molecule generally tumbles along the surface for several picoseconds before desorbing. Even though GLY retains some parallel momentum and scatters with a lobular angular distribution, which are desirable scattering dynamics for a concentrator, the increased energy transfer will ultimately lead to more trapping as the molecule experiences secondary, tertiary, etc. collisions on the walls of the concentrator. On the basis of the insight gained through the current study and other recent gas−surface scattering studies,[38, 104] we conclude that designs that reduce the surface residence time of the incoming molecules and the number of interactions they have with the walls of the concentrator will improve the efficacy of the device and make it more suitable for detecting a large variety of atoms and molecules.

3.8 Supporting information

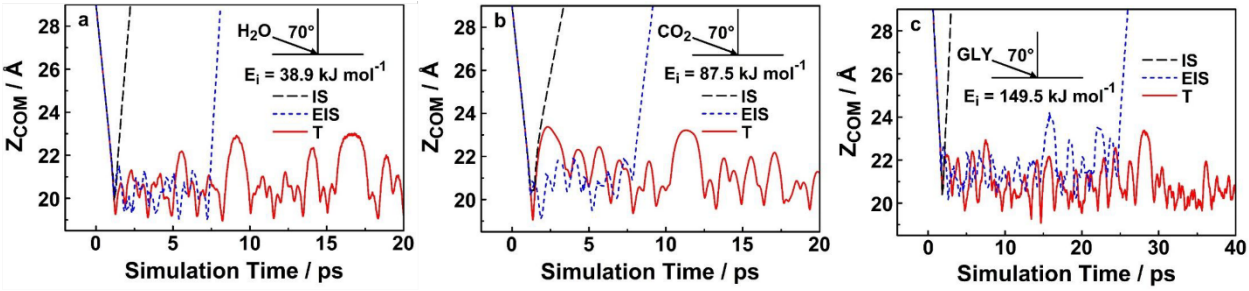

Figure S1. Representative trajectories displaying the center-of-mass motion along the Z direction for the three different scattering mechanisms, for (a) H_2O, (b) CO_2, and (c) GLY incident on the surface with θ_i = 70°.

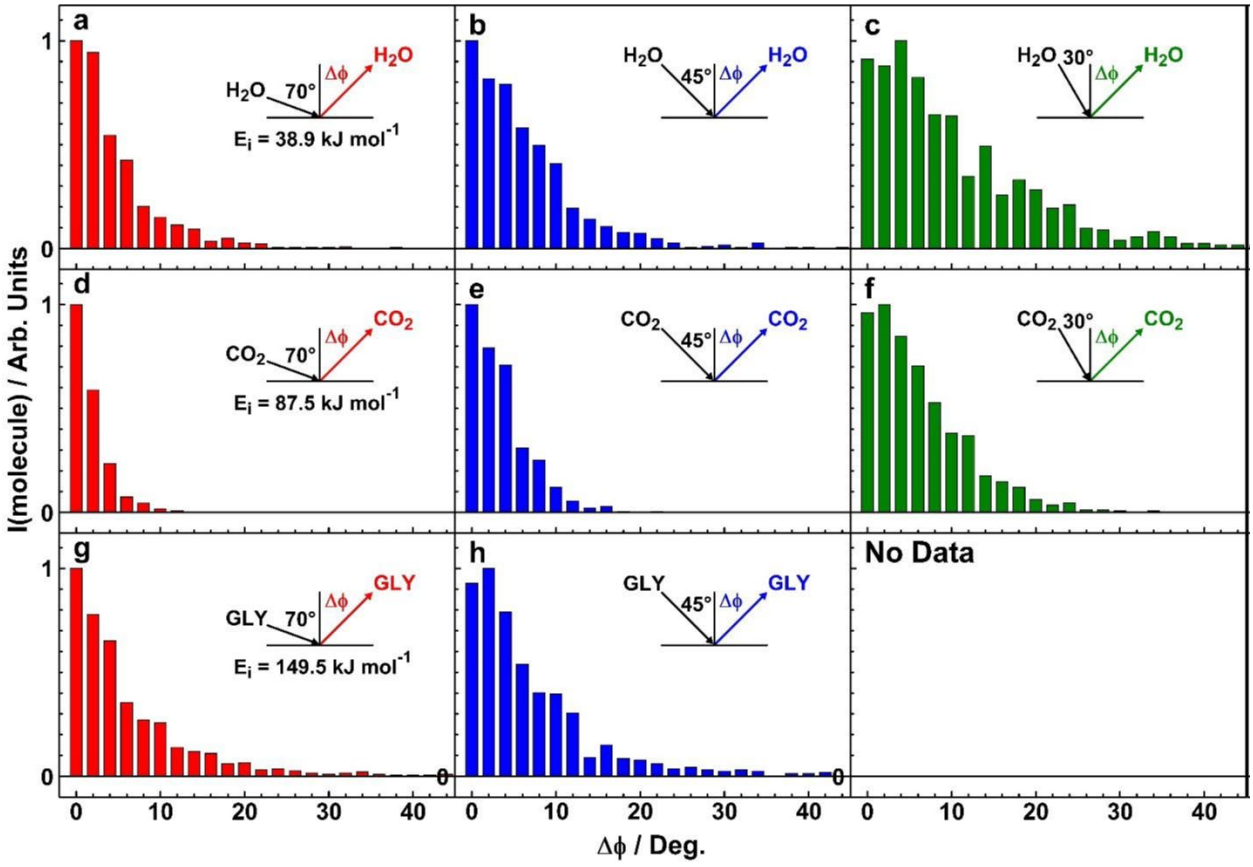

Figure S2. Simulated angular distributions for the total flux that is scattered out-of-plane for H_2O (a – c), CO_2 (d – f), and GLY (g, h), for θ_i = 70° (a, d, g, red bars), 45° (b, e, h, blue bars), and 30° (c, f, green bars).

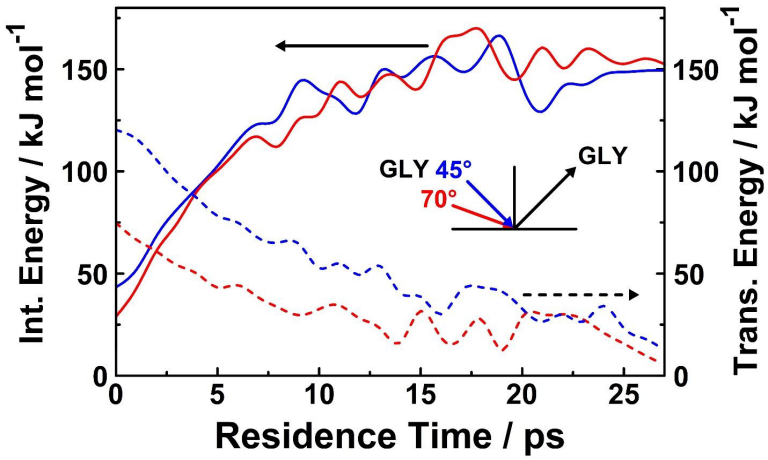

Figure S3. Average translation and internal energies of GLY molecules that scatter via the EIS mechanism as a function of the residence time, with θ_i = 45° (blue) and 70° (red).

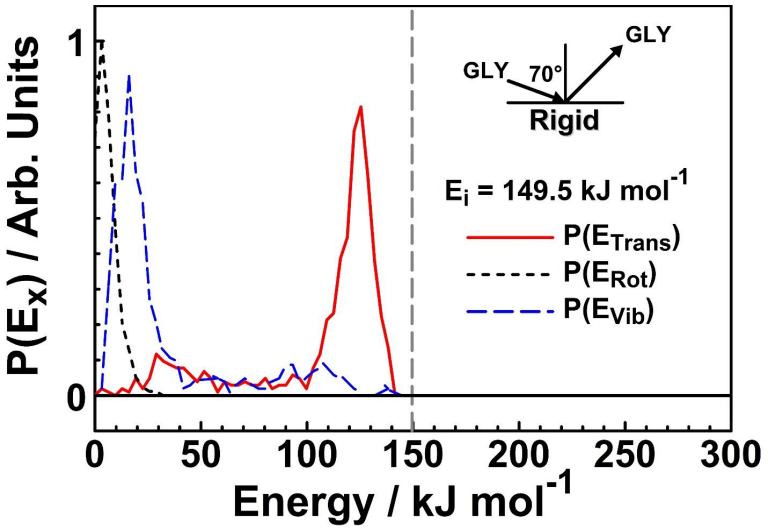

Figure S4. Simulated translational ($P(E_T)$, solid red line), rotational ($P(E_{Rot})$, dotted black line), and vibrational ($P(E_{vib})$, blue dashed line) distributions for GLY molecules that scatter from a rigid HOPG surface, with θ_i = 70°.

CHAPTER 4

INSIGHTS INTO ADSORPTION, DIFFUSION, AND REACTIONS OF ATOMIC NITROGEN ON A HIGHLY ORIENTED PYROLYTIC GRAPHITE SURFACE

The materials discussed in this chapter is based on the publication: Wang, Y.; Nieman, R.; Minton, T. K.; Guo, H. Insights into adsorption, diffusion, and reactions of atomic nitrogen on a highly oriented pyrolytic graphite surface. *J. Chem. Phys.* **2021**, *154*, 074708.

4.1 Introduction

When a returning spacecraft enters Earth's atmosphere, its hypersonic speed creates a hot shock layer above the leading surface of the vehicle, where rich chemistry takes place both in the gas phase and at the gas-surface interface. Atmospheric oxygen and nitrogen molecules are highly excited and many dissociate to produce atomic species.[142-143] The high temperatures of the shock layer lead to gas-surface collisions on the thermal protection system (TPS) surface of the vehicle at relative velocities that exceed 1 km s^{-1}, and the heat transported by the boundary layer gas to the TPS surface may result in surface temperatures that exceed 2000 K. Carbon and/or polymeric materials that form a carbon char are often used in for the TPS,[144-145] making the reactions of O and N atoms with hot carbon particularly relevant to hypersonic ablation during atmospheric entry. In order to optimize the design of a TPSs, much effort has been dedicated to the accurate and reliable modeling of carbon ablation.[146-148] The reliability of the models depends on the understanding of the microscopic mechanism and dynamics of the corresponding chemical processes. To gain insight into these issues, there have been several recent experimental and theoretical studies of collisions of the relevant gaseous species with carbon-based materials such

as highly oriented pyrolytic graphite (HOPG) and vitreous carbon.[149-159] Among these recent studies, most have focused on the scattering of O_2 and O from carbon surfaces.[149, 154-155, 158, 160-161]

In this work, we focus on the interaction of atomic nitrogen ($N(^4S)$) with pristine and defected graphite surfaces, which has received much less attention than analogous atomic-oxygen interactions. It is well known that N_2 does not easily react with carbon, but the reactivity of atomic nitrogen with graphite surfaces has been documented since 1964,[162-167] although earlier work offered few microscopic details on the process. More recently, molecular beam experiments have been performed to provide detailed information of $N(^4S)$ and N_2 scattering from both HOPG and vitreous carbon.[157-158] In addition to the expected direct scattering of atomic and molecular nitrogen, these experiments have identified interesting chemical processes, such as N-atom recombination to form N_2 and the reaction to produce CN. Furthermore, there is tantalizing evidence of atomic nitrogen trapping in the carbon surface at lower temperatures, which is released at higher surface temperatures.[158] While the adsorption and diffusion of atomic nitrogen on graphite or graphene surfaces have been extensively investigated previously,[168-169 170-176] such processes below the top graphene layer, as well as reactive processes involving atomic nitrogen have been largely unexplored from a theoretical perspective. We recently conducted an initial theoretical study on this topic,[159] using a direct dynamics method with a semi-empirical electronic structure theory (density functional tight bonding, or DFTB[177]). Related work on the controlled modification of graphene conducting properties by nitridation, aimed at modifying its electronic properties,[178] preceded our study.[179] While the use of DFTB provided a relatively low-cost approach to reveal various physical and chemical processes, DFTB theory is not quantitatively accurate. In addition, the model surface was approximated by a single molecule with edge atoms artificially anchored, which places a severe limit on the ability of the model to describe energy

transfer. Thus, we have increased the sophistication of our theoretical approach to the understanding of N-atom interactions on carbon by using a graphite slab model characterized with plane-wave density functional theory (DFT) with a non-local functional. We have explored both static and dynamic processes, and we have used the results to rationalize the observations in the recent molecular beam-surface scattering experiments on N-atom interactions with a vitreous carbon surface.[157-158]

4.2 Methods

While interaction potentials based on force fields have been used in many theoretical studies on the scattering of molecules from graphite surfaces,[180-183] such approaches are not expected to provide quantitative information on reactive events such as those investigated here. As mentioned above, numerically efficient semi-empirical Hamiltonians may also introduce large errors.[155, 159, 184] Hence, we employ here a first principles method based on plane-wave density functional theory to explore not only adsorption and diffusion, but also reactive events relevant to atomic-nitrogen scattering with graphite surfaces.

The (0001) facet of graphite was modeled by four-layer periodic slabs with a $p(5\times5)$ unit cell separated by a 20 Å vacuum space. In each slab, the adsorbate and the top three graphite layers were allowed to move, and the bottom graphite layer was frozen in a bulk-like geometry. The valence electron density was expanded in a plane-wave basis with a cutoff kinetic energy of 400 eV, and the electron-ion interaction was approximated using the projector augmented wave (PAW) scheme.[185] The integration of the Brillouin zone was performed using a 1×1×1 Monkhorst–Pack *k*-point mesh.[186] During optimization, the self-consistent field iteration was considered converged when the energy difference was less than 10^{-5} eV and the geometry optimization was considered converged when the force on each atom was less than 0.02 eV/Å. All DFT calculations were

carried out using the Vienna Ab-initio Simulation Package (VASP).[187-188] Spin polarization is taken into consideration in all calculations.

Given that graphene layers in graphite are bound through van der Waals (vdW) forces, it is essential to accurately describe the long-range interactions in order to obtain reasonable results. The most widely used electron exchange and correlation functionals in DFT calculations are based on the generalized gradient approximation (GGA).[189] However, a general drawback of the normal GGA functional is that it poorly describes the long-range electron correlations which are responsible for vdW forces. To overcome this limitation, a vdW density functional (vdW-DF) method can be used,[190] in which the exchange-correlation energy consists of two parts involving local and non-local correlations. In this work, the optB86b-vdW-DF[191] was used to include dispersion forces.

Static calculations were performed in order to determine adsorption energies and transition states. The adsorption energy of an adsorbate was calculated as

$$E_{\mathrm{ad}}\,(\mathrm{adsorbate}) = E_{\mathrm{adsorbate/graphite}} - E_{\mathrm{graphite}} - E_{\mathrm{adsorbate}}$$

where $E_{\mathrm{adsorbate/graphite}}$ is the total energy of the adsorbate adsorbed on graphite surface, E_{graphite} is the energy of clean graphite surface and $E_{\mathrm{adsorbate}}$ is the energy of the adsorbate in gas phase. To map out the transition states, the climbing image-nudged elastic band (CI-NEB)[192-193] and dimer[194] methods were used. The Hessian matrix of the stationary points was calculated numerically to obtain the harmonic vibrational frequencies of each vibration mode.

In addition to the static calculations described above, *ab initio* molecular dynamics (AIMD) were used to investigate the dynamics of N_2 formation through both Langmuir-Hinshelwood (LH) and Eley-Rideal (ER) mechanisms. The trajectories were propagated with a time step of 0.5 fs using the forces calculated on the fly. For the LH pathway (N* + N* → N_2(g)), AIMD trajectories

were started from the recombinative desorption transition state to shed light on the product energy disposal. In such calculations, the initial velocity for each atom was sampled from a Boltzmann distribution at the simulation temperature. For the ER pathway (N(g) + N* → N_2(g)), the impinging N atom was prepared at Z = 4.0 Å above the surface, with a direction towards the surface having an incident angle of θ_i = 60° relative to the surface normal and an incident kinetic energy of E_i = 0.3 eV, as in the recent experiment.[158] In both cases, the simulation was terminated when the distance between the newly formed N_2 and graphite surface was over 7.0 Å, or when the molecule became stuck on the surface for more than 1.5 ps. Two experimental temperatures, 1000 and 1900 K, were selected to examine the temperature effect on N-N recombination on the graphite surface, but ER simulations were only conducted at 1900 K. For the desorbed N_2, the final kinetic energy, scattering angular, and ro-vibrational energies were extracted from the trajectories. Using histogram binning, the rotational quantum number was determined by the angular momentum, while the vibrational quantum number was determined by the total energy in the vibrational coordinate.

Finally, to rationalize the AIMD results for the LH pathway, the sudden vector projection (SVP) model, which is a transition-state based model for predicting energy disposal, was used. The principle behind this model is that, in the sudden limit, the energy disposal in a product degree of freedom is proportional to the overlap of the corresponding normal mode with the reaction coordinate at the transition state.[195] The applicability of the SVP model in surface processes has been demonstrated in many reactive systems.[196-197]

4.3 Results

First, we assessed the validity of the DFT model in charactering the bare graphite surface. With the vdW-DF, the geometry of the relaxed graphite is in excellent agreement with experiment:

C-C bond length is 1.42 Å, same as experimental measurement, and the interlayer separation is 3.35 Å, with a percent deviation of 1.49 % from actual value.[198]

The non-polar nitrogen molecule is expected to physisorb on graphite surfaces, which was confirmed in our calculation. With the vdW-DF, which is a non-local correlation functional that accounts for dispersion interactions, the calculated adsorption energy of N_2 on graphite with a parallel or perpendicular configuration was –0.28 or –0.24 eV, respectively. In these two minima, the center of mass of N_2 is 3.27 and 4.06 Å away from the surface, which is not distorted. An image of the most stable adsorption geometry for N_2 adsorbed in the parallel configuration may be seen in Figure 1. There have been several experimental reports on the N_2-graphite/graphene adsorption energy, with values of –0.10,[199] –0.16,[200] and -0.27 to –0.37 eV.[201] The latter result was measured at a low coverage and is thus perhaps more relevant to our model at the near zero-coverage limit. Our calculated adsorption energies are larger in magnitude than those of most previous theoretical calculations,[168, 170, 172] presumably due to the different models used to simulate graphite/graphene.

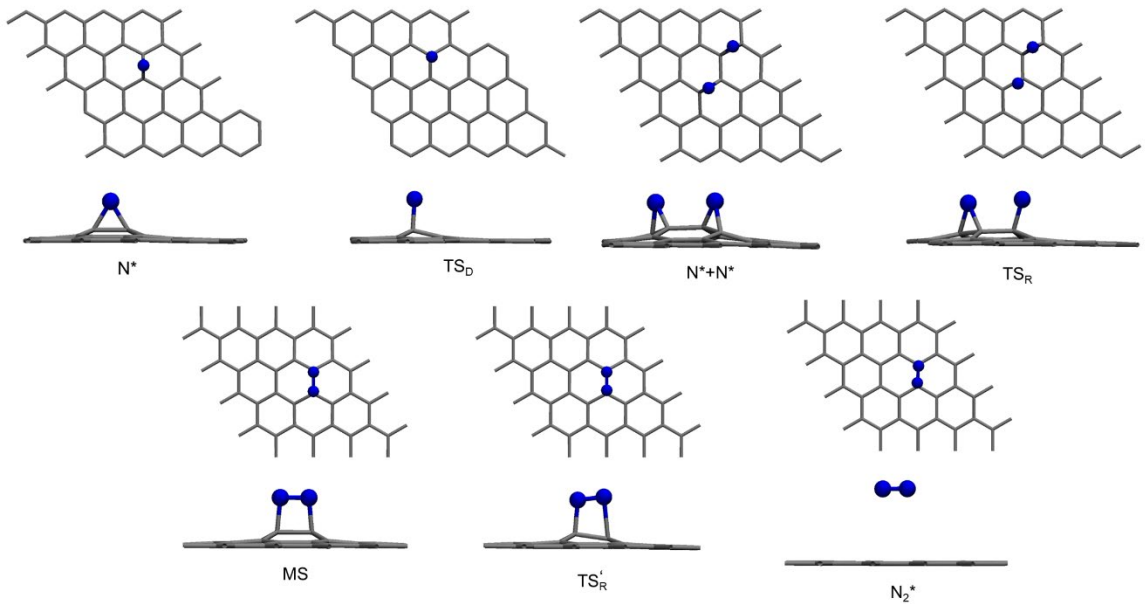

Figure 1. Top and side views of geometries of the stationary points for N* adsorption, diffusion, and reactions on the graphite surface. Only the top layer of the graphite is shown for clarity.

There are three high symmetry sites available for N-atom adsorption on the graphite surface, which are top, bridge, and hollow sites. From our calculations, the adsorption site of the N atom is the bridge site, as shown in Figure 1. It is clear from the figure that the two carbon atoms of the top graphene layer pucker above the surface plane, indicating some sp^3 character. The corresponding N-C bond lengths are 1.47 and 1.48 Å, respectively, while the C-C bond is 1.53 Å, slightly elongated from that in graphene (1.42 Å). The adsorption at top and hollow sites was examined and found to be unstable. This adsorption geometry is supported by previous theoretical studies on N chemisorption on a graphene or graphite surface.[169, 171, 173-176] The Bader charge of the adsorbed nitrogen is 0.51 *e*, signaling significant charge transfer from the underlying graphene. The adsorption energy at the bridge site is calculated to be –1.10 eV, relative to the gas phase N(^{4}S), as shown in Table 1. This value is larger than those reported in previous theoretical studies, ranging from –0.78 to –0.93 eV,[169, 175-176] presumably due to the inclusion of the vdW interactions in our calculations.

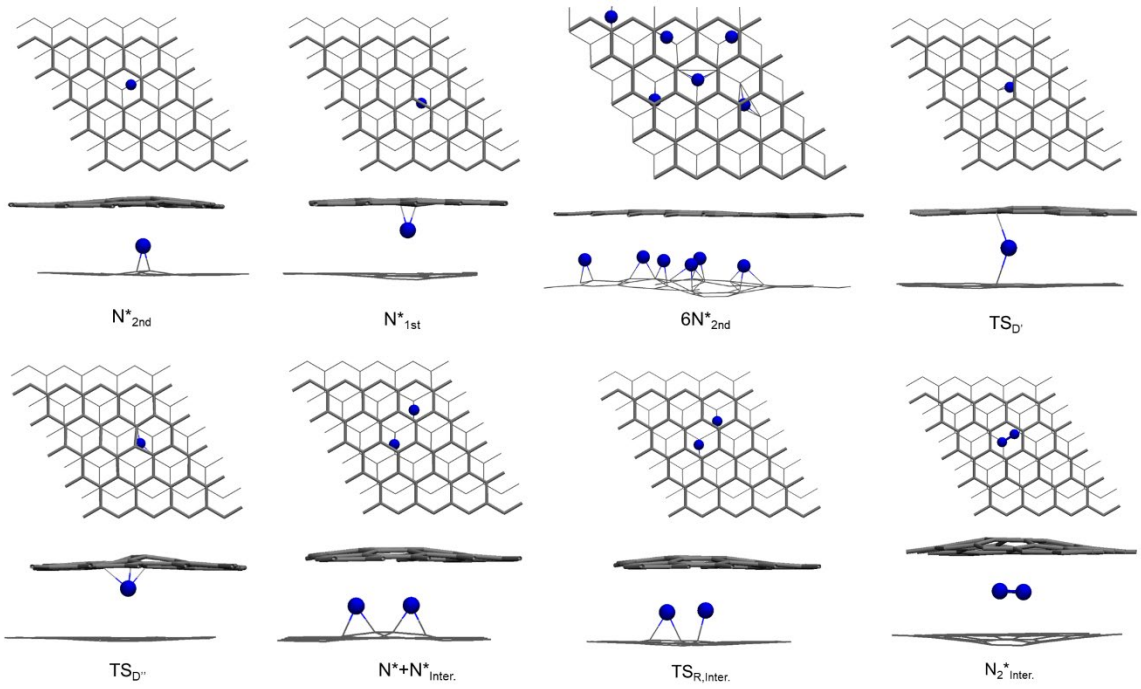

Figure 2. Top and side views of geometries of the stationary points for N* adsorption and diffusion between the first and second graphite layers, which are represented by thick and thin lines, respectively.

To understand possible trapping of atomic nitrogen underneath the top layer of graphite, the adsorption of atomic nitrogen between the first and second layers of graphene sheets was investigated. While the adsorption geometries for interlayer N are similar to those on the top surface, as shown in Figure 2 (N^*_{1st} and N^*_{2nd}), the adsorption energies are significantly smaller (–0.12 and –0.19 eV, respectively). The reduction of the adsorption energy can be traced to the mechanical (vdW) energy cost of distorting the graphene layers,[202] which is clearly visible in Figure 2. The distortion of the graphene sheets is not restricted to the adsorption site, because of their planar rigidity. As a result, the adsorption energy is expected to increase when multiple N atoms are adsorbed between the sheets. Indeed, when six N atoms are adsorbed, as shown in Figure 2, the average adsorption energy becomes –1.02 eV, only slightly smaller than the adsorption energy of an N atom on the top surface. The adsorption energies are listed in Table 1.

We have also investigated the adsorption of atomic nitrogen at defect sites on the graphite surface. Specifically, single carbon vacancy (SV) defects, in which a single carbon on the top layer of graphite is removed, are considered. As expected, the binding energy at the defects is much larger than that on a pristine surface, as the carbon atoms at the defects are unsaturated and highly reactive. The N* atom can replace the missing carbon atom and form a planar and three-coordinated structure, as shown in Figure 3. This nitrogen species, denoted as N^*_{SV}, has a large adsorption energy (–11.9 eV). The adsorption of an N atom at a bridge site near the SV defect, denoted as $N^*_{SV\text{-}B}$ in Figure 3, has an adsorption energy slightly larger than that on the pristine surface (–1.39 eV). We also found a Stone-Wales (SW) defect formed by adsorbed nitrogen, denoted in Figure 3 as N^*_{SW}. The N atom is again three-coordinated, and the adsorption energy (–7.26 eV) is somewhat smaller than for N^*_{SV}. Again, the adsorption energies are listed in Table 1.

Addition of a second N* atom to bridge sites around the defect in N^*_{SV} gives two structures, $2N^*_{SV1}$ and $2N^*_{SV2}$ as shown in Figure 3, each with similar adsorption energies relative to free N of –2.05 and –1.99 eV, respectively. Finally, a second N* atom will form C-N and N-N bonds when added to the defect in N^*_{SV} gives $2N^*_{SV3}$, also shown in Figure 3, where the adsorption energy decreases in magnitude to –1.32 eV. These adsorption energies are listed in Table 1.

Table 1. Adsorption energies (eV) for N atom on both pristine and defect graphite, referenced to a $N(^4S)$ atom in the gas phase.

Top layer of graphite						
N^*	N^*_{SV}	$N^*_{SV\text{-}B}$	N^*_{SW}	$2N^*_{SV1}$[a]	$2N^*_{SV2}$[a]	$2N^*_{SV3}$[a]
-1.10	-11.9	-1.39	-7.26	-2.04	-1.99	-1.32
Between the two top layers of graphite						
N^*_{1st}	N^*_{2nd}	$6N^*_{2nd}$[b]				
-0.12	-0.18	-1.02				

a: for the N adsorbate on the N-substituted graphite layer.
b: averaged value per N atoms.

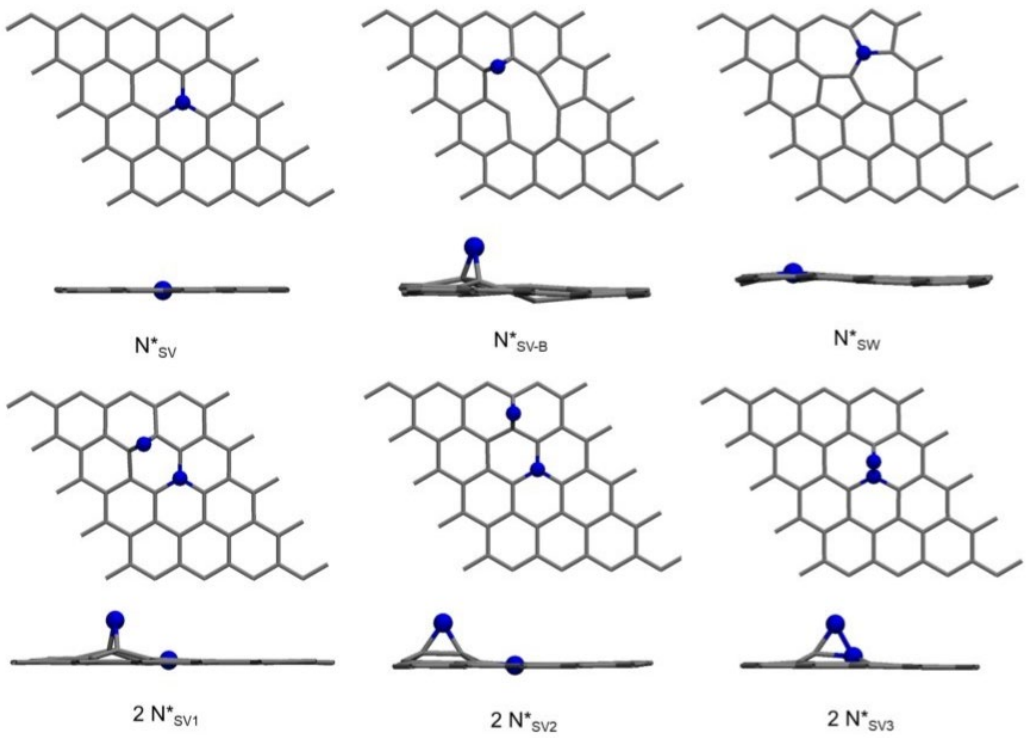

Figure 3. Top and side views of geometries for stationary points of one and two N* adsorbed to the single vacancy (SV) graphite defect site.

The diffusion of N* from one bridge site to a neighboring bridge site on the (0001) surface of graphite was investigated. The diffusion barrier was calculated to be 0.88 eV, as shown in Figure 3 and listed in Table 2. The diffusion transition state (TS_D) features the N atom at the top of the C atom shared by the two bridge sites, with an N-C distance of 1.47 Å, as shown in Figure 1. Previous theoretical studies on N-adatom diffusion on graphene/graphite suggest an activation energy of 1.1[169] and 1.0 eV.[174] The difference can presumably be attributed to the different exchange-correlation functionals and different sizes of supercell used in the calculations. Such a barrier implies that the mobility of adsorbed atomic nitrogen is *limited* at room temperature but elevated at higher temperatures, above 1000 K.

The diffusion barriers for N* trapped between the two top graphene sheets have also been determined. The barrier for diffusion between two bridge sites on the same sheet is 0.57 eV,

smaller than that for diffusion on the top surface, while the diffusion barrier for N hoping between the adsorption sites on different sheets is 1.28 eV. The geometries of the transition states are shown in Figure 2 and the barriers are listed in Table 2.

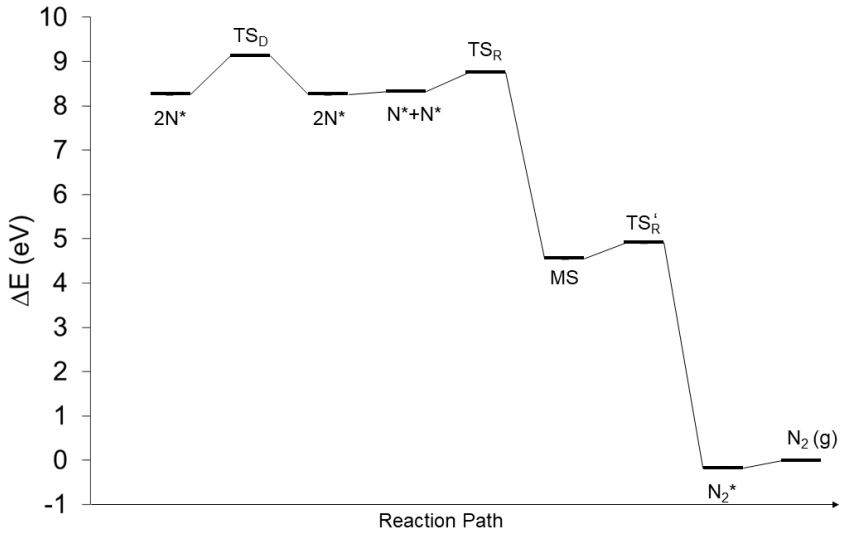

Figure 4. Energy diagram for the diffusion of N* and recombinative desorption of N_2 on the (0001) facet of graphene. 2N* denotes the adsorption state of two infinitely separated nitrogen atoms, while N* + N* is the initial state for TSR. N_2* denotes the physisorbed state of the molecule, while MS the metastable N_2 on the graphite surface. Geometries of the stationary points are given in Figure 1.

N-N recombination on graphite may proceed through either a Langmuir–Hinshelwood (LH) or an Eley-Rideal (ER) mechanism, and both mechanisms were studied here. For the LH mechanism, two infinitely separated N adsorbates at the graphite surface diffuse towards each other and overcome a barrier for recombinative desorption to form N_2. This reactive transition state was determined to be 0.53 eV above the initial state (IS), shown in Figure 4 as TS_R and N* + N*, respectively. Given that the energy of the IS is -0.06 eV above the infinitely separated limit (denoted in Figure 3 as 2N*), the overall barrier is 0.47 eV, as listed in Table 2. This barrier is lower than that determined by Ma et al., which is 0.80 eV.[169] As shown in Figure 1, at the transition state, one N atom largely stays in the initial bridge site, and the other N atom moves to an adjacent

top site from the original bridge site. The distance between two N atoms is 2.54 Å and their distances to the underlying carbon atoms are 1.46 and 1.48/1.54 Å (N atom at top and bridge sites, respectively). The final state (FS) is the physisorbed N_2 (denoted as N_2* in Figure 3) which is 8.98 eV lower than the TS_R and 0.28 eV below the energy of the free N_2.

Further analysis indicated that there is a metastable state between the TS_R and physisorbed N_2. This species is 4.22 eV lower than TS_R, as shown in Figure 4. Its geometry has a much-elongated N-N distance (1.27 Å) and shorter C-N distances (1.53 and 1.54 Å) than N_2*, which suggests chemisorption. Indeed, it has a negative ion character, as the Bader charge of the N_2 moiety is –0.65 e, reminiscent of the metastable $CO_2^{\delta-}$ anion on Pt surfaces.[203] The transferred fractional electron is expected to partially occupy an antibonding orbital of N_2, leading to its elongated bond length. The existence of this metastable state is responsible for the trapping of the incipient N_2, as shown in the AIMD results discussed below. The corresponding transition state (TS_R') is identified with a barrier of 0.18 eV, as shown in Table 2.

The recombinative reaction between two adsorbed N* atoms leading to physisorbed N_2 via the LH mechanism was investigated between the two top sheets as well. The TS structure ($TS_{R,Inter}$, Figure 2) is 0.49 eV above the IS, denoted as N*+N*$_{Inter}$. The full barrier height is 1.06 eV, coming from two infinitely separated adsorbed N* atoms, about twice the value found for the top surface. The IS is located 0.57 eV above the infinitely separated limit, much higher than the -0.06 eV for the top layer. The $TS_{R,Inter}$ geometry is quite similar to the TS_R structure for the top surface with one N atom at a bridge site and the second bonded to only one carbon, while the two N atoms are closer together at 2.19 Å. The FS (physisorbed N_2, denoted N_2*$_{Inter}$) is 7.35 eV below $TS_{R,Inter}$, 2.69 eV above the energy of free N_2. These barriers are listed in Table 2.

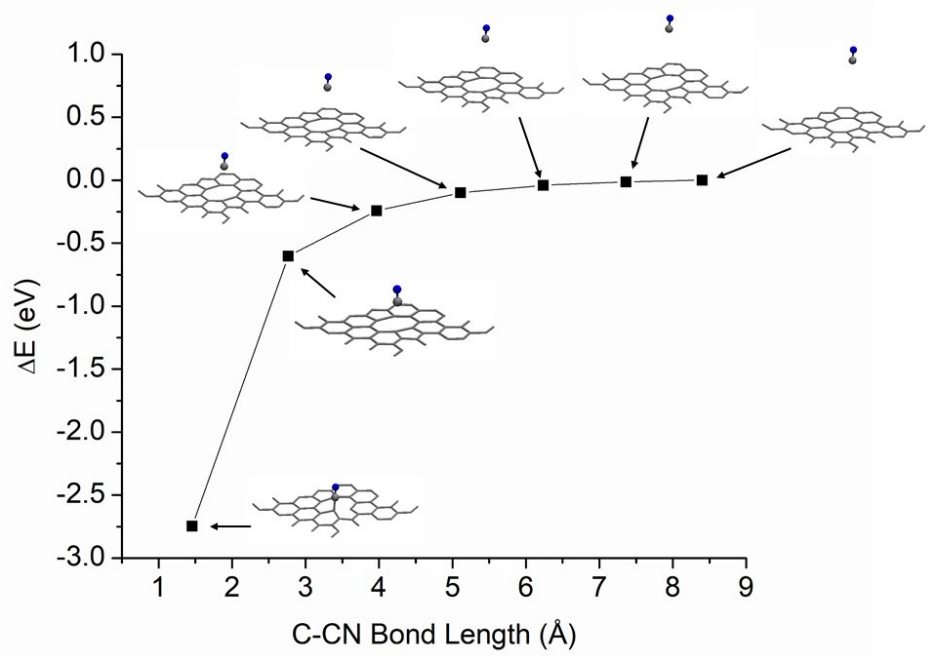

Figure 5. Potential energy curve for the NEB calculation of CN dissociating from the graphene defect surface. Corresponding geometries are shown for each point.

No transition state was located for the ER pathway, in which the approach of a gas phase N(^{4}S) atom is barrierless and highly exoergic with an energy release of 9.68 eV. The calculated exoergicity is consistent with the experimental value of 9.75 eV.[157]

We have also examined the formation of CN from defected graphene in which a nitrogen atom is connected to an edge carbon atom, as shown in Figure 5. No barrier was found for the breaking of the C-N bond between the CN moiety and the substrate, and the energy required to release the CN radical is 2.75 eV. The energetics of the NEB images and the corresponding geometries are shown in Figure 5. As the CN group departs from the surface, its bond length extends slightly from 1.17 Å to the final value of 1.18 Å.

The AIMD calculations for the LH path were performed by starting the trajectories at the TS_R geometry and sampling the vibrational normal modes orthogonal to the reaction coordinate with the Boltzmann distribution, as described in our recent work.[203] 50 trajectories towards the

product were run at each temperature (1000 or 1900 K). At the higher temperature (1900 K), all but one trajectory resulted in the formation of gaseous N_2 product. However, only 44 trajectories at the lower temperature (1000 K) did the same and the rest were trapped on the surface at the end of the 1.5 ps simulation time. No trapping in the physisorption well was observed, resulting apparently from its small adsorption energy. The translational, rotational, and vibrational distributions of the desorbed N_2 are shown in Figure 6, and scatter plots of angle and kinetic energy for all the trajectories are displayed in Figure 7. It is clear that the desorbed N_2 molecules are translationally and vibrationally hot, while rotational excitation is limited. The average translational and vibrational energies are 2.25 (2.39) and 1.37 (1.67) eV, respectively, at 1000 (1900) K. These molecules are ejected mostly along the surface normal.

Table 2. Barrier energies (eV) for N atom and N_2 molecule with both pristine and defect graphite slabs. The process resulting in the TS is defined below the TS label.

Top layer of pristine graphite		
TS_D	TS_R	$TS_{R'}$
$N^* \rightarrow N^*$	$N^* + N^* \rightarrow N_2^*$	$MS \rightarrow N_2^*$
0.88	0.53	0.18
Intercalation of pristine graphite		
$TS_{D'}$	$TS_{D''}$	
$N^*_{1st} \rightarrow N^*_{2nd}$	$N^*_{1st} \rightarrow N^*_{1st}$	
1.28	0.57	

To understand the vibrational excitation of the N_2 product, we resort to the SVP analysis. The projection of the N-N vibrational mode onto the reaction coordinate at TS_R is 0.40, while the that for the translational mode along the surface normal (Z) is 0.07. This is due to the fact that the corresponding reaction coordinate is mostly along the N-N vibrational coordinate as the N_2 molecule is formed. These SVP values predict that the energy disposal of this highly exoergic process goes largely into the vibrational degree of freedom, consistent with the high vibrational excitation in the N_2 product. On the other hand, the projection of the translational mode along the

surface normal is 0.90 at TS_R', suggesting strong repulsion when the chemisorbed N_2 is converted to physisorption. As a result, the N_2 product is expected to gain a large amount of kinetic energy along this direction as it departs from the transition state.

The SVP values also explain the trapping of the trajectories at the low temperature. As a large portion of the energy released from TS_R is in the vibrational coordinate, the energy in the translational coordinate is expected to be small as it departs from the barrier. This is similar to the post-transition state dynamics in the recombinative chemisorption of CO_2 on Pt surfaces.[203] Indeed, they are likely to enter the chemisorption well at MS because of the large N-N internuclear distance resulting from vibrational excitation. While the N_2 is expected to desorb eventually to the gas phase, our maximal simulation time of 1.5 ps is not sufficient to observe its eventual fate.

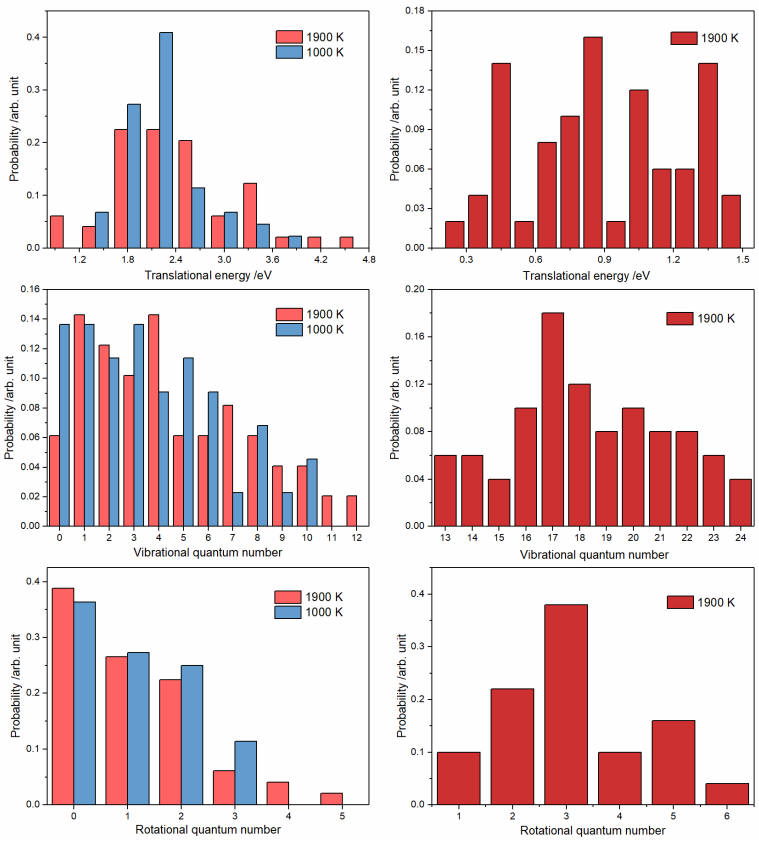

Figure 6. Translational energies and vibrational and rotational state distributions for N_2 products from the LH (left panels) and ER (right panels) pathways.

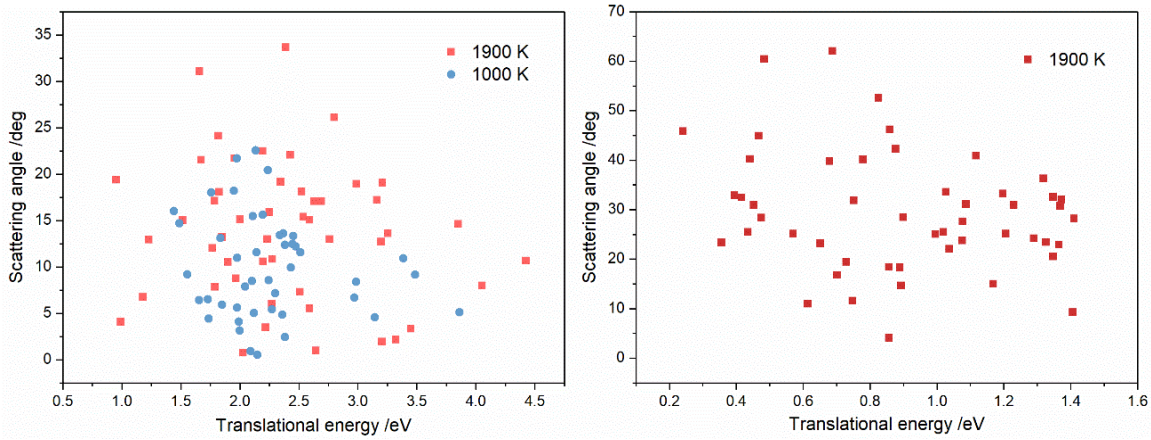

Figure 7. scatter plots of the N_2 angle and translational energy for the LH (left) and ER (right) pathways.

Finally, AIMD trajectories have been calculated for the ER pathway. The initial conditions feature an N atom adsorbed at bridge site and the gaseous N atom 4.00 Å above the surface with a random x and y coordinates in the unit cell and a polar angle of 60° from the surface normal. The initial kinetic energy was 0.30 eV, and the graphite surface was simulated at 1900 K. Many trajectories led to direct scattering of the impinging N because of the large impact parameter with the adsorbed N, and these trajectories were ignored. The N_2 product distributions for 50 reactive trajectories with small impact parameters are given in Figures 6 and 7. It is clear that the ER pathway results in lower translational energy but higher vibrational excitation than the LH pathway. Note also that the angular distribution of the products is peaked significantly away from the surface normal, suggesting that the product retains some memory of the incident angle and energy. These are typical characteristics of ER reactions.[204-209]

The exothermicity during N-N recombination can impact the heat flux to a TPS surface; therefore, the energy that was transferred to the graphite surface during N-N recombination was calculated and the results for the two different mechanisms were compared. From Figure 8, it is clear that the majority of the energy released from N-N recombination through the ER pathway

goes to the nascent N_2 molecule, especially into vibrational and rotational modes. On the other hand, a much larger amount of energy is transferred to the surface in the LH pathway. While similar trends were observed at both 1000 and 1900 K, more energy is transferred to lattice motion at 1000 K. This is understandable because the residence time of newly formed N_2 on graphite is longer at 1000 K than at 1900 K, which gives more time for the energy transfer process and explains the larger fraction of trapped molecules at 1000 K.

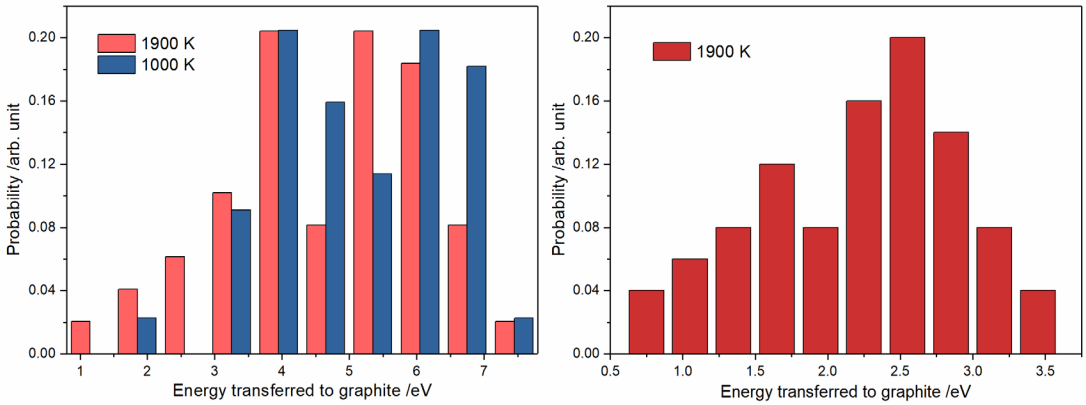

Figure 8. Distributions of energy transferred to the graphite surface in N-N recombination through LH (left) and ER (right) pathways.

4.4 Discussion

The theoretical results on the adsorption, diffusion, and reactions of atomic nitrogen on a graphite surface offer insights into observations in the recent molecular beam experiments.[157-158] Apart from non-reactive scattering, these experiments established that nitrogen atoms recombine to form N_2 molecules, which are then emitted into the gas phase. The formation rate of N_2 was observed to increase with temperature, implying an activated process. Our calculations confirm the existence of barriers for the N_2 formation via the LH mechanism and suggest that the rate-limiting step is the diffusion of N atoms adsorbed at the bridge sites of the graphite surface. The calculated diffusion barrier of 0.88 eV is significant, but at the experimental temperature of ~2000 K, the Boltzmann factor is non-negligible (~1%). This is presumably why our previous direct

dynamics study found no recombinative desorption, as the relatively short simulation time did not allow the diffusion of N atoms.[159] Once the N adsorbates encounter each other, the recombinative desorption can take place with a barrier that is lower than that for diffusion. Unfortunately, there is no experimental report on the apparent activation energy for the N_2 formation on graphite. In addition, our calculations also indicate a non-thermal ER pathway, which is barrierless. This ER mechanism could become important at high coverages of adsorbed N atoms as the chances for N(g) + N* encounters increase with the coverage. The competition between the ER and LH pathways at higher coverages is a future research topic, as the barrier for the LH pathway is likely to decrease with the N coverage. Our AIMD calculations indicate that the desorbed N_2 products formed through both the LH and ER pathways are vibrationally highly excited. This internal excitation in the ER mechanism is a manifestation of the abstraction nature of the reaction. For the LH mechanism, vibrational excitation can be explained by the SVP model, which suggests that a large overlap between the reaction coordinate at the transition state and the N-N vibrational mode facilitates facile energy flow from the former to the latter. Our results further predict trapping of the incipient anionic N_2 in a metastable well at low temperatures. These predictions are to be verified by future experiments.

Apart from the formation of N_2, the recent experiment of Murray et al. also found significant CN product.[157-158] This radical has long been speculated as the nascent product in atomic nitrogen ablation of graphite, because the C_2N_2 species was observed in earlier experiments.[162-163, 165] In sharp contrast to N_2, which is likely a physisorbed species on graphite, the CN radical is chemisorbed. The activation energy for the CN formation was estimated by Murray et al. to be 1.78 eV.[158] This product has also been found in our previous simulation as a minor species when the incident energy was 4.77 eV.[159] DFT calculations reported here indicate

that the elimination of the CN radical from a defected graphite surface is endoergic by 2.75 eV, but with no barrier. This activation energy is significantly larger than those reported experimentally. There might be a number of factors that can contribute to this experiment-theory discrepancy in the binding energy of CN on graphite. Apart from the uncertainty associated with the functional in DFT, the binding energy might be significantly affected by the bonding site, bonding pattern, nature of the defect site, and the presence of nearby adsorbates. These questions require more detailed investigations in the future. However, it is clear that the formation of CN requires more activation energy than the recombinative desorption of N_2. This difference explains the order of magnitude smaller CN signal.[158]

The experiment at low collision energy (0.36 eV) found that the N, N_2 and CN products can all be characterized by near cos□ angular distributions and Maxwell-Boltzmann kinetic energy distributions at the surface temperature.[158] Although these results are signatures of a thermal desorption process, one needs to consider the fact that vitreous carbon was used as a substrate in these experiments. Due to the extreme roughness of these surfaces, it would not be unreasonable to assume that desorbing atoms and molecules undergo multiple collisions with on the surface before escaping to the gas phase. These collisions are expected to dissipate the extra energy to the substrate, resulting in a thermal distribution, as suggested in our earlier work.[159] Interestingly, at high collision energy (4.8 eV), neither N_2 nor CN was found experimentally to have a Maxwell-Boltzmann distribution.[157] Our theoretical results reported here suggest that although N* may be equilibrated with the graphite surface, the N_2 product is unlikely to be thermally equilibrated. For the ER pathway, the direct abstraction nature prevented such a statistical outcome, while for the LH pathway the existence of a significant barrier and large exoergicity also result in hyperthermal

translational and internal excitations in the product. To provide a definitive comparison with theory, experiments need be performed on well-defined graphite surfaces such as HOPG.

There is some evidence from the recent experiments that the total nitrogen flux increases with surface temperature, seemingly violating mass balance.[158] This observation could be a manifestation of N atoms that are trapped in the bulk more efficiently at lower temperatures than at higher temperatures. Our theoretical results suggest that it is possible for atomic nitrogen to intercalate the graphene sheets with average adsorption energies comparable to those on the top surface. These inter-sheet nitrogen atoms might be responsible for the experimental observations of additional nitrogen release at high temperatures.

4.5 Summary and Conclusions

We report in this work an extensive density functional theory study of the interaction of atomic nitrogen with pristine and defected graphite surfaces. The adsorption and diffusion of atomic nitrogen are investigated on the (0001) face of graphite, in between graphene sheets, and at defect sites. In addition, the formation of N_2 via LH and ER mechanisms and the formation of CN are investigated. While the ER reaction to form N_2 requires no barrier, the LH pathway is limited by the diffusion barrier of the N-atom adsorbate. The N_2 formation is found to be highly exoergic, but the CN formation is highly endoergic. Furthermore, the N_2 product is found to be translationally and internally hot. These theoretical results are used to shed light on the recent experimental observations. Although quantitative agreement is still to be achieved, qualitative understanding of the possible reaction pathways and mechanisms improve our understanding of the experimental data. More complete knowledge of such processes will require detailed and better-defined experiments and more realistic simulations of scattering dynamics. The advances will benefit models of hypersonic air-carbon ablation chemistry and future design of TPS materials.

CHAPTER 5

SPIN-DEPENDENT REACTIVITY AND SPIN-FLIPPING DYNAMICS IN O ATOM SCATTERING FROM GRAPHITE

The materials discussed in this chapter is based on the publication: Z. Zhao, Y. Wang, X. Yang, J. Quan, B. C. Krüger, P. Stoicescu, R. Nieman, D. J. Auerbach, A. M. Wodtke, H. Guo, G. B. Park, Nat. Chem., submitted, Spin-dependent reactivity and spin-flipping dynamics in O atom scattering from graphite.

5.1 Introduction

The influence of electronic spin on the outcome of molecular collisions is of fundamental importance in understanding chemical reaction pathways and rates and often has dramatic effects. In gas-phase reactions and photochemistry, electronic spin conservation leads to well-known selection rules. For example, $O(^1D)$ reacts without a barrier by inserting from the side into an H-H bond to form water[210], whereas $O(^3P)$ reacts at one end of the molecule forming OH+H, which requires significant activation[211]. On the other hand, spin-forbidden reactions are known, particularly for systems involving heavy atoms.[212] Spin-orbit couplings can be computed for simple gas-phase reactions[213], and the role of spin in gas-phase reaction dynamics has become well understood.

In contrast, for surface reactions, so important to topics like catalysis, corrosion, and microelectronic materials processing, spin-selective reactivity is controversial. For example, spin selection rules have been invoked to explain conflicting results coming from experiment and theory for the dissociative chemisorption of $O_2(^3\Sigma_g^-)$ on Al(111). Experiment shows that the

reaction becomes more probable when $O_2(^3\Sigma_g^-)$ collides at the surface with high translational energy[57], a clear indication of a barrier to dissociative adsorption. However, when DFT calculations are performed at the level of generalized gradient approximation (GGA), no barrier is found.[59, 214] One school of thought supposes that the reaction must occur with conservation of triplet spin, and indeed spin restricted DFT calculations predict a barrier to reaction.[59, 214] An alternative explanation involves charge transfer—transient O_2^- formation— where barriers are found only when correlated wave function methods are used. In this line of reasoning, weaknesses in the ability of DFT-GGA to describe charge transfer are the source of inconsistency between experiment and theory[61, 66].

While the work just described reveals important features of surface chemistry, especially the care that must be taken when attempting electronic structure calculations of reaction paths, they leave unanswered questions of whether and under what conditions electronic spin is important in surface chemistry and it is unlikely to be unimportant. For example, it has been recently demonstrated that the electrons' spin degeneracy lowers the reaction rate constant fourfold in H-H recombination on metals, just as has long since been known for H-H recombination in the gas phase. The fate of atomic spin polarization in H scattering from surfaces has been explored theoretically[215], but to the best of our knowledge, there are no experiments addressing spin-dependent reactivity and/or spin-flipping pathways.

In this paper, we report spin-resolved state-to-state scattering of O atoms from a highly oriented pyrolytic graphite (HOPG) surface, using a novel ion-imaging technique to measure reaction probabilities and differential scattering cross sections with high velocity resolution for both incident and scattered atoms even when the incident atomic beam has a broad velocity distribution. We analyze these experimental observations with the help of novel spin-state selective

molecular dynamics (MD) simulations using newly developed high-dimensional potential energy surfaces (PESs), machine learned from DFT data. The results clearly demonstrate O(^{1}D) undergoes much more efficient reaction with HOPG than does O(^{3}P), exhibiting higher sticking probabilities than its high-spin counterpart. We also observe electronically nonadiabatic pathways, where O(^{1}D) quenches to O(^{3}P), releasing excess kinetic energy. The mechanism of quenching involves a spin flip – singlet to triplet – of a highly vibrationally excited chemisorbed O atom formed from incident O(^{1}D), that takes place before it has equilibrated fully with the surface.

5.2 Methods

The experimental setup is shown in Fig. S1 of the Supplementary Materials (SM). Alternately, one of two methods is used to generate atomic oxygen beams with different initial O-atom spin state distributions: photolysis, which favors formation of O(^{1}D), or electric discharge, which favors O(^{3}P).

O-atom photolysis source: To generate well-defined O atom beams comprising predominately O(^{1}D), we used 157 nm radiation from an F_2 excimer laser for photolysis of CO_2. The 157 nm photolysis of CO_2 occurs via two channels[216]

$$CO_2(^1\Sigma_g^+) + h\nu \rightarrow O(^1D) + CO(^1\Sigma^+) \quad \text{(Channel I, 94\%)}$$

$$CO_2(^1\Sigma_g^+) + h\nu \rightarrow O(^3P) + CO(^1\Sigma^+) \quad \text{(Channel II, 6\%)}$$

The measured translational energy distribution of the O(^{1}D) component is bimodal with broad peaks at 0.065 and 0.23 eV, whereas the minor O(^{3}P) component exhibits a single peak at ~1.5 eV.

O-atom discharge source: The discharge source makes use of a home-built pulsed solenoid valve equipped with a homemade pulsed DC discharge device[217] based on the Lu et al. design[218]. We measured the beam state composition to be 87±2% O(^{3}P) and 13±2% O(^{1}D). Both spin states

exhibit broad translational energy distributions peaked at 0.36 eV with a FWHM of 0.2 eV (See Section 1.1 of the SM for more details.)

Scattering experiments: Scattering experiments were performed from a pristine HOPG surface, held at 298 K and mounted downstream of the beam sources in a UHV chamber. The incident and scattered O atoms were detected state-selectively by resonance-enhanced multiphoton ionization (REMPI), using a pulsed, tunable UV dye laser. Ions were detected mass-selectively using a home-built imaging detector, which directly provides the velocity vector of each O atom that undergoes in-plane scattering, following the approach of Refs.[25, 219-221]. (See Section 1.1 of the SM for more details.)

Incoming/Outgoing Correlation Ion-imaging: high resolution scattering with "bad beams". The molecular beam sources of spin-state enriched O atoms used in this work exhibit broad and irregular velocity distributions, a common problem in molecular beam chemistry that typically prevents high resolution transitional energy measurements. We have overcome this problem by combining pulsed molecular and laser beams with ion imaging. Controlling the delay time between the pulsed laser and pulsed molecular beam acts as a time-of-flight velocity selection of the incoming atoms. Simultaneously, velocity information on the scattered outgoing atoms is obtained from ion imaging. Combining this incoming/outgoing velocity information allows us to determine the incident velocity of the O atom connected with individual scattered atoms detected in the ion image. Specifically, for every ion detection event seen in the ion image, we simultaneously record the time, t_{probe}, at which the REMPI laser fired relative to the firing of the atomic beam source. The position in the ion image tells us the velocity vector of the outgoing O atom v_{f} and, together with the distance from the REMPI detection point to the surface, $d_{\mathrm{REMPI-surface}}$, we can calculate the time at which the detected O atom departed the graphite surface,

$$t_{\text{depart}} = t_{\text{probe}} - d_{\text{REMPI-surface}}/v_{z,\text{f}} \qquad (1)$$

where $v_{z,\text{f}}$ is the component of v_{f} along the incident atomic beam axis. Assuming zero residence time, the arrival time of the atom at the surface is $t_{\text{arrive}} = t_{\text{depart}}$. With the measured distance from the beam source to the surface, $d_{\text{REMPI-surface}}$, we obtain the incident atom's speed

$$v_{\text{i}} = d_{\text{source-surface}}/t_{\text{arrive}} \qquad (2)$$

In this way, we determine the incident O-atom speed for each scattered atom seen in the ion image. By recording ion images at all values of t_{probe} where ions can be detected in the image, we map out distributions of v_{f} at particular values of v_{i} within the broad distribution of the incident beam. This multiplexing concept allows us to use "bad" O atom sources with broad speed distributions, but well-defined spin ratios to control incidence electronic excitation. (See Section 1.2 of the SM for more details.)

Density Functional Theory (DFT): DFT calculations of atomic oxygen on graphene were performed using the Vienna Ab initio Simulation Package (VASP).[93-94] The PBE functional was used to calculate the exchange-correlation energy.[222] The HOPG surface was approximated by a single graphene layer with a unit cell of 32 carbon atoms, which should be sufficient for low energy collisions. Unlike the conventional spin-relaxed treatment where the lowest energy spin state is followed, we constrained the spin of the system by fixing the number of unpaired electrons. These spin-constrained DFT data permit for the first time, the construction of spin-specific potential energy surfaces (PESs) for surface systems. These PESs with 99 dimensions were fit using the Embedded Atom Neural Network (EANN) method.[86] The triplet and singlet PESs were then used to reconstruct the adiabatic PES by taking the lower energy of the two PESs. These PESs were used as the basis for spin-conserving and spin-changing molecular dynamics (MD) simulations of atomic scattering. See Section 1.3 of the SM for more details.

5.3 Results

Calculated PESs. The calculated surface binding configurations and saddle points on the triplet and singlet PESs are compared in Fig. 1. The triplet PES has a shallow physisorption well ~2.3 Å above graphene and exhibits stable chemisorption at top and bridge sites with 0.65 and 0.51 eV binding energy, respectively. On the singlet PES, no physisorption state was found. The bridge site is the only stable binding site, forming an epoxide moiety with an elongated C-C bond (r=1.5 Å) and two C-O bonds (r=1.5 Å). The binding energy at the bridge site is 1.91 eV relative to the triplet asymptote. These results are consistent with previous DFT calculations,[223-227] which follow the lower adiabat because the spin of the system was not specified. The PESs of the two spin states cross when the O-atom is relatively far (~ 2 Å) from surface and the intersection seam is almost isoenergetic to the triplet asymptote (Fig. S11), but the crossing seam might contain significant uncertainties given the inability of DFT to reproduce the ^{1}D-^{3}P energy difference of atomic oxygen. For the impinging O(^{3}P) atom, it is possible to hop to the singlet state or stay in the triplet state, which will lead to different dynamical results. The incident O(^{1}D) atoms also face the choice of either staying on the singlet state or hopping to the triplet state as they reach the intersection.

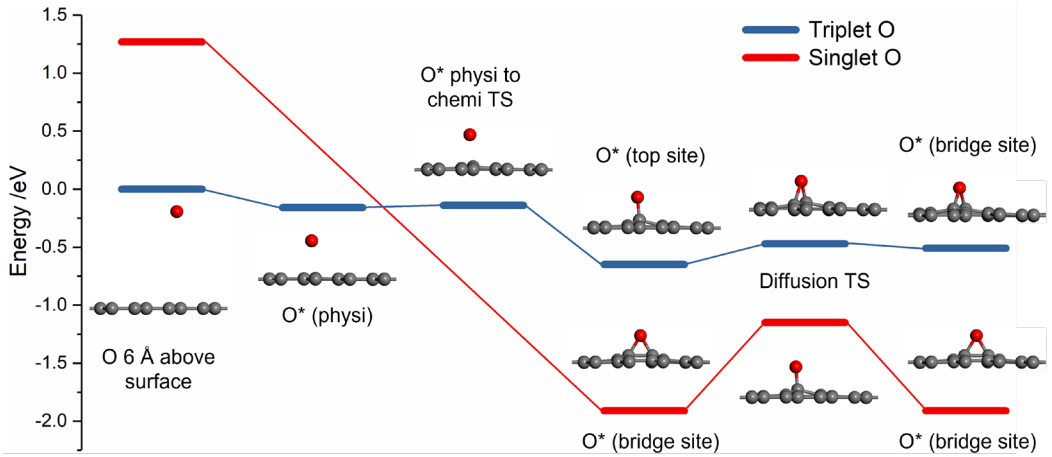

Figure 1. DFT stationary points on the triplet (blue) and singlet (red) PESs for atomic oxygen on graphene. The triplet PES has a shallow physisorption well with O 2.3 Å above the surface and exhibits chemisorption

at top and bridge sites with binding energies of 0.65 and 0.51 eV, respectively. The singlet PES does not have a physisorption well but exhibits strong chemisorption at the bridge site (1.91 eV binding energy relative to the O(^{3}P) asymptote.) The two PESs cross at a seam of intersection located near the physisorption barrier on the triplet PES. In the O(^{1}D) scattering simulations, the singlet PES was shifted upwards by 0.7 eV to match the ^{1}D/^{3}P energy gap of the atomic oxygen.

Scattering of O(^{3}P). Using the 87% O(^{3}P) discharge source, we measured the energy and angular distributions of scattered O atoms. We looked for atoms in the O(^{1}D) state but did not find any. Using the incoming/outgoing ion imaging correlation method we determined the angular and kinetic energy distributions of scattered O(^{3}P) atoms with $\langle E_i \rangle$=0.34±0.05 eV at an incidence angle of 20°. The results are displayed in Fig. 2a. (Distributions obtained at other incidence angles are shown in Fig. S9.) The angular distribution is peaked close to the specular angle and the energy distribution is peaked at a value of $E_s/E_i \approx 0.47$. Furthermore, the scattering energy distribution clearly depends on the incidence energy, as shown in Fig. 2d. These results indicate that the observations are dominated by a direct inelastic scattering mechanism with ≲1 ps surface residence time, as has been reported previously in O/HOPG scattering experiments performed at T_{surf} = 298 K.[101, 228]

O(1D) scattering experiments with the 94% O(^{1}D) source. The beam consists of both O(^{1}D) and O(^{3}P) atoms but the O(^{3}P) are much faster and consequently arrive at the surface much earlier. Fig. 3a shows the flux of incident and scattered O atoms as a function of t_{probe}. Incident O(^{3}P$_2$) atoms reach the detection laser about 40 μs after the photolysis laser, whereas incident O(^{1}D) atoms arrive between ~80–220 μs. Note that the surface-arrival time distributions of the O(^{1}D) and O(^{3}P) atoms are separated in time, making state-to-state measurements of the scattered atom distribution possible. No scattered atoms could be detected in the O(^{1}D) state, but scattered O(^{3}P) atoms were

detected with a broad t_{probe} distribution between 30 and 250 μs after the photolysis laser also shown in Fig. 3a.

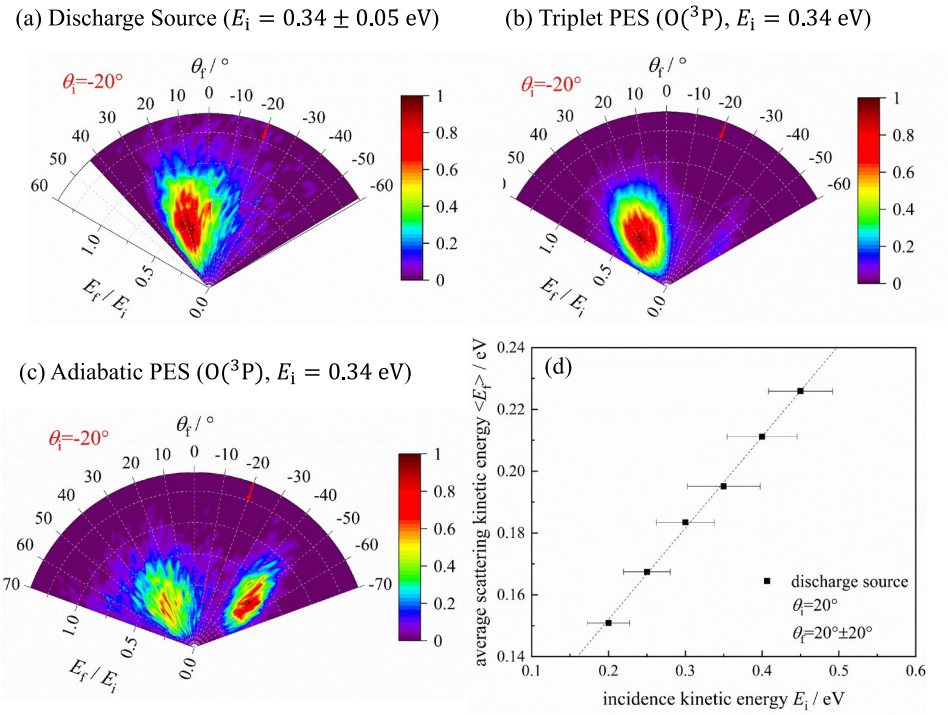

Figure 2. (a) The experimental kinetic energy and angular distribution of O(^{3}P$_2$), obtained after scattering atomic O (E_i=0.34±0.05 eV) from HOPG at an incidence angle of −20°. Calculated scattering distributions at an incidence energy of E_i=0.34 eV and an incidence angle of 20° are plotted in panels (b) and (c) using the triplet PES and adiabatic PES, respectively. The average scattered kinetic energy, derived from experiment, is plotted as a function of incidence kinetic energy in panel (d). The horizontal error bars indicate the FWHM of the incidence energy distribution corresponding to each data point.

Fig. 3b shows the results when applying the incoming/outgoing correlation methods. Here we compare the distribution of t_{arrive} for the incident O(^{1}D) and O(^{3}P) atoms with the distribution of t_{depart} for the scattered O(^{3}P) atoms. (The details of the correction for the surface to probe laser flight time are illustrated in Fig. S4 of the SM.) There is a small contribution of incident O(^{3}P) atoms at early times, giving rise to a peak at ~40 μs, but the primary scattering component, which extends from 90–250 μs, has a t_{depart} distribution that closely matches the surface-arrival time

distribution of $O(^1D)$ atoms, which allows us to definitively assign the primary component of the signal from $O(^3P)$ leaving the surface to a spin-changing process involving $O(^1D) \rightarrow O(^3P)$ conversion induced by the collision at the surface. (Note that the small peak at 85 μs marked with an asterisk is an artefact arising from a small contamination of O_2 in the CO_2 precursor beam.)

Figure 3c shows the $O(^1D) \rightarrow O(^3P)$ scattering energy distribution for $E_i = 0.065 \pm 0.02$ eV. The most probable scattering energy E_s^{MP} is ~0.1 eV and the distribution extends more than 0.3 eV higher than E_i. This excess translational energy must come from the incidence electronic energy (1.97 eV). Remarkably, only a small fraction (~5%) of the incidence electronic energy is converted to translation. The results also show that the spin-forbidden $O(^1D) \rightarrow O(^3P)$ channel occurs without complete thermalization of the adsorbed atom to the surface. Comparing Figs. 3c and d, where the incidence energy is increased from 0.065 to 0.23 eV, we see that E_s^{MP} also increases from 0.1 to 0.2 eV. This *memory effect* rules out the possibility of a substantial residence time at the surface and at the same time validates the assumption $t_{\text{arrive}} = t_{\text{depart}}$, used in the incoming/outgoing correlation method. Additional evidence of electronic to translational energy conversion is seen in Fig. 3d, where the scattering energy distribution obtained for incident $O(^3P)$ and $O(^1D)$ are compared at $E_i = 0.23 \pm 0.05$ eV. Note that the observed energy of departing $O(^3P)$ is significantly smaller than that obtained for incident $O(^1D)$.

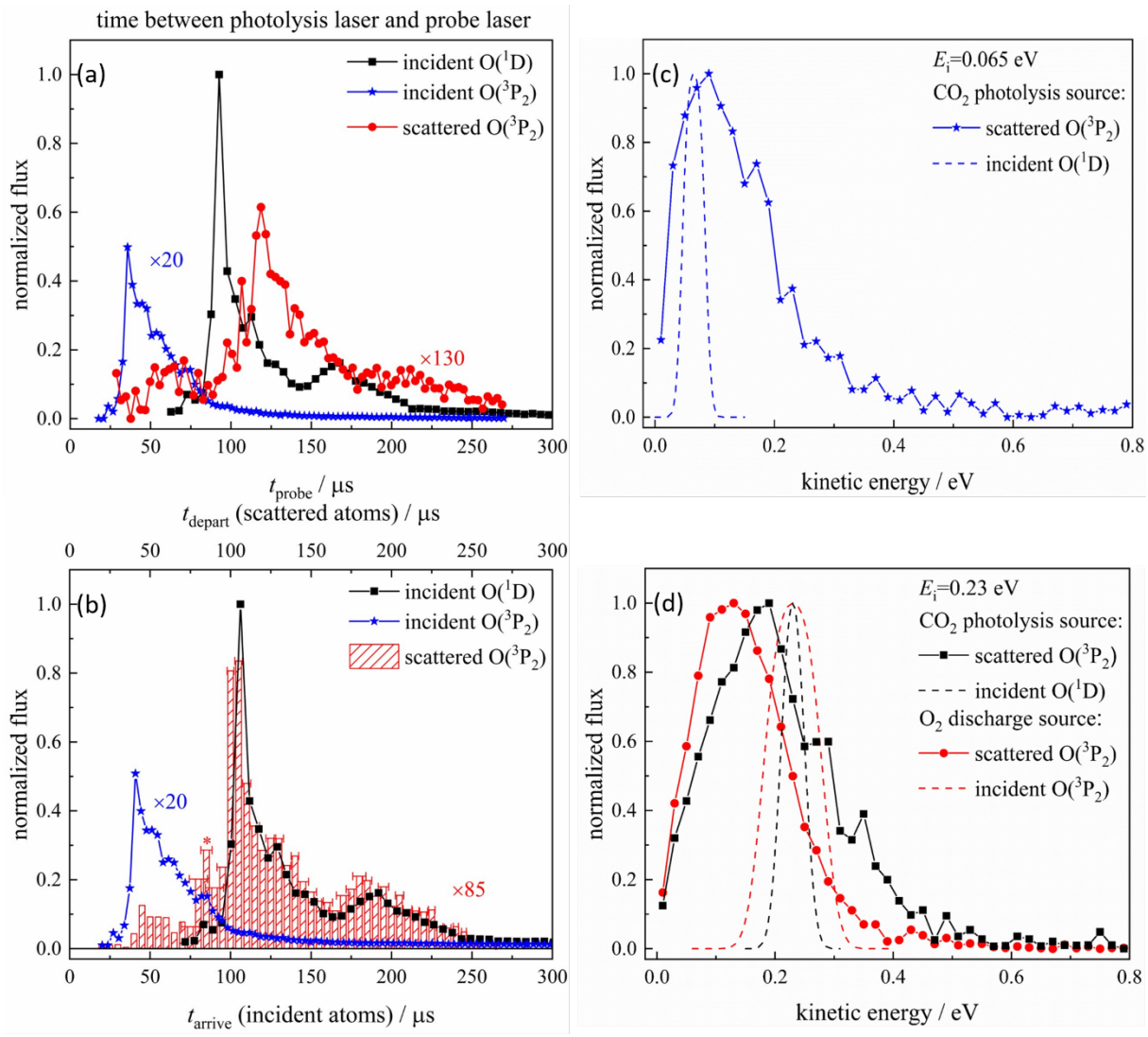

Figure 3. (a) The flux of incident $O(^3P_2)$ (blue stars), incident $O(^1D)$ (black squares), and scattered $O(^3P_2)$ (red circles) in the CO_2 photolysis experiment are plotted as a function of t_{probe}. (b) The t_{arrive} distribution for incident $O(^1D)$ and $O(^3P_2)$ is compared with the t_{depart} distribution for scattered $O(^3P_2)$. The widths of the red shaded rectangles indicate the size of the t_{depart} histogram intervals and the horizontal error bars indicate the FWHM uncertainty in t_{depart} due to uncertainty in the velocity measurements. The peak at 85 μs (marked with an asterisk) is an artefact due to a small contamination of O_2 in the CO_2 molecular beam. (c) The scattering kinetic energy distribution for the $O(^1D)\rightarrow O(^3P_2)$ channel is shown for incident O assigned to $\langle E_i\rangle$=0.065±0.020 eV (blue stars). The distribution of incidence energies (including experimental uncertainty) is shown as a blue dashed curve. (d) The scattered $O(^1D)\rightarrow O(^3P_2)$ kinetic energy distribution from the CO_2 photolysis source assigned to $\langle E_i\rangle$=0.23±0.02 $\langle E$i$\rangle$=0.2±0.02 eV (black squares) is compared to the distribution obtained from the O_2 discharge source (red circles) with a similar range of

incidence energies ($\langle E_i \rangle$=0.23±0.05 eV). The incidence energy distributions are indicated by black and red dashed curves, respectively.

The sticking probabilities of $O(^1D)$ are uniformly larger than those of $O(^3P)$ as shown in Fig. 4. Experimental sticking probabilities were derived by comparing the ratio of total incident and scattered flux from the CO_2 photolysis and O_2 discharge sources, respectively, assigned via the incoming/outgoing correlation method (see Section 2.4 of the SM for details). Despite rather larger error bars, it is unmistakable that $O(^1D)$ exhibits ~7 × higher sticking probability than $O(^3P)$.

Simulation results for $O(^3P)$ scattering. To test the validity of spin conservation in the dynamics, MD simulations were carried out on both the triplet and adiabatic PESs. Figure 2 compares the experimental results (panel 2a), obtained for the $O(^3P) \rightarrow O(^3P)$ channel at E_i=0.34±0.05 eV and θ_i=20° with the theoretical results calculated for the same incidence conditions using both the triplet (2b) and adiabatic (2c) PESs. Similar results at different incidence angles are included in Fig. S9. The experimental distribution can only be reproduced by use of the triplet PES. Dynamics calculations on the adiabatic PES yield a bimodal angular distribution, in which the backscattering peak can be attributed to the strong corrugation of the graphene surface towards O atom. No evidence of this backscattering peak is seen in experiment. The sticking coefficients for $O(^3P)$ obtained from MD simulations are shown in Fig. 4, where the value from spin-conserving (triplet) simulation is shown to be significantly smaller than that from spin-relaxed adiabatic simulation and closer to experiment. (See Section 2.4 of the SM for details.)

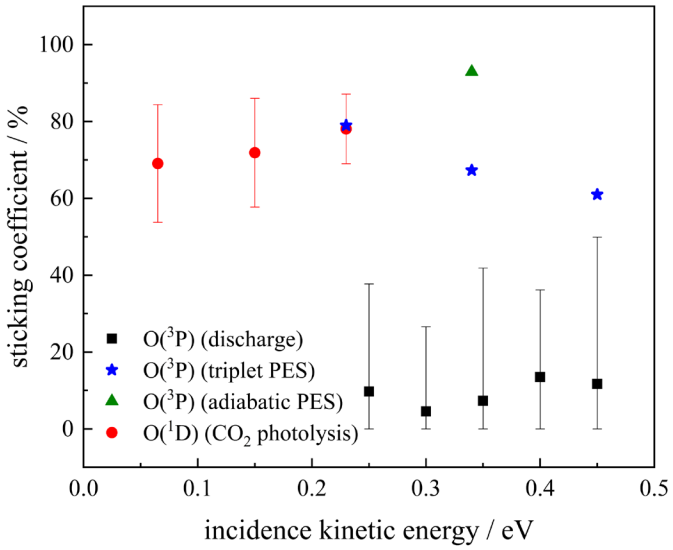

Figure 4. Measured sticking coefficients for $O(^1D)$ from the CO_2 photolysis experiment (red circles) and for $O(^3P)$ from the O_2 discharge experiment (black squares) are plotted with 95% confidence intervals as a function of incidence kinetic energy. Calculated sticking coefficients for $O(^3P)$, obtained from trajectory calculations on the adiabatic PES (green triangle) and triplet PES (blue star) are also shown.

Simulation results for O(^{1}D) scattering. Two different MD simulations were performed for scattering of $O(^1D)$ atoms at an incidence energy of 0.23 eV and an incidence angle along the surface normal, where comparison to experiment is possible. The first simulation employed the singlet PES, neglecting possible singlet-triplet crossing. Here, all trajectories led to sticking, which is consistent with the absence of $O(^1D) \rightarrow O(^1D)$ scattering in the experiment (Fig. 3b).

The second simulation models singlet-triplet coupling in a semi-empirical way. A proper simulation of the non-adiabatic intersystem crossing dynamics requires the knowledge of the coordinate-dependent spin-orbit coupling between the singlet and triplet states, which is very challenging for this high-dimensional system and beyond the scope of this work. Instead, the following strategy was used to consider spin non-conserving dynamics.

As the impinging $O(^1D)$ atom first approached the singlet-triplet seam, no transition to the triplet was permitted in our model; this is justified by the high velocity of the incident atom. The

O atom then forms a hot adsorbate structure and begins relaxing to form the stable epoxide-like bridge site species. During the course of relaxation, the O atom continues to attempt crossings of the singlet-triplet seam, but it does so with decreasing velocity and thus increasing probability for a transition to the triplet. We simulated the effect of this time varying spin flip probability with the following ad hoc procedure. We imposed a singlet-triplet crossing delay, τ_{S-T}. Any trajectory that reaches the singlet-triplet seam in the outgoing direction after this time delay is allowed to cross to the triplet PES with 100% probability. Very few such spin flips were observed, as the fast energy dissipation of the hot adsorbate rapidly prevents the trajectory from approaching the seam, which lies ~2 eV above the singlet PES minimum. See Section 2.5 of the SM for more details.

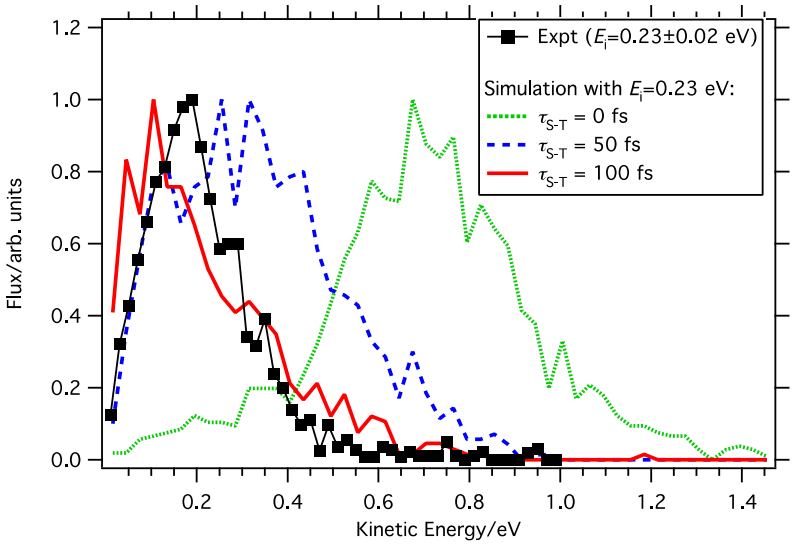

Figure 5. The final kinetic energy distribution for the scattered atomic oxygen, initially in the ^{1}D state, from HOPG via the spin non-conserving O(^{1}D)→O(^{3}P) channel. Simulations were performed in which the spin flip was allowed to occur when the singlet/triplet seam of intersection is crossed in the outgoing direction only after a chosen delay, as described in the main text. Simulated results are shown for an incidence kinetic energy of 0.23 eV and a delay of 0 fs (green dotted line), 50 fs (blue dashed line), and 100 fs (red solid line). The experimental results corresponding to an incidence kinetic energy range of 0.23±0.02 eV is shown for comparison (black squares).

Figure 5 compares the experimental distribution for scattered O(^{3}P) atoms resulting from incident O(^{1}D) with calculated results. When the singlet→triplet transition is assumed to occur immediately (τ_{S-T} = 0 fs), a much larger fraction of the electronic energy of incidence is channeled to translation energy of the scattered atom. As τ_{S-T} increases, the trajectories that undergo seam crossing back to the triplet result from a partially relaxed adsorbate, which leads to reduced translational energy in the outgoing atom. When τ_{S-T} =100 fs, the simulated kinetic energy distribution agrees well with experiment. We caution against taking this value of τ_{S-T} as an accurate estimate of the actual singlet-triplet crossing delay. It represents the time required for the nascently adsorbed O atom to lose sufficient kinetic energy to undergo a spin-flip transition and, due to the small size of our model system, the energy relaxation rate is probably not quantitatively accurate. What is clear is that a prompt spin relaxation, τ_{S-T} =0, is incompatible with the experimental results. Furthermore, the ability of the model to reproduce experiment only with a substantial singlet-triplet delay suggests that the spin-orbit coupling is small, consistent with the small atomic numbers of the constituting atoms.

5.4 Summary and conclusion

Using a novel high-resolution state-to-state scattering approach, we experimentally investigate the spin-state selective scattering of O atoms and their adsorption to HOPG to explore the spin-dependent reactivity and spin-flipping dynamics in surface chemistry. Detailed DFT and MD calculations on high-dimensional PESs machine-learned based on DFT data are performed to gain a more in-depth understanding of the experimental observations. Both experiment and theory reveal large sticking probabilities for O(^{1}D), which are attributed to the formation of a surface bound epoxide, with a ~2 eV binding energy to the surface relative to the triplet asymptote. The nascent epoxide adsorbate formed by collision of O(^{1}D) at the surface possesses ~4 eV of

vibrational energy and rapidly relaxes below the desorption asymptote. The only mechanism by which $O(^1D)$ may return to the gas phase involves a spin flip to the triplet state, which is indeed observed in our experiment. Semi-empirical dynamics simulations show that this spin flip must occur after the impinging oxygen atom dissipates a significant portion of its energy to the HOPG surface, but before it reaches thermal equilibrium.

Sticking probabilities for $O(^3P)$ are smaller than those of $O(^1D)$ but are still significant under the conditions explored in this work. The fact that experimental angular and kinetic energy distributions are consistent with the theoretical simulations performed using the triplet PES allows us to conclude that triplet→singlet→triplet conversion does not readily occur at the surface during direct scattering trajectories at incidence energies around 0.34 eV. The most likely sticking mechanism involves dissipation of incidence kinetic energy on the triplet PES followed by spin relaxation to the lower singlet state on longer timescales.

These conclusions are consistent with the scattering results of atomic oxygen from the 94% $O(^1D)$ CO_2 photolysis source, where the scattering kinetic energy distribution of the $O(^1D)$→ $O(^3P)$ channel involves hyperthermal yet still relatively low translational energies in comparison to the nearly 2 eV of incidence electronic energy (Fig. 3 and Fig. S7). Since the seam of intersection is near the triplet asymptote, the observed energy of the scattered $O(^3P)$ closely reflects its kinetic energy at the seam of intersection. The high sticking coefficients (Fig. 4) are consistent with this picture. The inefficiency of spin relaxation for incident $O(^3P)$ atoms limits their likelihood of sticking to the surface, whereas the inability of $O(^1D)$ to convert to $O(^3P)$ when the kinetic energy at the seam of intersection is too high leads to enhanced $O(^1D)$ sticking. These observations underscore the two important factors in spin-flipping dynamics in surface chemistry, namely the efficiency of vibrational energy dissipation and strength of the spin-orbit coupling. The picture

that emerges from this study is that spin-forbidden transitions do occur in this system, but with low probabilities.

5.5 Supplementary material

5.5.1 Methods

5.5.1.1 Experimental

Figure S1 shows an overview of the experimental setup. The discharge nozzle is directed along the atomic beam axis with the discharge region 342.5 mm from the HOPG surface. The molecular beam nozzle for photolysis is mounted at 90° to the beam axis with the photolysis region 174 mm from the surface. The REMPI probe laser is focused 22 mm in front of the surface.

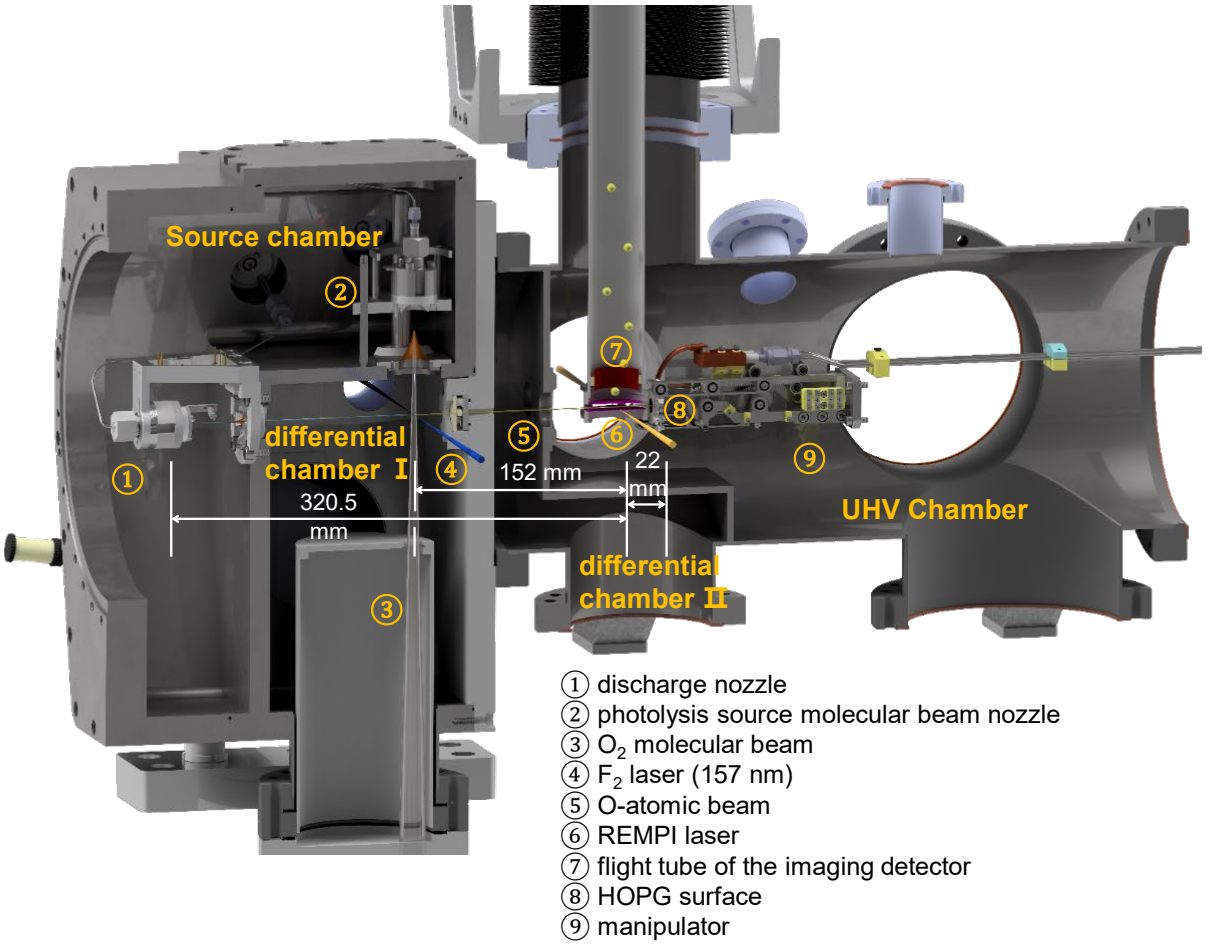

Figure S1. Schematic of the experimental setup of the atomic beam scattering apparatus. The flight distance from the discharge source (1) to the REMPI probe laser (6) is 320.5 mm, whereas the distance from the photolysis region (overlap of the CO_2 molecular beam (3) with the focused F2 laser (4)) to the REMPI laser is 152 mm. The incident atomic beam flies from left to right across two differentially pumped chambers before entering the UHV chamber, where it impinges upon an HOPG surface (8) mounted on a manipulator (9). The surface is located 22 mm from the REMPI laser. Oxygen ions are extracted into a flight tube (7) through which they are sent upward towards an imaging detector (not shown).

Discharge source. Figure S2 shows a schematic of the components of the discharge source. In the discharge region there is a conical electrode and a ground electrode. A ceramic electrode holder and a ceramic electrode spacer are installed between the two electrodes. A −1200 V pulse with 20 μs width is applied to a copper ring attached to the conical electrode, shown in yellow color. An expansion of O_2 seeded in helium passes through the discharge region, where atomic oxygen is formed. The discharge current (~40 mA) is monitored during the discharge. During the discharge a simmer voltage of −1500 V is applied to a copper wire brush mounted off-axis 2.5 cm downstream of the orifice. Electrons that are emitted from the brush stabilize the pulsed discharge current by pre-ionization (<100 ns temporal jitter and 1% amplitude fluctuation).

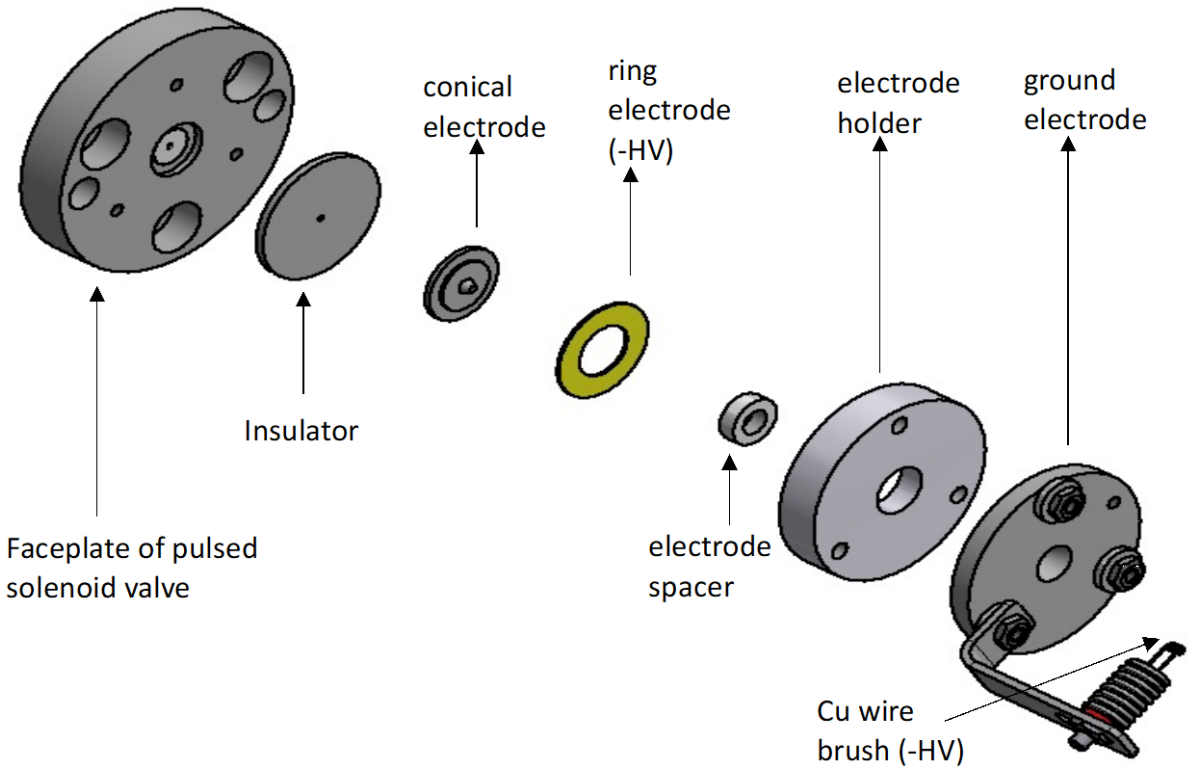

Figure S2. Expanded schematic drawing of the O-atom discharge source.

Photolysis source. For the photolysis process a molecular beam of CO_2 is introduced to the source chamber by a home-built pulsed solenoid valve based on the Even-Lavie design [229]. This molecular beam is collimated by a 2 mm skimmer and subsequently photodissociated by a 157 nm F_2 laser (Coherent LPF Pro 205 F 400 VAC, about 20 mJ pulse energy), focused by a f = 400 mm lens, to produce the atomic oxygen beam, which is perpendicular to the pulsed molecular beam and VUV laser.

UHV Chamber and Detector. The atomic oxygen enters the UHV chamber through a 3 mm × 1 mm (horizontal × vertical) rectangular aperture before impinging on the target surface. Prior to each set of scattering experiments, the surface is annealed by electron bombardment heating at 450 ℃ for 30 minutes. The cleanliness and structure of the surface is characterized by low-energy electron diffraction (LEED) and Auger electron spectroscopy (AES). Under the conditions in

which experiments were performed, the LEED pattern and AES spectrum were consistent with pristine sp^2 carbon—the oxygen coverage was below the AES detection threshold.

The resonance-enhanced multiphoton ionization (REMPI) detection of the incident and scattered O-atoms makes use of a tunable UV dye laser (Sirah Cobra Stretch CBST-G-18 + THU-205-N), operated with DCM, Rhodamine B, and Rhodamine 101 dyes and pumped by the second harmonic of a Nd:YAG laser (Innolas Spitlight 600 S/N P1754) operated at a repetition rate of 50 Hz. The fundamental is frequency tripled by a pair of BBO crystals yielding the desired ionizing radiation in the 200 to 240 nm range with a pulse energy of 0.4–2.0 mJ and a pulse duration of 8 ns. The laser beam is focused by a 250 mm lens into the region between the repeller and extractor of the detector. The focusing lens is mounted on a motorized translation stage so that the focus can be scanned along the laser propagation direction. During scattering experiments, the laser focus is continuously scanned back and forth so that the effective detection efficiency is uniform along the laser propagation direction. The *J*-resolved detection of $O(^3P_{2,1,0})$ is achieved by (2+1) REMPI via the 3p ^{3}P intermediate state at wavelengths of 225.654, 226.059 and 226.233 nm, respectively [230], and $O(^1D)$ atom is detected by (2+1) REMPI via the $^1F \leftarrow {}^1D$ transition at 203.812 nm [231].

The laser ionization takes place between a pair of 45 mm diameter extractor and repeller grids that are separated by 5 mm. After ionization, an extraction delay of typically 0.1–2 μs is introduced before pulsing the repeller grid to +2500 V. The extraction delay results in slice imaging [232-233], which selects only the component of the atoms that scatter in the plane defined by the incident atomic beam and probe laser axes. Mass selection is achieved by pulsing the MCP voltage, and the two-dimensional velocity is extracted from the ion image, obtained either in spatial imaging mode (without Einzel lens) or velocity mapping mode (with the Einzel lens turned on). The time-of-flight tube to the detector has a length of 44 cm. The scattering angular

distribution that can be imaged at a given time is limited by the detector cutoff to approximately $\pm 25°$ from the surface normal. However, the detector can be translated along the probe laser propagation direction to increase the measurable range to $-45°$ to $+65°$ relative to the surface normal.

5.5.1.2 Incoming/Outgoing Correlation Ion-imaging: high resolution scattering with "bad beams"

Most previous studies using energy-resolved atomic beam scattering experiments have relied on diatomic molecules as photolysis precursors because energy and momentum conservation lead to sharp incidence kinetic energy (E_i distributions. Our CO_2 photolysis and O_2 discharge sources lead to incident O-atom beams with broad E_i distributions, but velocity-resolved detection allows us to probe significantly below the energy resolution afforded by the incident beam. In particular, since the photolysis occurs in a narrow time window (20 ns) and well-defined spatial region (~2 mm broad), different incidence velocity components spread out during the long flight distance from the photolysis region to the surface (174 mm) and reach the surface at different times. This is illustrated in Fig. S3. The center panel of Fig. S3 shows the ion image of incident oxygen atoms from the CO_2 photolysis source, probed at the REMPI laser position $d_{\mathrm{REMPI-surface}}$ = 22 mm in front of the surface at three different photolysis-probe laser delays. The arrival time-dependence of the incidence velocity that was obtained from the ion images was found to match the result calculated from the 152 mm flight distance between the photolysis and probe laser divided by the photolysis-probe laser delay (Eq. 2 of the main article). Since the incidence velocity (v_i) of each atom is known, it is trivial to calculate its arrival time at the surface from

$$t_{\mathrm{arrive}} = t_{\mathrm{probe}} + \frac{d_{\mathrm{REMPI-surface}}}{v_i} \qquad \text{(S1)}$$

which allows us to construct a plot of $\langle E_i \rangle$ vs t_{arrive} (Fig. S3, left-hand side).

VMI images of the scattered atoms are obtained as a function of the photolysis-probe laser delay, t_{probe}. The total flux of scattered atoms detected at each delay is shown in the left-hand panel of Fig. S4, and representative ion images obtained at three delays are shown at the top of Fig. S4. Since the velocity components of each scattered atom are also measured at each probe laser delay, the time at which each REMPI detected atom left the surface is calculated from

$$t_{\text{depart}} = t_{\text{probe}} - \frac{d_{\text{REMPI-surface}}}{v_{z,f}} \qquad \text{(S2)}$$

where $v_{z,f}$ is the component of velocity of the scattered atom along the incident beam direction. The boxed regions shown in the ion images of Fig. S4 represent the assignment of ions into 10 μs histogram intervals of t_{depart}. The overall t_{depart} distribution (right-hand panel of Fig. S4) is obtained by summing the histograms obtained at each value of t_{probe}.

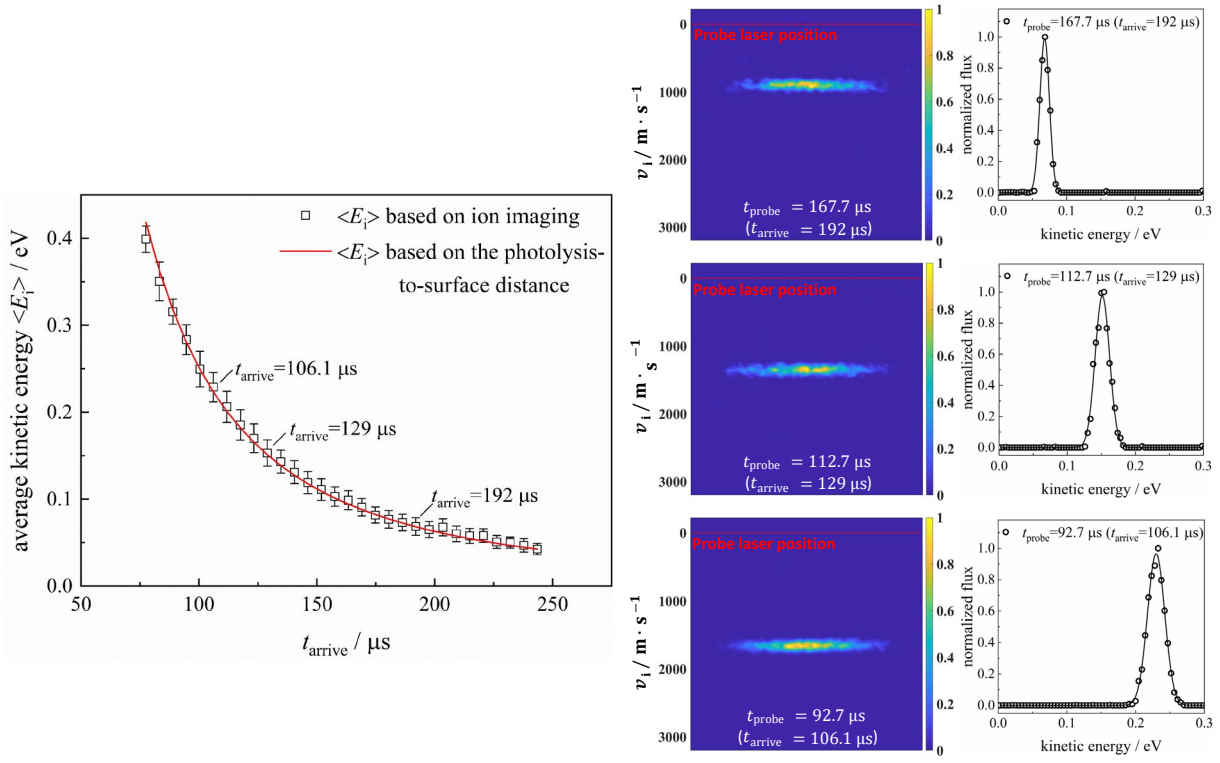

Figure S3. The relationship between arrival time at the surface and the expectation value of incidence kinetic energy is shown in the left panel for the O atom beam obtained from the CO_2 photolysis source. The

black square markers indicate the value of <E_i> obtained from ion imaging and the error bars indicate the FWHM of the instantaneous E_i distribution obtained at each delay. The red curve shows the expected arrival time dependence of kinetic energy derived from the experimental geometry. The ion images at t_{probe} =92.7 μs, t_{probe} =113 μs, and t_{probe} =168 μs are illustrated in the middle panel, and their corresponding kinetic energy distributions are shown in the right panel.

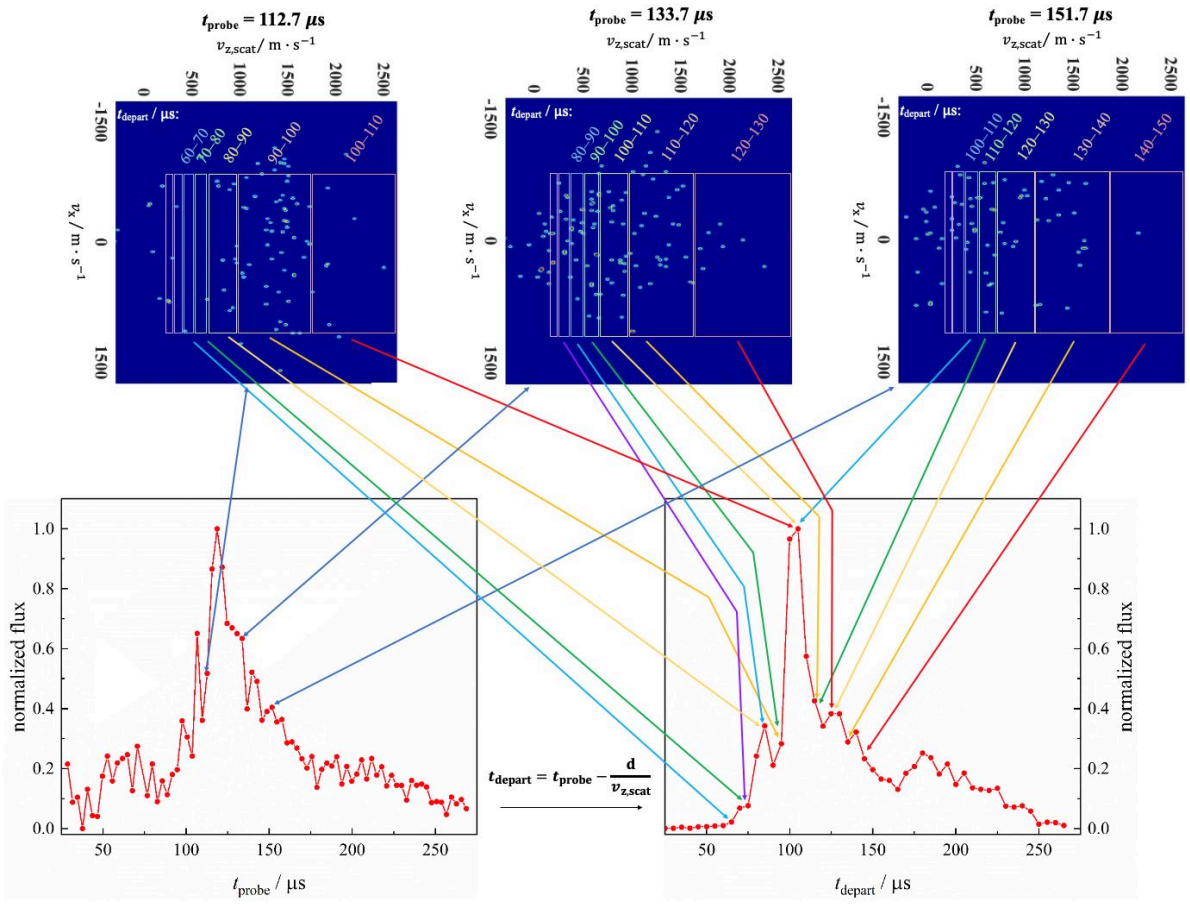

Figure S4. The lower left panel shows the total density of scattered O ($^3P_2$) atoms obtained using the CO_2 photolysis source as a function of the photolysis-probe laser delay, t_{probe}. VMI images obtained at three representative delays are shown at the top. For each ion in the image, the departure time from the surface, t_{depart}, is calculated from $v_{z,f}$ using Eq. S2. The rectangular boxes drawn over the ion images represent 10 μs histogram intervals for t_{depart} (as labeled). The overall t_{depart} distribution obtained by summing the histograms for every image is shown in the lower right panel. The contribution of ions to different t_{depart} intervals is indicated by colored arrows. Due to the broad distribution of scattered velocities, ions from images obtained at multiple different t_{probe} delays contribute to each interval of t_{depart}.

For direct scattering phenomena described in the current work, the $\lesssim$ ps residence time at the surface can be considered negligible, which allows us to equate t_{arrive} with t_{depart} and assign a value of $\langle E_i \rangle$ to each scattered atom based on the arrival-time dependence of $\langle E_i \rangle$, which can be read from the left panel of Fig. S3. A much higher energy resolution than the width of the E_i distribution is obtained by selecting only those scattered atoms assigned to a particular $\langle E_i \rangle$ interval.

The approach can also be applied to experiments involving the discharge source with the only difference being that the arrival times of different incidence kinetic energy components are less well resolved ($\sim$20% E_i resolution), since the O atoms are generated over a broader time window ($\sim 20\ \mu$s) and in a broader spatial region ($\sim$4 mm) compared to the photolysis source. Figure S5 illustrates the relationship between arrival time at the surface, t_{arrive}, and incidence kinetic energy, E_i, obtained with the discharge source. The central panel shows ion images of the incident atomic beam acquired at three different t_{probe} delays, defined as the delay between the maximum of the discharge current pulse and the firing of the REMPI probe laser. For each image, the expectation value of t_{arrive} is calculated from Eq. S1 using the measured velocity distribution. The distance $d_{\text{REMPI-probe}}$ between the probe laser and surface was 22 mm. The incidence kinetic energy distribution corresponding to each image is shown in the right-hand side of Fig. S5, and the relationship between t_{arrive} and E_i is shown in the left-hand panel. Vertical error bars represent the FWHM of the instantaneous distribution of E_i of atoms impinging on the surface at each point in time. There is a clear time dependence of $\langle E_i \rangle$, but the energy resolution is only approximately 20%, due primarily to the finite ($\sim 20\ \mu$s) length of the discharge current pulse. The red curve through the data represents the expected value of $\langle E_i \rangle$, calculated from the 320.5 mm distance between the discharge source and the surface and the time delay (Eq. 2 of the main text).

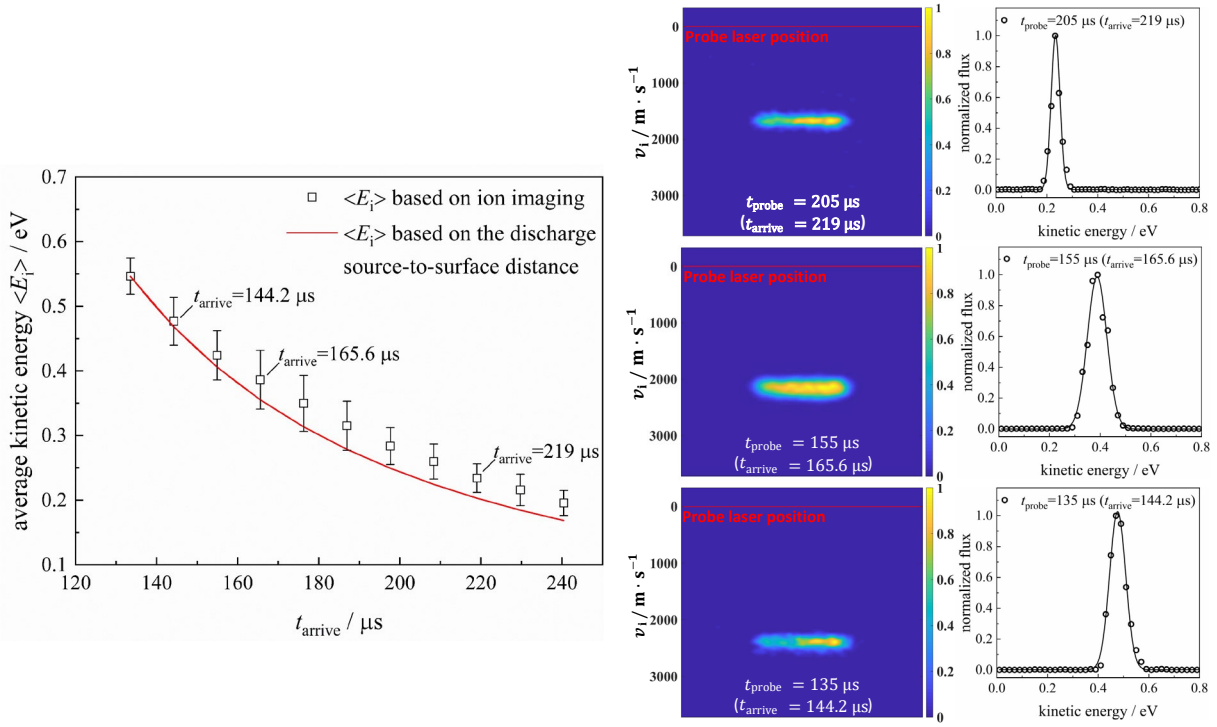

Figure S5**.** The center panel shows ion images of incident O $^3P_2$ atoms from the discharge source obtained at different t_{probe} delays. The corresponding kinetic energy distributions are displayed in the right-hand side of the figure and the expectation value of arrival time at the surface for each group of atoms is indicated in the figure. The left-hand panel shows the expectation value of incidence kinetic energy as a function of arrival time at the surface. Vertical error bars represent the FWHM of the instantaneous distribution of incidence energies derived from the measurement. The red curve shows the expected time dependence of E_i, based on the distance from the discharge source to the surface.

5.5.1.3 Computational methods

Density Functional Theory (DFT). The computational results were obtained from plane-wave DFT calculations performed using the Vienna Ab initio Simulation Package (VASP) [94, 234]. The PBE functional is used to calculate the exchange-correlation term based on the generalized gradient approximation (GGA) [235]. The electron−ion interaction is described by the projector augmented-wave method (PAW) [236]. The energy cutoff of the plane-wave basis is set to 400 eV. The HOPG surface is modeled by periodic slabs with one-layer 4×4 cell containing 32 movable C

atoms and a vacuum space of 15 Å in the *z*-direction. The Brillouin zone is sampled with a 2 × 2 × 1 *k*-point grid.

The spin-constrained triplet calculations are carried out using spin-polarization with NUPDOWN=2, while the singlet calculations are performed with spin-unpolarized DFT.

The O atom adsorption energy is calculated according to

$$E_{\mathrm{ad}}(\mathrm{O}) = E_{\mathrm{O@Gra}} - E_{\mathrm{O}} - E_{\mathrm{Gra}} \qquad \text{(S3)}$$

where $E_{\mathrm{O@Gra}}$, E_{O} and E_{Gra} are the energy of the whole system, the O atom in gas phase and the isolated graphene sheet.

Ab Initio Molecular Dynamics (AIMD). About 400 AIMD trajectories are calculated with an O atom incidence energy of 1.0 eV along the surface normal at a surface temperature of 300 K. The system is constrained to either the singlet or triplet state throughout the simulation, using the spin-constraining recipe described above. The initial position of the O atom is evenly sampled over the unit cell at 6 Å above the surface.

NN PES fitting. PESs with 33 movable atoms (99 dimensions) are fitted with the Embedded Atom Neural Network (EANN) method [86], which enforces full permutation symmetry. 120000 points (energies and gradients) are used in the fitting. These points are culled from the AIMD trajectories using a criterium based on the Euclidean distance larger than 0.3 Å. The fitting quality of the singlet and triplet PESs is given by root mean square errors (RMSEs) of 19 and 26 meV, respectively. These two PESs intersect, as shown in Figure 1, and the lower energy one of the two PESs forms the adiabatic spin-relaxed PES.

5.5.2 Results

5.5.2.1 Scattering experiments with the O_2 discharge source

Under the conditions used in this experiment, the O-atom discharge source gave rise to an incident O atom beam with a state distribution of ^3P:^1D=0.867±0.018:0.133±0.018 and $^3P_2$: $^3P_1$: $^3P_0$=0.933±0.038:0.053±0.031:0.014±0.007. The incident beam had a broad kinetic energy distribution peaked at 0.36 eV with a FWHM of 0.2 eV (see Fig. S6, left panel). The overall angular and kinetic energy distribution of incident and scattered O $^3P_2$ atoms obtained in the discharge experiment is shown in Fig. S6 for three different incidence angles. Using the incoming/outgoing correlation method, we assigned a value of $<E_i>$ to each scattered atom. The solid red curve in Fig. 3d of the main text includes only those atoms with $<E_i>$ in the range 0.23 ± 0.05 eV. Figure 2d of the main text shows the dependence of the mean scattered kinetic energy on the incidence energy.

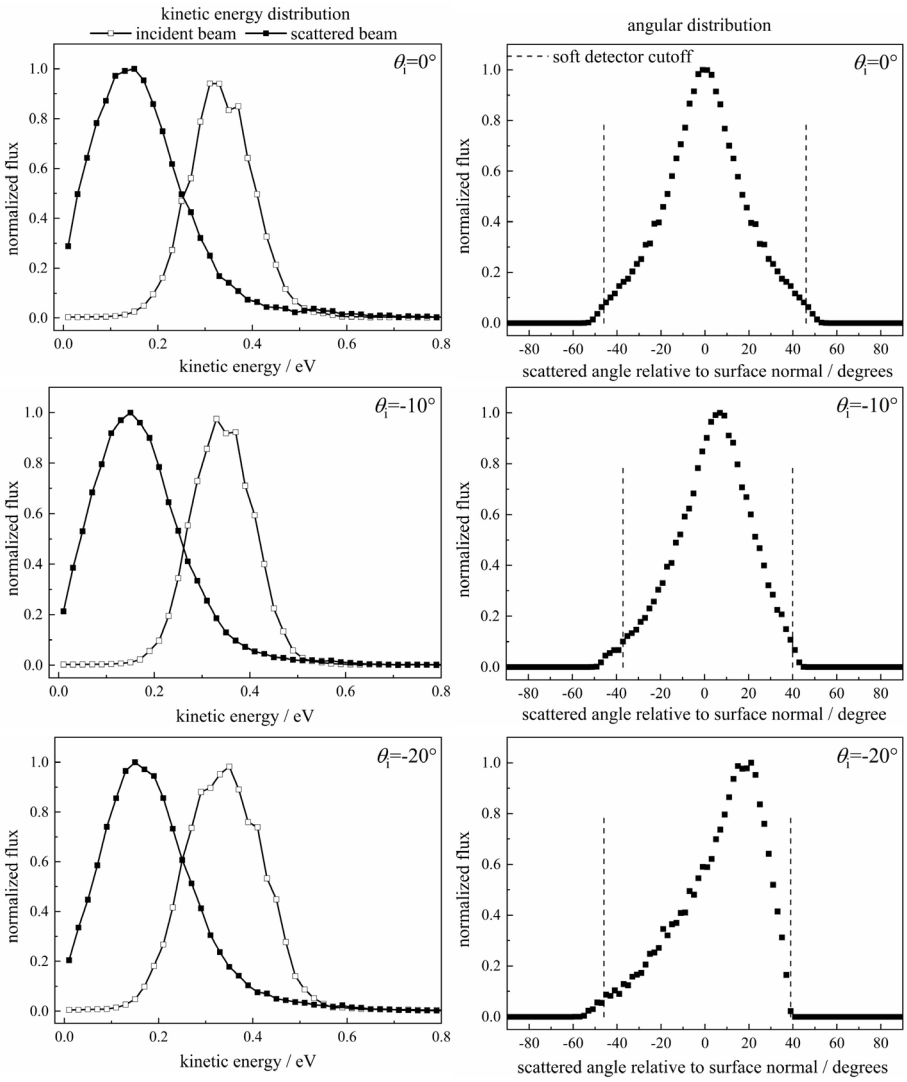

Figure S6. Scattering characteristics of the O$^3P \rightarrow {}^3P$ channel. Left panel: The kinetic energy distributions of incident O $^3P_2$ atoms generated by running 1% O_2/He at a stagnation pressure of 10 bar through a pulsed discharge source, operated with a discharge voltage of −1200 V and a discharge current pulse width of 20 μs, is shown with open squares and the kinetic energy distribution of O($^3P_2$) atoms scattered from HOPG at normal incidence angle is shown with solid squares. The angular distribution of scattered O($^3P_2$) is shown in the right panel. The dashed vertical lines indicate the angles at which a portion of the ions start to be cut off due to the detector geometry. The portion of the angular distribution between the dashed lines can be considered reliable.

5.5.2.2 $O(^1D)$ Scattering experiments with the CO_2 photolysis source

The overall kinetic energy distribution of the incident $O(^1D)$ and scattered $O(^3P_2)$ atoms are shown in Fig. S7. The incident $O(^1D)$ atoms have a broad kinetic energy distribution with peaks at 0.065 and 0.23 eV, which correspond to formation of the CO co-product in the v=1 and v=0 states, respectively. Both peaks are broadened due to the population of many CO rotational states. The scattered kinetic energy distribution is broad, with a peak at around 0.15 eV. Such a hyperthermal distribution is consistent with a direct scattering mechanism, which occurs on a short timescale. Note that the distribution extends somewhat higher in energy than that of the incident beam, suggesting that some of the incident electronic energy has been converted to kinetic energy. The main text explores this suggestion further.

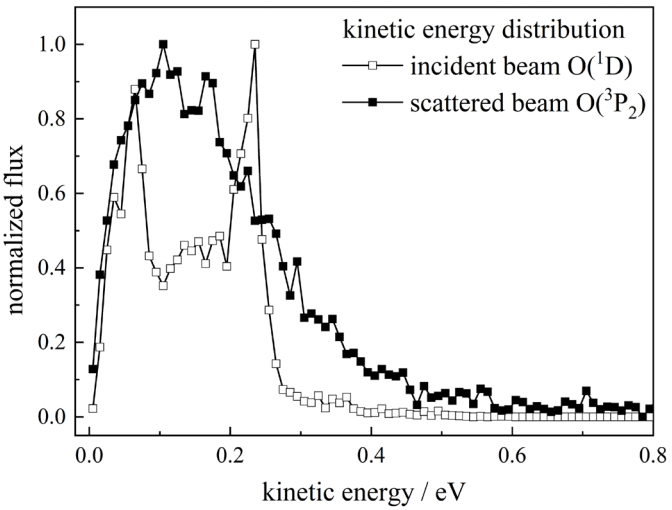

Figure S7. The kinetic energy distribution of incident $O(^1D)$ atoms obtained from the 157 nm photolysis of CO_2 is shown as open markers. The resulting kinetic energy distribution of $O(^3P_2)$ state atoms scattered from HOPG at normal incidence angle is shown with filled markers.

For $t_{\text{arrive}} = t_{\text{depart}}$ times between 30 μs and 90 μs, the contribution of the minor $O(^3P) \rightarrow O(^3P)$ channel is well resolved from the dominant $O(^1D) \rightarrow O(^3P)$ channel. The kinetic energy distributions of incident and scattered $O(^3P_2)$ atoms that were assigned to this range of t_{arrive} or

t_{depart}, respectively, are plotted in Fig. S8. The average incidence kinetic energy $\langle E_{\mathrm{i}} \rangle = 1.28$ eV and the average scattering kinetic energy $\langle E_{\mathrm{s}} \rangle = 0.525$ eV. The incidence energy distribution has a width of ~1 eV. We did not attempt to assign scattered atoms to more precise E_{i} intervals because the signal level in this scattering channel was low, due to the small amount of $\mathrm{O}(^3\mathrm{P})$ produced by this beam source.

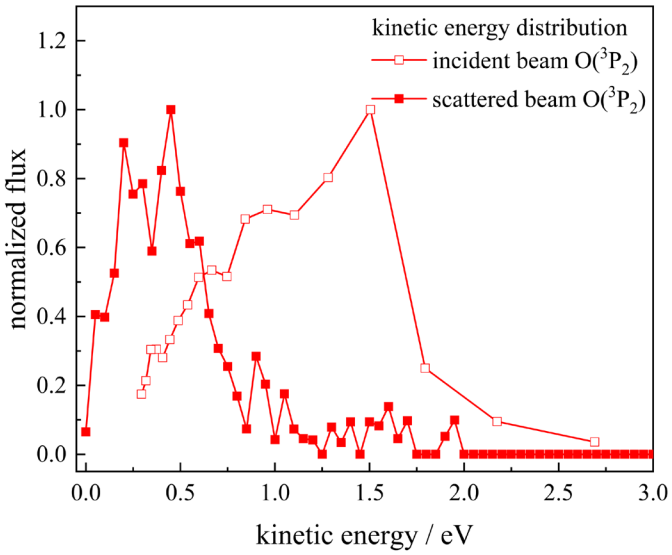

Figure S8. Kinetic energy distribution of incident (open squares) and scattered (filled squares) $O(^3P_2)$ atoms that were assigned to $t_{\mathrm{arrive}} = t_{\mathrm{depart}}$ times between 30 μs and 90 μs (corresponding to the early peak in Fig. 3b of the main text). These distributions arise from $\mathrm{O}(^3\mathrm{P}) \rightarrow \mathrm{O}(^3\mathrm{P})$ scattering of the incident atoms from Channel II of the CO_2 photolysis beam.

5.5.2.3 Theoretical results for O(^{3}P) scattering

MD trajectories for incident O atoms in the ^{3}P ground state are calculated using two different PESs: the triplet and adiabatic PESs. For all trajectories, the initial kinetic energy is set at 0.34 eV and three initial polar incidence angles ($\theta_i = 0°$, $-10°$, and $-20°$) are chosen in order to compare with experimental results, while the initial azimuthal angle is generated randomly ranging from 0 to 360 degrees. The surface temperature is set at 300 K. Because in the experiment, only in-plane scattering is observed, we also choose in-plane trajectories to make meaningful

comparisons. Considering that strictly in-plane trajectories represent only a small fraction of the total trajectories and a very large number of total trajectories are needed to generate enough in-plane trajectories to get converged statistical results, trajectories within ±20 degrees of acceptance angle are counted as in-plane trajectories.

The angular and kinetic energy distributions obtained from the scattering trajectories on the two PESs are compared with the experimental results in Fig. S9. (The $\theta_i = -20°$ data is the same as that shown in Fig. 2(a)–(c) of the main text.) Both PESs lead to similar scattering kinetic energy distributions, but to qualitatively different angular distributions and sticking probabilities (see below). The triplet PES resulted in an angular distribution peaked near the specular angle, whereas the adiabatic PES resulted in a bimodal distribution with a second peak at much larger angles. When $\theta_i \neq 0$, backward scattering (toward the incidence direction) is seen. To gain insight into the origin of the backward scattering, the position of the turning point of the scattered trajectories on the adiabatic PES, which is defined as the point when the normal component of the O atom velocity changes direction, is computed and plotted in Fig. S10. It was found that most in-plane specular scattering takes place at the top site (red crosses in Fig. S10) and the larger angle scattering occurs at the hollow site (blue crosses in Fig. S10). This can be understood from the two-dimensional cuts of the triplet and adiabatic PESs along the *xz* and *yz* planes with all the other dimensions relaxed, as shown in Fig. S11. Comparing with the triplet PES, the adiabatic PES is much more attractive and corrugated. The corresponding PES near the top site is relatively flat, leading largely to specular scattering. On the other hand, the strong corrugation near the hollow site results in backward scattering.

Although the predicted back scattering peak occurs near the detector cutoff, we would still expect to be able to experimentally observe indications of this peak at angles between −20 to −50°

when $\theta_i = -20°$ (upper right panel of Fig. S9). The absence of any indication of such a peak in the measured angular distribution leads us to conclude that the experiment is more consistent with the simulations performed on the triplet PES, which suggests that triplet → singlet → triplet conversion *does not* readily occur at the surface during direct scattering trajectories at incidence energies around 0.34 eV.

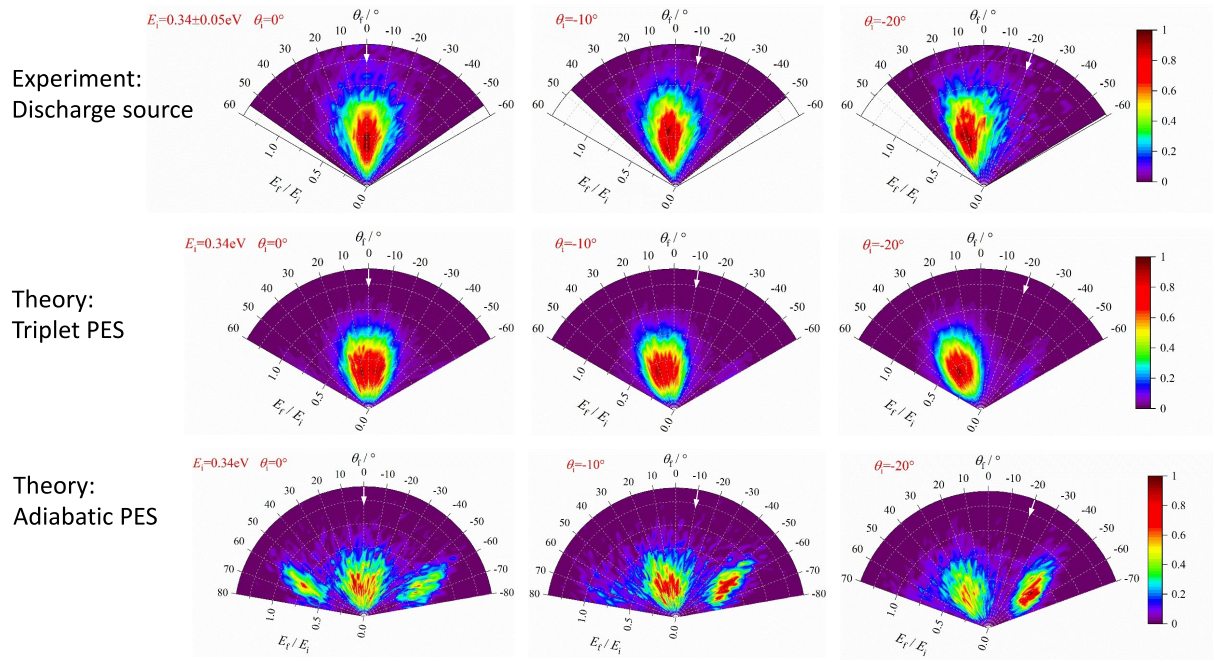

Figure S9: Comparison of Experiment to MD simulations on two PESs. The experimental kinetic energy and angular distribution (top row) obtained for O atoms from the O_2 discharge source after scattering from HOPG. Scattered atoms were detected in the $^3P_2$ state. The plotted distribution corresponds to those atoms assigned to an incidence energy range of $E_i = 0.34 \pm 0.05$ eV via the incoming/outgoing correlation method (Section 1.2). The results of MD simulations on the triplet PES (middle row) and adiabatic PES (bottom row) are shown for comparison. The simulations were performed at an incidence energy of precisely 0.34 eV. The radial coordinate corresponds to the final kinetic energy divided by the nominal incidence energy (0.34 eV). The left, center, and right columns correspond to incidence angles of 0°, −10°, and −20°, respectively. The incidence angle is indicated by a white arrow for clarity.

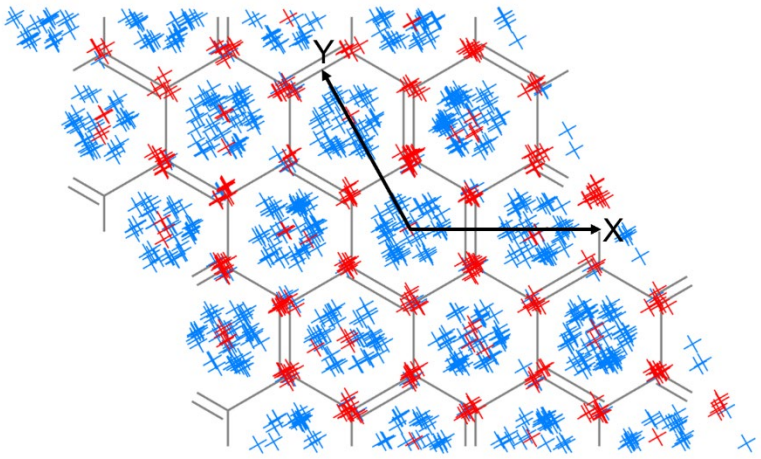

Figure S10. Turning point distribution of in-plane scattering trajectories on the adiabatic PES for $E_i = 0.34$ eV. The red and blue crosses represent trajectories with near-specular and non-specular scattering angles, which are concentrated at the top and hollow sites, respectively. The x and y coordinates are defined by the vectors in the surface plane and z is the coordinate perpendicular to the surface plane.

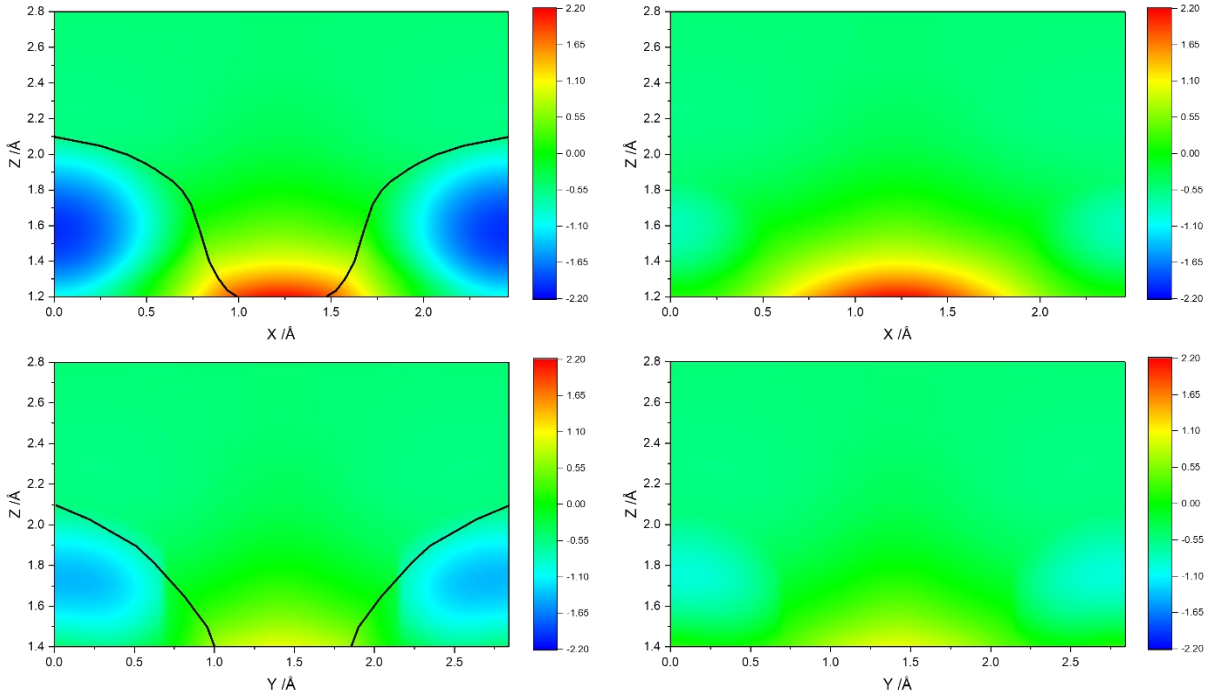

Figure S11. Two-dimensional cuts of the adiabatic PES (left panels) and triplet PES (right panels) through the xz and yz planes (as defined in Figure S10). The triplet-singlet crossing seam is displayed in the left panels as black curves. The energy, in eV, is relative to the triplet asymptote.

5.5.2.4 Experimentally determined sticking probabilities

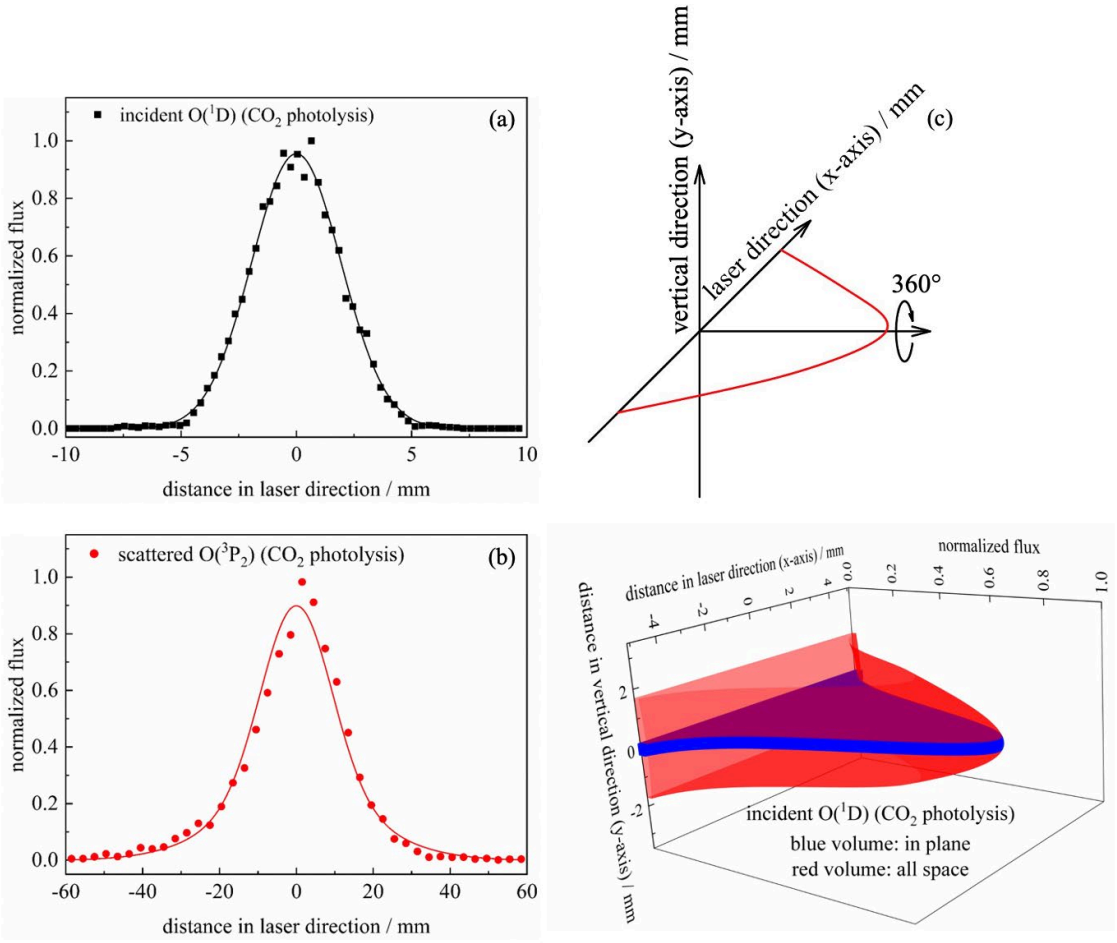

Figure S12. Panels (a) and (b) show the spatial flux distribution in the laser direction for scattered $O(^3P_2)$ and incident $O(^1D)$ from the CO_2 photolysis source. Panel (c) shows the axis system, where the *x*-axis is laser direction, the *y*-axis corresponds to vertical direction, and the *z*-axis is along the surface normal direction. Panel (d) is the incident O^1D spatial distribution from the CO_2 photolysis source in 3D space.

We obtained the sticking coefficients from experiment by measuring the ratio of the integrated flux of incident and scattered O atoms. Here, we describe the procedure in detail for the CO_2 photolysis source, used to obtain the $O(^1D)$ sticking coefficient. The sticking coefficient for $O(^3P)$ was obtained in a similar manner using the O_2 discharge source. For the CO_2 photolysis source, we measured the incident $O(^3P_2)$ flux and scattered $O(^3P_2)$ flux at the same time, while scanning the probe laser focus along the laser propagation direction. The REMPI scheme, laser

power, and nozzle conditions were hence identical for the two measurements. The ratio $O(^1D):O(^3P_2) = 94\%:4.2\%$ obtained from the 157 nm photolysis of CO_2 is taken directly from the literature [237-238]. The incident $O(^1D)$ density is equal to the incident $O(^3P_2)$ density multiplied by this ratio.

The experiment measures only the in-plane component of the incident and scattered flux via slice imaging (Figs. S12(a) and S12(b)). These distributions were fitted with Gaussian functions, which can be expressed (in arbitrary units) as:

$$f_{\text{i,in plane}}(x) = 0.95 \cdot \exp\left(-\frac{x^2}{2\cdot(1.93\text{ mm})^2}\right) \tag{S8}$$

$$f_{\text{scat,in plane}}(x) = 0.22 \cdot \exp\left(-\frac{x^2}{2\cdot(18.74\text{ mm})^2}\right) + 0.68 \cdot \exp\left(-\frac{x^2}{2\cdot(9.07\text{ mm})^2}\right) \tag{S9}$$

The vertical height of the scattered in-plane O-atom signal is determined by the focal waist of the laser. We assume a height of 0.384 mm, which corresponds to an acceptance angle about $\pm 1°$ relative to the scattering plane. (Note that the final result is not sensitive to the accuracy of this value due to cancellation of error when taking the ratio between the incident and scattered flux.) The volume of the resulting truncated Gaussian function is calculated from:

$$V = 2\pi a {\sigma_a}^2 \left[\Phi\left(\frac{y_0}{\sigma_a}\right) - \Phi\left(-\frac{y_0}{\sigma_a}\right)\right] \tag{S10}$$

where y_0 is the vertical cutoff distance, $\Phi(x) = \frac{1}{\sqrt{2\pi}}\int_{-\infty}^{x} \exp\left(-\frac{t^2}{2}\right) \mathrm{d}t$ is the cumulative distribution function of the standard normal distribution, and σ_a is the Gaussian width parameter.

In order to estimate the scattering probability in three-dimensional space $p_{\text{scat,3D}}$, we assumed that the distribution has cylindrical symmetry about the surface normal and rotated the fitted in-plane distribution over 360° about the surface normal. Such a rotated Gaussian function is given in the coordinate system of Fig. S12(c) by:

$$g(x,y) = a\exp\left(-\frac{x^2+y^2}{2{\sigma_a}^2}\right) \tag{S11}$$

We used a rectangular orifice ($x \times y$ = 3 mm × 1 mm) in the experiment such that the incident beam is truncated along the vertical direction. We expect the width of the incident atomic beam to be three times wider along the *x*-direction than along the *y*-direction. The incident $O(^1D)$ spatial distribution of CO_2 photolysis source in 3D space is shown in Fig. S12(d). The volume of integration corresponding to the in-plane scattered O atom flux (laser focus size $y = \pm 0.192$ mm) is shaded blue, and the volume of integration corresponding to the overall flux is shaded red. The distance along the laser direction (*x* axis) is about ± 5.1 mm, so the distance along the vertical direction (*y* axis) is about $\pm\frac{5.1}{3}$ mm, and the volume of integration (shaded red), in arbitrary units, is

$$V_{\mathrm{i,3D}} = 2\pi \cdot 0.95 \cdot 1.93^2 \cdot \left[\Phi\left(\frac{\frac{5.1}{3}}{1.93}\right) - \Phi\left(-\frac{\frac{5.1}{3}}{1.93}\right)\right] = 13.82 \tag{S12}$$

The laser focus size is ± 0.192 mm, so the volume of integration corresponding to the in-plane flux (shaded blue), in arbitrary units, is

$$V_{\mathrm{i,in\ plane}} = 2\pi \cdot 0.95 \cdot 1.93^2 \cdot \left[\Phi\left(\frac{0.192}{1.93}\right) - \Phi\left(-\frac{0.192}{1.93}\right)\right] = 1.76 \tag{S13}$$

The integrated flux in 3D space can be obtained by correcting the in-plane flux component by the ratio between the volume of integration for in plane signal and for 3D signal:

$$\mathrm{flux_{3D}} = \left(\int f_{\mathrm{i,in\ plane}}(x)\mathrm{d}x\right)\frac{\mathrm{V_{3D}}}{\mathrm{V_{in\ plane}}} \tag{S14}$$

The scattering probability is equal to

$$p_{\mathrm{scat,3D}} = \frac{flux_{\mathrm{scat,3D}}}{flux_{\mathrm{i,3D}}} = \frac{\left(\int f_{\mathrm{scat,in\ plane}}(x)\mathrm{d}x\right)\frac{\mathrm{V_{scat,3D}}}{\mathrm{V_{scat,in\ plane}}}}{\left(\int f_{\mathrm{i,in\ plane}}(x)\mathrm{d}x\right)\frac{\mathrm{V_{i,\ 3D}}}{\mathrm{V_{i,\ in\ plane}}}} \tag{S15}$$

The sticking coefficient is calculated from:

$$s_0 = 1 - p_{\mathrm{scat,3D}} \tag{S16}$$

In experiments using the discharge source, both the in-plane incident and scattered $O(^3P)$ fluxes are measured directly. The sticking coefficient for $O(^3P)$ is then determined from Eqns. S15 and S16 in a manner similar to that described above for $O(^1D)$. The results are shown in Fig. 4 of the main text.

5.5.2.5 Theoretically determined sticking probabilities

The MD simulations also allow a theoretical determination of the $O(^3P)$ sticking probability. On the spin-relaxed adiabatic PES, there was a very high probability of sticking—in about 93% of trajectories, the O atom was still less than 2.0 Angstroms from the surface after 50 ps. Due to the much weaker binding on the triplet surface, the sticking probability was much lower on this surface (about 68% after 50 ps). We note that due to the finite number of atoms in the model graphene, the dissipation of energy is not expected to be complete in the simulation.

The $O(^1D)$ simulation with $\tau_{S-T} = 100$ fs yielded a sticking probability of 0.997 at an incidence energy of 0.23 eV. This value is much higher than the experimental value of ~0.7 ± 0.1. Error might arise due to the uncertainties in electronic structure calculations, in particular the adsorption well depth and the crossing seam between the two states. Such errors are not unexpected with DFT as evidenced by its inability to reproduce the $O(^1D)$-$O(^3P)$ energy gap. Another type of error might arise if electronically excited states, which are not considered here, participate in the dynamics due to the coupling of O-atom orbitals to the conduction band of the graphene layer. For example, if the dynamics can take place on electronically excited singlet states, this could shift the location of the intersection with the triplet state, possibly leading to an effective broadening of the seam of intersection. In addition, the *ad hoc* assumption used to treat the spin flipping dynamics and the limited size of the graphene model may also be responsible to the disagreement.

5.5.2.6 Theoretical simulations of $O(^1D) \rightarrow O(^3P)$ spin-flipping dynamics

We performed an MD simulation to consider spin non-conserving $O(^1D) \rightarrow O(^3P)$ trajectories, as described in the main text. Due to intrinsic errors of the DFT calculations, the energy of gas-phase $O(^1D)$ is only about 1.3 eV higher than that of $O(^3P)$. In order to match the experimental energy gap between singlet and triplet O, which is about 2 eV, the singlet PES was shifted upwards by 0.7 eV in our calculations. We used three different values of τ_{S-T} (0, 50 fs, and 100 fs) and performed simulations with 10,000, 50,000, and 700,000 trajectories, respectively. Figure S13 shows the energy difference between the singlet and triplet PESs for points along several scattering trajectories with the spin-flip delay τ_{S-T} set to 100 fs. The inset shows the results for one representative trajectory, plotted alongside the z-distance of the O atom above the surface. The O atom reaches the seam of intersection ($\sim$2 Å above the surface) about 200 fs after the start of the simulation. For the next 100 fs, the O atom was constrained to the singlet PES, no matter whether it reaches the intersection or not. After that, at about 400 fs, the O atom jumps to the triplet state once it crosses the seam, leading eventually to desorption from the surface as evidenced by the increasing z value. The kinetic energy distributions obtained at different τ_{S-T} delays are described in the main text.

Admittedly, this *ad hoc* model is not expected to quantitatively reproduce the experimental finding. Rather, it is used to test the viability of the nonadiabatic spin-flip mechanism in this system. The results underscore competition of two important time scales, namely the rate of energy dissipation and the rate of nonadiabatic transitions. The former is controlled by the interaction of the impinging oxygen atom with the HOPG, while the latter by the spin-orbit coupling and the velocity of the O atom passing through the seam. The current model is insufficient to provide quantitative information on either rate; more sophisticated theory is needed.

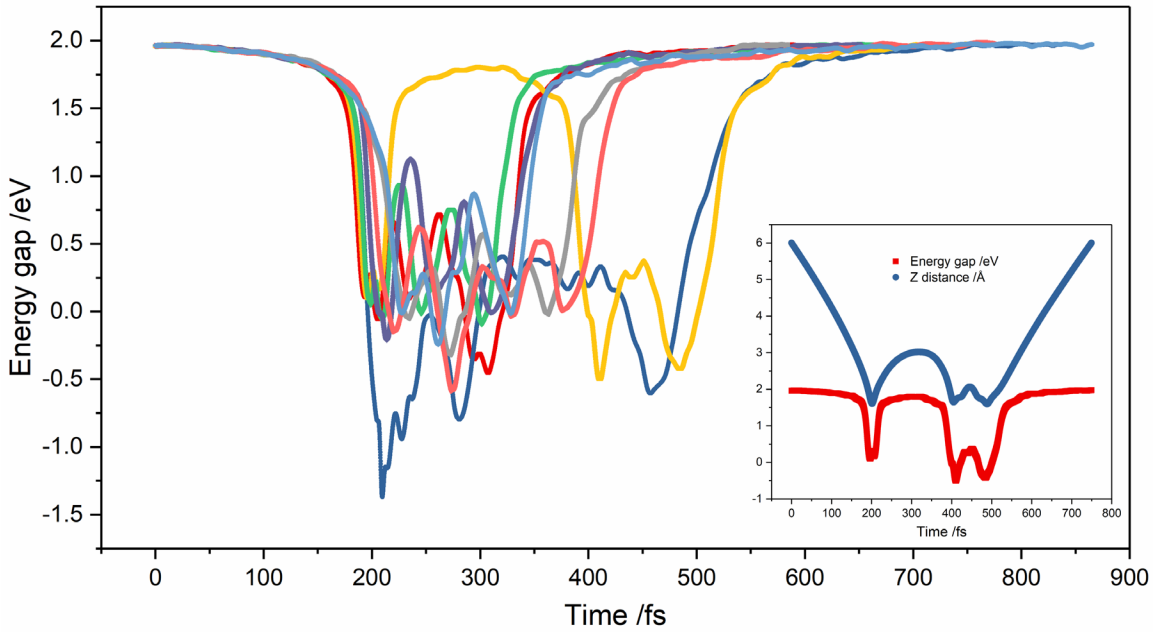

Figure S13. Molecular Dynamics including spin flipping. The energy difference between the singlet and triplet PESs is plotted for several scattering trajectories as a function of time. The $O(^1D) \rightarrow O(^3P)$ spin-flip delay τ_{S-T} (see main text) was set to 100 fs. A positive energy gap corresponds to a configuration where the triplet PES is more stable and a negative energy gap corresponds to a configuration where the singlet PES is more stable. The seam of intersection is crossed when the energy gap changes sign. The inset plots the energy gap (red) and z-distance (blue) simultaneously for a representative trajectory.

CHAPTER 6

H ATOM COLLISIONS WITH A SEMICONDUCTOR EFFICIENTLY PROMOTE ELECTRONS TO THE CONDUCTION BAND

The materials discussed in this chapter is based on the publication: K. Krüger, Y. Wang, S. Tödter, F. Debbeler, A. Matveenko, N. Hertl, X. Zhou, B. Jiang, H. Guo, A. M. Wodtke, O. Bünermann, Nat. Chem., accepted, H atom collisions with a semiconductor efficiently promote electrons from the valence to the conduction band.

6.1 Introduction

Atoms and molecules colliding at solid surfaces create time-varying electric fields that, due to their finite masses and associated low speeds, represent frequencies typically $\leq 10^{13}$ Hz, whereas much lighter electrons in solids oscillate at frequencies one to two orders of magnitude higher than this. This separation of time-scales is used to justify the Born-Oppenheimer approximation (BOA), the bedrock of computational surface chemistry,[239] where electronic quantum states rapidly adjust to the motion of nuclei. Inelastic H atom surface scattering experiments have provided excellent benchmarks against which theoretical methods can and have been tested and proven.[240] Using this approach, the BOA has been shown to be justified for H atom scattering from Xe, where molecular dynamics simulations using a full-dimensional potential energy surface quantitatively reproduced energy-losses measured in high-resolution scattering experiments.[241] The validity of the BOA in this case is not surprising since the lowest energy electronic excitations in Xe exceeded the energies of that work. Similar energy-loss measurements from experiments scattering H and D from the semi-metal graphene, where low energy electron-hole pair (EHP) excitations are possible,

also showed no signs of BOA failure.[242-244] Despite these successes, there are reasons to question the BOA's validity. For example, energetic H atoms colliding at metal surfaces always excite EHPs;[10, 245] albeit, theory could successfully treat this with a weak-coupling "electronic friction" approximation suggesting BOA failure is not severe and can be accounted for in a perturbative fashion.[20, 246]

Experiments with semiconductors present an opportunity to make predictions from our current understanding about a fundamentally different class of solids. This is true if semiconductors behave in some hybrid fashion, reflecting some intermediate to insulators and metals. But let us consider semiconductors from the point of view of another kind of time varying electric field. We know visible light with electric fields oscillating at ~$10^{14\text{-}15}$ Hz efficiently excites electrons from the valence band (VB) to the conduction band (CB), forming the basis for a large fraction of optical science and technology. This raises the question: if collisions of atoms and molecules with semi- conductors could produce time varying electric fields oscillating at similar frequencies, would they not also excite VB electrons to the CB and might this not provide important new avenues of research with promise of new technology? If we were to adopt the physical picture derived from our study of metals, where electronic friction describes BOA failure, the answer to this question would certainly be "no" or more precisely "only weakly" as electronic friction theories lead to hot EHP distributions that still favor low energy excitation near the Fermi level.[246] Unfortunately, scattering experiments with semiconductors that test the validity of the BOA are rare. Transient currents were observed when Xe atoms with energies between 3 and 10 eV were scattered from surfaces of semiconductors;[247-249] however, this resulted from the creation of a local hot spot where initial phonon excitation subsequently transferred energy to EHPs. While these experiments provide us clear evidence of BOA failure in a semiconductor, we can gain only

little insight into the dynamics of the atom-surface collision. In fact, an electronically adiabatic model could describe the energy-loss of scattered Xe atoms.

In this work, we produce H atoms whose speeds are high enough to test the limits of the BOA directly by investigating the characteristics of their collisions with a semiconductor surface and measured H atom energy-loss spectra and angular distributions reveal the excitations appearing in the solid on the sub-ps time scale. We find that, not only is VB-CB excitation possible, at sufficiently high energies it dominates the energy transfer dynamics, showing that new physical mechanisms are at play. Specifically, we present translational energy-loss measurements on energetic H atoms scattered from a reconstructed Ge(111)c(2×8) surface along with first principles electronically adiabatic molecular dynamics (MD) simulations, performed with a newly developed full- dimensional neural network potential energy surface (NN-PES). When incidence energies are below the bandgap, only one scattering channel arises with small energy-losses nearly identical to those seen in the MD simulations. These exhibit collision dynamics similar to those seen in H scattering from Xe. Surprisingly, at higher incidence energies, a second channel appears whose energy-loss onset is coincident with the semiconductor bandgap. This channel is absent in the MD simulations with and without electronic friction. The importance of this channel increases rapidly with H atom velocity — a signature of BOA failure — and accounts for ~90% probability at the highest H atom incidence energies of this work.

6.2 Results

Fig. 1 shows experimental translational energy-loss distributions for H atoms scattered from Ge(111)c(2×8)[250] at incidence energies E_i above and below the 0.49 eV surface bandgap.[251] Also shown are the predictions of the electronically adiabatic MD trajectory calculations. Below the bandgap (Fig. 1A) only a single feature appears in the energy-loss distribution. The MD

simulations reproduce the experimental result extremely well. Molecular dynamics with electronic friction[51] at the level of local density friction approximation (LDFA)[53] fail to describe the energy loss distributions—see Fig. E1. Analysis of adiabatic MD trajectories shows that H atoms interact with the Ge surface for only a few fs and that energy exchange is limited. Figs. 1B-D show energy loss distributions for three values of E_i larger than the surface bandgap—in all three cases, the distributions are bimodal and the MD trajectories reproduce only the feature seen at low values of energy-loss. Hereafter, we refer to this feature as the adiabatic channel. The second feature appearing at higher energy-losses is absent in the adiabatic MD simulations, strongly suggesting that this channel involves conversion of H atom translational energy to electronic excitation of the Ge solid. This idea is further supported by the observation that the energy-loss onset of this feature is coincident (within experimental uncertainty) with the Ge surface bandgap of 0.49 eV at all values of Ei. Furthermore, as expected for a channel involving BOA failure, this channel is strongly pro- moted by incidence translational energy, becoming about 90% of the observed scattering at the highest value of E_i = 6.17 eV. For these reasons, we assign the high energy-loss feature to an electronically non-adiabatic process where the collision of the H atom at the surface promotes an electron from the VB to the CB of the Ge surface. We refer to this channel hereafter as the VB-CB channel.

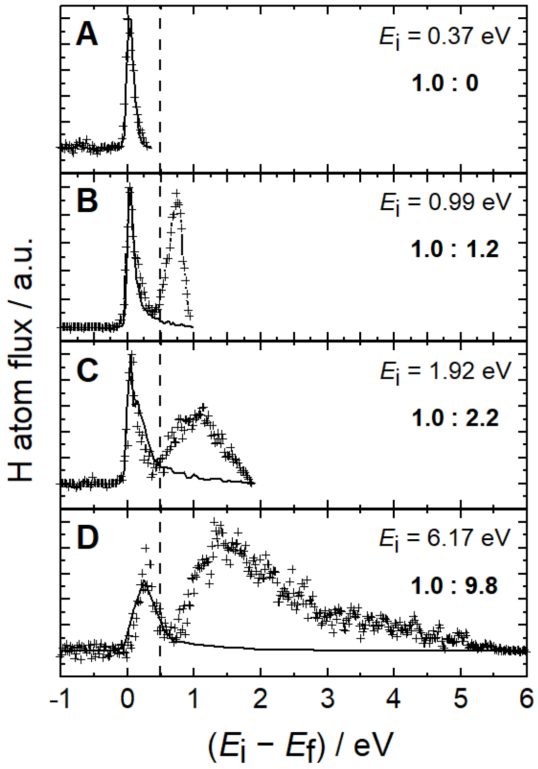

Fig. 1. Translational energy-loss distributions for H atoms scattered from Ge(111)c(2×8). The incident H atoms travel along the [$\bar{1}$10] surface direction, while the polar incidence and scattering angles θ_i and θ_f, respectively, were both 45° with respect to the surface normal. The surface temperature TS was 300 K. Experimental data (+) and the results of adiabatic molecular dynamics simulations (solid lines) for four H atom translational incidence energies are shown: E_i = 0.37 eV (A), 0.99 eV (B), 1.92 eV (C), and 6.17 eV (D). The band gap of the surface is 0.49 eV and indicated by the vertical dashed line. The experimentally obtained ratio of the adiabatic to the VB-CB channel appears in each panel. All experimental curves are normalized to the peak intensity. The MD curves are scaled to fit the adiabatic channel.

Fig. 2 shows differential properties from both experiment and theory for H atoms incident at three angles θ_i and at E_i = 0.99 eV. Here, polar plots display the final translational energy E_f as a function of final scattering angle θ_f. A white dashed line shows the expected energy loss for excitation of an electron from the VB maximum to the CB minimum, which demarcates the adiabatic from the VB-CB channel. Experiment shows that the VB-CB channel exhibits a much narrower angular distribution (Table 1) than the adiabatic channel at all three incidence angles.

The MD simulations yield similar differential scattering maps as seen in experiment for the adiabatic channel only. The energy loss agrees with experiment and even the experimentally observed dependency of the angular distribution on θ_i is reproduced. The VB-CB channel is absent in the MD simulations.

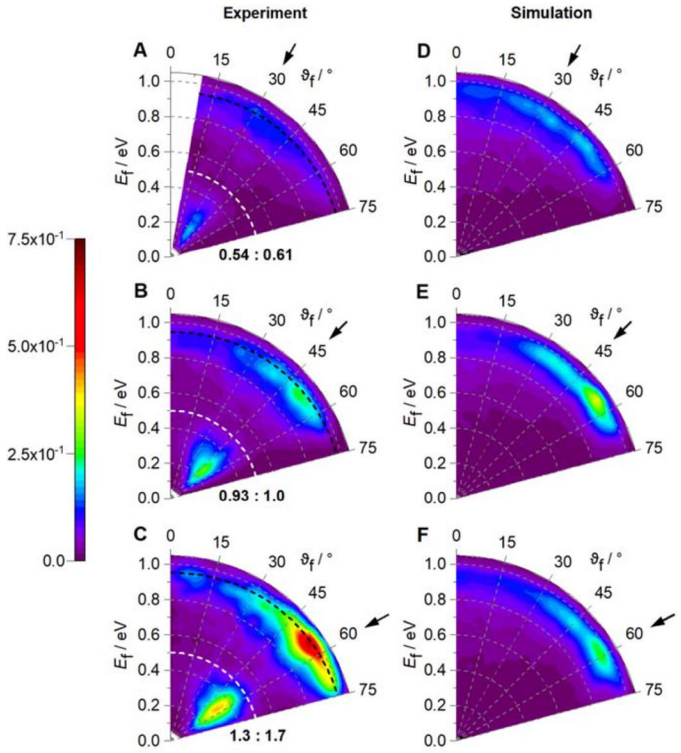

Fig. 2. Incidence angle dependence of H atoms scattered from Ge(111)c(2×8). Energy resolved angular distributions derived from in-plane scattering flux are shown for three incidence angles, θ_i = 30°, 45°, 60° and an incidence translational energy E_i = 0. 99 eV. The surface temperature was T_S = 300 K. Experimental results (A to C) are com- pared to MD simulations (D to F). The adiabatic and the VB-CB channels both exhibit maximum scattering flux near the specular scattering angle (arrows). The MD simulations reproduce the behavior of the adiabatic channel only. To construct the experimental plots, data was recorded in 5° increments from θ_f = 0° to 75°. All six polar plots are normalized to the incident H atom flux. The MD simulations are scaled to experiment such that at θ_i = 45°, the integrated adiabatic channels are equal in both. The experimentally obtained ratio of the VB-CB channel to the adiabatic channel appears in each panel. The black dashed lines represent the final energy predicted by a line-of-centers binary collision model: $E_f = E_i\{1 - \cos^2[(\theta_i + \theta_f) / 2] \times [1 - (m_H - m_{Ge})^2 / (m_H + m_{Ge})^2]\}$. The white dashed lines show the expected value of E_f for excitation of an electron from the VB maximum to the CB minimum.

Fig. 3 shows polar plot representations similar to Fig. 2 emphasizing the incidence energy dependence of the scattering. As before, the experimental results show bimodal scattering distributions with two well-resolved channels separated in energy space by the bandgap energy, marked as a white dashed line. The angular distributions of both channels broaden between E_i = 0.99 eV and 1.92 eV; but the VB-CB channel broadens significantly more as it is narrower at E_i = 0.99 eV. The adiabatic MD simulations (Fig. 3C & 3D) reproduce this effect for the adiabatic channel.

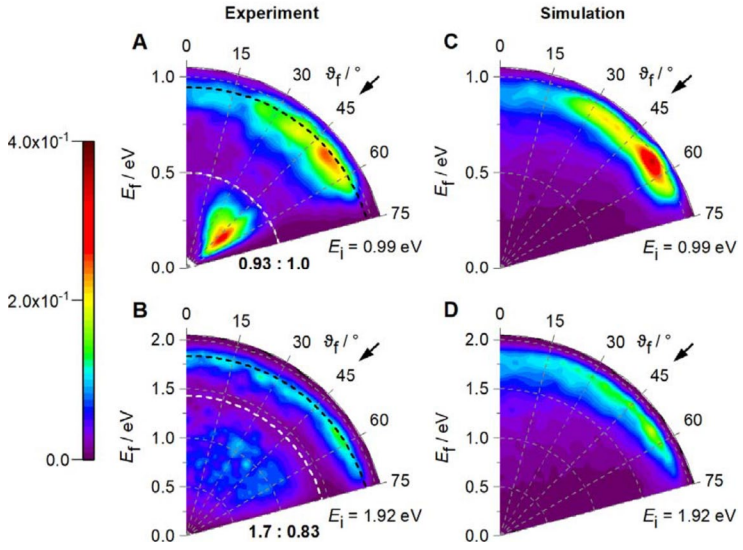

Fig. 3. Incidence energy dependence of H atoms scattered from Ge(111)c(2×8). As in Fig. 2 unless stated otherwise. Two incidence translational energies E_i = 0. 99 eV (A & C) and 1. 92 eV (B & D) are shown. Experimental results (A & B) are compared to MD simulations (C & D). The incidence angle is θ_i = 45°.

The average energy losses derived from the experiments are summarized in Table 2. Notice that for the adiabatic channel, the average energy transferred to the surface $\langle E_i - E_f \rangle$ is a small and nearly constant fraction (10 ± 5%) of E_i. The VB-CB channel behaves differently—the fraction of incidence energy transferred to the solid goes up dramatically as E_i is reduced. This is an influence of the surface bandgap, where the absolute of energy lost must exceed 0.49 eV, regardless of E_i.

Hence at lower values of E_i, the fractional energy loss must sharply increase. Also notice that the average energy lost decreases only slightly with increasing θ_i for both channels.

Table 1: Angular full width at half maximum for the experimental angular distributions of this work.

E_i	VB −CB			Adiabatic		
	$\theta_i = 30°$	$\theta_i = 45°$	$\theta_i = 60°$	$\theta_i = 30°$	$\theta_i = 45°$	$\theta_i = 60°$
0.99 eV	24°	31°	24°	> 56°	44°	34°
1.92 eV	–	> 70°	–	–	> 73°	–

Table 2: Average energy-loss in experimentally obtained specular ($\theta_i = \theta_f$) H atom scattering. Values in parentheses were computed from adiabatic MD trajectories.

E_i	θ_i	VB − CB		Adiabatic	
		$\langle E_i - E_f \rangle$	$\frac{\langle E_i - E_f \rangle}{E_i} \times 100$	$\langle E_i - E_f \rangle$	$\frac{\langle E_i - E_f \rangle}{E_i} \times 100$
0.37 eV	45°	–	–	0.05 eV	14% (13%)
0.99 eV	30°	0.75 eV	75%	0.15 eV	15% (17%)
	45°	0.71 eV	72%	0.13 eV	13% (12%)
	60°	0.69 eV	70%	0.10 eV	10% (8.1%)
1.92 eV	45°	1.12 eV	58%	0.20 eV	10% (14%)
6.17 eV	45°	2.28 eV	37%	0.32 eV	5.2% (7.7%)

6.3 Discussion

We first highlight some of the key observations just presented and their implications. First, Fig. 2 shows clearly that the most probable value of θ_f depends on the chosen value of θ_i, proving the scattered atoms did not thermalize with the solid—thermalization occurs on the ps timescale. Thus we conclude that the scattered atoms in both channels experience a sub-picosecond interaction time with the surface. Second, there is evidence of sticking, despite the fact that integrated scattering probabilities like sticking probabilities cannot be easily obtained from in-plane differential scattering measurements, since the fraction of incident atoms that scatter out of the detection plane may also depend on incidence conditions and branching channel. We can

nevertheless integrate the observed scattering flux over E_f and θ_f. These integrals appear next to each differential scattering diagram in Figs. 2 & 3 divided into the relative contributions of the two scattering channels. There is an overall loss of signal between E_i = 1.92 eV and 0.99 eV. If we were to assume the out-of-plane scattering fraction were independent of E_i, we would conclude that the sticking prob- ability decreases with increasing incidence energy. A similar trend is seen in the MD simulations. Also notice that the branching ratios shown in Figs. 3A & B are consistent with those of Figs. 1B & C, which represent the branching between the two scattering channels detected at $\theta_f = 45°$ only. This agreement suggests that the branching see in Fig. 1D (E_i = 1.92 eV) is representative of scattering angles.

The major outcome of this work is the observation that an H atom scattering from a semiconductor may experience one or the other of two types of interactions, either a mechanical interaction well described within the BOA or a strong non-adiabatic interaction capable of promoting an electron from the VB to the CB. We emphasize that while there are similarities with past work, the behavior seen here is qualitatively different from previous observations involving insulators, metals or semi-metals. For example, the adiabatic channel seen in Figs. 1-3 exhibits marked similarities to H atom scattering from insulating Xe; however, that system exhibited no BOA failure whatsoever. Conversely, H scattering trajectories describing collisions with metals simultaneously excite both phonons and EHPs,[10, 20, 245-246] the two excitations being inextricably linked to one another. The question remains, what gives rise to the branching between the two channels in the H/Ge system?

The fact that H scattering from Ge exhibits branching behavior between two distinct dynamical channels is consistent with a two-state picture involving the VB and the CB. We envision that the H atom proceeds initially along an electronic state associated with the VB and

subsequently encounters a seam of crossing associated with electronic excitation of the CB. At low incidence energies, the crossing requires specific approach, but at higher energies, other regions of the seam become accessible with different steric restrictions.

Evidence supporting this picture can be found in observations of this work, especially Fig. 2. Notice that the VB-CB channel exhibits a narrow angular distribution, peaking near the specular scattering angle (arrows in Fig. 2). This shows that there is no preference for loss of incidence energy parallel or perpendicular to the surface when promoting an electron from the VB to the CB. A narrow angular distribution is typical of scattering influenced by directional forces associated with atomic orbitals with preferred orientations, consistent with the suggested mechanism of a curve crossing, where H atom collisions must occur at specific surface sites (Ge atoms) and with specific approach geometries. Fig. 3 shows that at higher energy these steric restrictions appear to be less severe; consequently, the VB-CB scattering angular distribution broadens.

Contrasting this behavior, the adiabatic channel exhibits a markedly broader angular distribution even at low incidence energy. This indicates a large corrugation of the potential energy surface experienced by the atoms passing through the adiabatic channel. Despite the many final scattering angles, the energy loss follows a hard-sphere line-of-centers (LOC) binary collision model (black dashed line). This indicates that the H atom scattered through the adiabatic channel is experiencing binary collisions with many impact parameters, not surprising due to the complex surface structure of Ge(111)c(2×8) surface if the H atoms scattering through the adiabatic channel sample a large fraction of the surface unit cell.

We hasten to point out that bimodal energy-loss distributions are seen for H atom scattering experiments using graphene grown on Pt(111);[242-244] however, this behavior is due to a chemisorption barrier that does not exist for the H/Ge system. H scattering from a graphene layer

involves trajectories that either fail or succeed in surmounting the chemisorption barrier. H atoms reflected from the barrier experience weak van der Waals interactions with little energy transferred, while H atoms surmounting the barrier couple strongly to in-plane phonons of the graphene layer.[242] Similar dynamics are not possible for the H/Ge system; so, the bimodal energy distributions must arise by another mechanism.

While it is common knowledge that absorption of photons in the bulk of a semiconductor excites electrons from the VB to the CB, this work shows that a colliding atom may efficiently promote electrons in a similar way in a purely surface specific process. The probability to convert translational energy of the H atom to electronic excitation of the solid dramatically increases with incidence energy, as does the average excitation energy. The large excitation probability as well as the large energy-loss appears inconsistent with electronic friction theories; hence, this work stands as a challenge for new theories of electronically non-adiabatic surface chemistry. Beyond this, the observation that VB-CB electronic transitions dominate the dynamics in collisions of a simple atom with a semiconductor may open new horizons for research into non-adiabatic effects in surface chemistry and chemical sensors.

6.4 Methods

The experimental setup is described in detail in refs. [240, 252]. Briefly, UV ($\lambda_{photolysis}$ = 248.35 nm) or VUV ($\lambda_{photolysis}$ =121.4 nm) photodissociation of a supersonic molecular beam of hydrogen iodide produces a H atom beam with translational energies of E_i = 0.37, 0.99, 1.92 or 6.17 eV that then passes two differential pumping chambers to enter an UHV scattering chamber before colliding with a Germanium crystal. The Ge sample is held on a 5-axis manipulator allowing the variation of the polar incidence angle θ_i with respect to the surface normal. The scattered H atoms are excited to a long-lived Rydberg state just below the ionization limit[253] and fly 250 mm before

they are field-ionized and detected by a multichannel plate (MCP) assembly. A multichannel scaler records the arrival time to obtain the time-of-flight (TOF) distributions, which we convert to energy spectra applying the appropriate Jacobians. The detector is rotatable in the plane defined by the incident H atom beam and the surface normal allowing TOF distributions to be obtained at various final scattering angles θ_f. The Ge(111) surface was cleaned with cycles of Ar^+ ion sputtering and annealing to ~ 670°C. Auger electron spectroscopy (AES) and low-energy electron diffraction (LEED) validated the cleanliness and c(2×8) structure of the surface.

To perform theoretical simulations, a neural-network potential (NN-PES) was constructed for the H@Ge(111)c(2×8) system and molecular dynamics (MD) simulations were performed. Data for the NN fitting were obtained with spin-polarized DFT calculations, carried out with the Vienna Ab initio Simulation Package (VASP)[93-94] with the frozen-core all-electron projector-augmented wave (PAW) method.[77, 254] The electronic wave function was expanded using plane waves with an energy cutoff of 250 eV. The electron exchange-correlation energies were described by the Perdew−Burke−Ernzerhof (PBE) functional within the generalized gradient approximation (GGA).[222] The reconstructed Ge(111)c(2×8) surface was modeled by repeated slabs separated by a vacuum space of 16 Å in z direction. Each slab contains eight atomic layers, with four additional Ge adatoms added on top of the first layer. The Ge atoms in the bottom layer not seen by the scattering H atoms in the MD simulations were capped by Ge-H bonds. The Ge adatoms and top six layers were allowed to move while the remaining atoms were fixed throughout the calculations and there are thus a total of 101 movable atoms in the unit cell. The Brillouin zone was sampled with a 3×1×1 k-point grid. AIMD trajectories were used to provide training data for the NN fitting. The AIMD trajectories employed initial positions of the H atom randomly sampled 6 Å above the sur- face. About 100 AIMD trajectories were run for an H atom incidence energy of 0.99 eV and

1.92 eV each, with an incidence angle of 45°, and a surface temperature of 300 K, providing ~150,000 points. Additional single point DFT calculations were performed to augment the AIMD points. The data set was culled using an Euclidean distance of 0.3 Å to remove points that were too close to one another. About 26,000 points (including both energy and gradient) were finally selected to fit a 303-dimensional PES using an embedded atom neural network (EANN) approach.[86] The EANN PES obtained in this way was thoroughly tested, giving a root mean square error (RMSE) of about 80 meV/cell (or 0.8 meV/atom). MD trajectories were calculated with a modified Venus program.[255] The timesteps were chosen separately for each incidence energy, 0.1, 0.05, 0.03 and 0.01 fs for 0.37, 0.99, 1.92 and 6.17 eV, respectively.

To study non-adiabatic effects, an electron friction model was applied.[51, 54] The electronic friction coefficient was calculated based on the local-density friction approximation (LDFA).[53-54] The electron density of the Ge(111)c(2x8) surface was obtained from about 100 configurations at 300 K. To receive an analytical expression for the friction coefficient the obtained data was again fitted with the EANN method.

6.5 Extended data

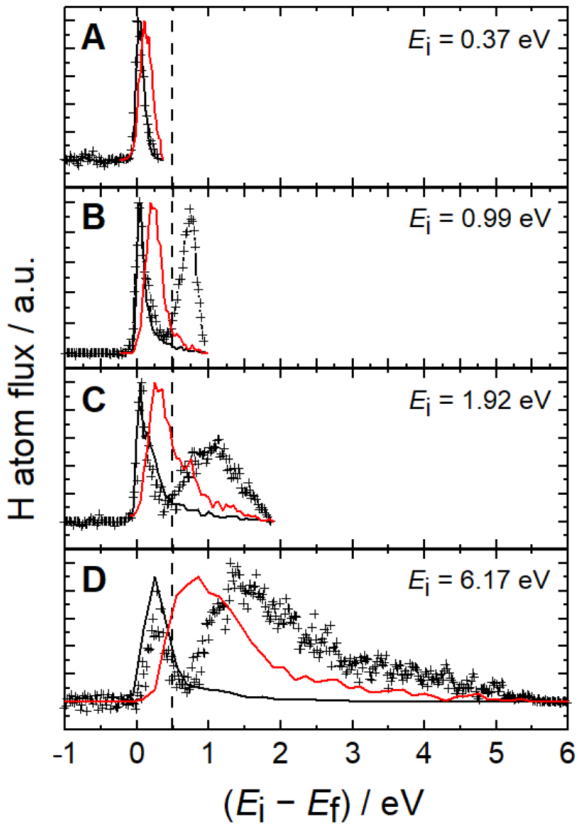

Figure E1: Comparison of molecular dynamics including electronic friction (EF) to adiabatic MD simulations and experiment. The data shown are the same as in Fig. 1 with added data 5 from MD simulations including EF (red solid lines).

CHAPTER 7

SUMMARY AND OUTLOOK

The interactions between gas molecules with solid surfaces have been the focus of experimental and theoretical studies for years. As an important carbon material, graphite serves as a useful model in studying the interaction between small gas atoms or molecules with carbon, which widely exist when aircraft reenters atmosphere. This thesis describes serval theoretical studies concerning the gas-surface dynamics on graphite surface. One project (Chapter 3) is small molecules, such as CO_2, H_2O and glycine, scattering from graphite surface. Angular and translational energy distributions of the inelastically scattered molecules were calculated and compared with experimental results. While H_2O and CO_2 retained their incident parallel energy during the gas−surface interaction, the scattering dynamics of glycine were more complicated, as a substantial fraction of the molecules exchanged a significant amount of energy during the gas−surface interaction but did not come into thermal equilibrium with the surface. The results show that the scattering dynamics are heavily dependent on the strength of molecule−surface interaction. Molecules with a stronger attraction tend to have longer residence times on the surface and consequently experience more translational energy transfer and vibrational excitation. Complex scattering dynamics, such as those observed in this study, must be considered carefully when designing a neutral-gas concentrator that can collect a variety of molecules.

Another project (Chapter 4) gains insight into the nitrogen-related gas-surface reaction dynamics on carbon-based thermal protection systems of hypersonic vehicles, we have investigated the adsorption, diffusion, and reactions of atomic nitrogen, $N(^4S)$, on the (0001) face of graphite using periodic density functional theory with a dispersion corrected functional. The

atomic nitrogen is found to bind with pristine graphite at a bridge site, with a barrier of 0.88 eV for diffusing to an adjacent bridge site. Its adsorption energy at defect sites is significantly higher, while that between graphene layers is lower. The formation of N_2 via Langmuir–Hinshelwood (LH) and Eley–Rideal (ER) mechanisms was also investigated. In the LH pathway, the recombinative desorption of N_2 proceeds via a transition state with a relatively low barrier. In addition, there is a metastable surface species, which is capable of trapping the nascent N_2 at low surface temperatures as a result of the large energy disposal into the N–N vibration. The desorbed N_2 is highly excited in both of its translational and vibrational degrees of freedom. The ER reaction is direct and fast, and it also leads to translationally and internally excited N_2. Finally, the formation of CN from a defect site is calculated to be endoergic by 2.75 eV. These results are used to rationalize the results of recent molecular beam experiments.

Although having been extensively studied both experimentally and theoretically, gas-surface dynamics are not thoroughly understood due to the complexity brought by the simple fact that the motion of nuclei and electrons cannot always be decoupled as stipulated by the Born-Oppenheimer adiabatic approximation. This thesis discusses non-adiabatic effects in O atom scattering from a graphite surface (Chapter 5). The calculated angular distribution of scattered $O(^3P)$ atoms given by adiabatic dynamics does not agree with experimental measurements. Considering the low mass number of C and thus the weak spin orbit coupling between O and graphite surface, the O atom may stay at triplet state after reaching the surface instead of switching to singlet state, which is the most stable state on surface. Because the graphite surface is a closed-shell system, by controlling the spin of the system, the spin of O atom can be fixed. We therefore constructed both the singlet and triplet potential energy surfaces (PESs) for the O+graphene system based on DFT data and carried out quasi-classical trajectory calculations on these high dimensional

PESs to explore the spin-dependent reactivity and spin-flipping dynamics. For $O(^1D)$ scattering, both experiment and theory reveal large sticking probabilities, which are attributed to the formation of a surface bound epoxide, with a ~2 eV binding energy to the surface relative to the triplet asymptote. The nascent epoxide adsorbate formed by collision of $O(^1D)$ at the surface possesses ~4 eV of vibrational energy and rapidly relaxes below the desorption asymptote. The only mechanism by which $O(^1D)$ may return to the gas phase involves a spin flip to the triplet state, which is indeed observed in the experiment. Semi-empirical dynamics simulations show that this spin flip must occur after the impinging oxygen atom dissipates a significant portion of its energy to the HOPG surface, but before it reaches thermal equilibrium. For $O(^3P)$ scattering, the fact that experimental angular and kinetic energy distributions are consistent with the theoretical simulations performed using the triplet PES allows us to conclude that triplet→singlet→triplet conversion does not readily occur at the surface during direct scattering trajectories at incidence energies around 0.34 eV. The most likely sticking mechanism involves dissipation of incidence kinetic energy on the triplet PES followed by spin relaxation to the lower singlet state on longer timescales. These observations underscore the two important factors in spin-flipping dynamics in surface chemistry, namely the efficiency of vibrational energy dissipation and strength of the spin-orbit coupling. The picture that emerges from this study is that spin-forbidden transitions do occur in this system, but with low probabilities.

The Born-Oppenheimer approximation is adequate for insulator, but fails on metal, but the effects of the electron-hole pairs can still be described by a weak frictional force representing energy transfer to the electrons successfully captures the physics of the collisions. Experimental results reveal that H atom collision with a semiconductor, Ge(111)c(2x8) surface, displays a bimodal final energy distribution. The fast component shows small energy loss and the slow one

shows significantly larger energy loss. I have performed adiabatic dynamics simulation on this system, which quantitively reproduced the fast channel with H atom direct scattering from Ge(111)c(2x8) surface (Chapter 6). Electron friction model, despite its many limitations, is one of the best ways to address non-adiabatic energy dissipation in high-dimensional gas-surface simulations. To find out the reason responsible for the slow channel, electron friction was employed to the scattering dynamics. Still the results with electron friction fail to match the slow channel in experiment. It is thus concluded that H atom collisions at the surface of a semi-conductor are capable of promoting electrons from the valance band to the conduction band with high efficiency. Our current understanding has so far not been able to explain the origin of the slow component in detail. Further experiments on H atom scattering from H-terminated Ge(111) surface yield results with one broader peak near incident energy. This reinforces our conclusion that the slow channel is due to the conducting band of the bare Ge surface.

The theoretical studies collected in this thesis focused on gas-surface dynamics, demonstrating the importance of the energy transfer process, in both adiabatic and non-adiabatic channels. While the adiabatic channel through energy exchange with surface phonons is better understood, the non-adiabatic effects which involve electronic transitions are far less understood and need to be explored. Deeper and more detailed comprehension on the adiabatic and nonadiabatic effects in gas-surface dynamics can help improve our understanding of surface chemistry. This requires collaborations between experimentalists and theorists, as demonstrated in the work discussed here.

References

1. Ertl, G., Reactions at surfaces: from atoms to complexity (Nobel lecture). *Angewandte Chemie International Edition* **2008,** *47* (19), 3524-3535.

2. Ertl, G., Dynamics of reactions at surfaces. In *Advances in catalysis*, Elsevier: 2000; Vol. 45, pp 1-69.

3. Rittmeyer, S. P.; Bukas, V. J.; Reuter, K., Energy dissipation at metal surfaces. *Advances in Physics: X* **2018,** *3* (1), 1381574.

4. Kroes, G.-J., Frontiers in surface scattering simulations. *Science* **2008,** *321* (5890), 794-797.

5. Luntz, A. C., Dynamics of Gas-Surface Interactions. *Surface and Interface Science: Solid-Gas Interfaces II* **2016,** *6*, 1255-1314.

6. Barth, J. V., Transport of adsorbates at metal surfaces: from thermal migration to hot precursors. *Surface Science Reports* **2000,** *40* (3-5), 75-149.

7. Bukas, V. J.; Reuter, K., Hot adatom diffusion following oxygen dissociation on Pd (100) and Pd (111): A first-principles study of the equilibration dynamics of exothermic surface reactions. *Physical Review Letters* **2016,** *117* (14), 146101.

8. Meyer, J.; Reuter, K., Modeling heat dissipation at the nanoscale: An embedding approach for chemical reaction dynamics on metal surfaces. *Angewandte Chemie International Edition* **2014,** *53* (18), 4721-4724.

9. Blanco-Rey, M.; Juaristi, J.; Muiño, R. D.; Busnengo, H. F.; Kroes, G.-J.; Alducin, M., Electronic friction dominates hydrogen hot-atom relaxation on Pd (100). *Physical review letters* **2014,** *112* (10), 103203.

10. Bünermann, O.; Jiang, H.; Dorenkamp, Y.; Kandratsenka, A.; Janke, S. M.; Auerbach, D. J.; Wodtke, A. M., Electron-hole pair excitation determines the mechanism of hydrogen atom adsorption. *Science* **2015,** *350* (6266), 1346-1349.

11. Jiang, B.; Guo, H., Dynamics in reactions on metal surfaces: A theoretical perspective. *The Journal of Chemical Physics* **2019,** *150* (18), 180901.

12. Nienhaus, H., Electronic excitations by chemical reactions on metal surfaces. *Surface Science Reports* **2002,** *45* (1-2), 1-78.

13. Wodtke, A. M., Electronically non-adiabatic influences in surface chemistry and dynamics. *Chemical Society Reviews* **2016,** *45* (13), 3641-3657.

14. Golibrzuch, K.; Bartels, N.; Auerbach, D. J.; Wodtke, A. M., The dynamics of molecular interactions and chemical reactions at metal surfaces: Testing the foundations of theory. *Annual review of physical chemistry* **2015,** *66*, 399-425.

15. Arnolds, H., Vibrational dynamics of adsorbates–Quo vadis? *Progress in Surface Science* **2011,** *86* (1-2), 1-40.

16. Rahinov, I.; Cooper, R.; Matsiev, D.; Bartels, C.; Auerbach, D. J.; Wodtke, A. M., Quantifying the breakdown of the Born–Oppenheimer approximation in surface chemistry. *Physical Chemistry Chemical Physics* **2011,** *13* (28), 12680-12692.

17. Hasselbrink, E., Non-adiabaticity in surface chemical reactions. *Surface science* **2009,** *603* (10-12), 1564-1570.

18. Hasselbrink, E., How non-adiabatic are surface dynamical processes? *Current Opinion in Solid State and Materials Science* **2006,** *10* (3-4), 192-204.

19. Wodtke*, A. M.; Tully, J. C.; Auerbach, D. J., Electronically non-adiabatic interactions of molecules at metal surfaces: Can we trust the Born–Oppenheimer approximation for surface chemistry? *International Reviews in Physical Chemistry* **2004,** *23* (4), 513-539.

20. Dorenkamp, Y.; Jiang, H.; Köckert, H.; Hertl, N.; Kammler, M.; Janke, S. M.; Kandratsenka, A.; Wodtke, A. M.; Bünermann, O., Hydrogen collisions with transition metal surfaces: Universal electronically nonadiabatic adsorption. *The Journal of chemical physics* **2018,** *148* (3), 034706.

21. Gu, K.; Wei, F.; Cai, Y.; Lin, S.; Guo, H., Dynamics of Initial Hydrogen Spillover from a Single Atom Platinum Active Site to the Cu (111) Host Surface: The Impact of Substrate Electron–Hole Pairs. *The Journal of Physical Chemistry Letters* **2021,** *12* (34), 8423-8429.

22. Yoder, B. L.; Bisson, R.; Beck, R. D., Steric effects in the chemisorption of vibrationally excited methane on Ni (100). *Science* **2010,** *329* (5991), 553-556.

23. Hundt, P. M.; Jiang, B.; van Reijzen, M. E.; Guo, H.; Beck, R. D., Vibrationally promoted dissociation of water on Ni (111). *Science* **2014,** *344* (6183), 504-507.

24. Juurlink, L.; Killelea, D.; Utz, A., State-resolved probes of methane dissociation dynamics. *Progress in Surface Science* **2009,** *84* (3-4), 69-134.

25. Neugebohren, J.; Borodin, D.; Hahn, H. W.; Altschäffel, J.; Kandratsenka, A.; Auerbach, D. J.; Campbell, C. T.; Schwarzer, D.; Harding, D. J.; Wodtke, A. M., Velocity-resolved kinetics of site-specific carbon monoxide oxidation on platinum surfaces. *Nature* **2018,** *558* (7709), 280-283.

26. Van Lent, R.; Auras, S. V.; Cao, K.; Walsh, A. J.; Gleeson, M. A.; Juurlink, L. B., Site-specific reactivity of molecules with surface defects—the case of H2 dissociation on Pt. *Science* **2019,** *363* (6423), 155-157.

27. Bisson, R.; Sacchi, M.; Beck, R. D., State-resolved reactivity of CH 4 on Pt (110)-(1× 2): The role of surface orientation and impact site. *The Journal of chemical physics* **2010,** *132* (9), 094702.

28. Chadwick, H.; Guo, H.; Gutiérrez-González, A.; Menzel, J. P.; Jackson, B.; Beck, R. D., Methane dissociation on the steps and terraces of Pt (211) resolved by quantum state and impact site. *The Journal of Chemical Physics* **2018,** *148* (1), 014701.

29. Gutiérrez-González, A.; Crim, F. F.; Beck, R. D., Bond selective dissociation of methane (CH3D) on the steps and terraces of Pt (211). *The Journal of Chemical Physics* **2018,** *149* (7), 074701.

30. Shakouri, K.; Behler, J. r.; Meyer, J. r.; Kroes, G.-J., Analysis of energy dissipation channels in a benchmark system of activated dissociation: N2 on Ru (0001). *The Journal of Physical Chemistry C* **2018,** *122* (41), 23470-23480.

31. Shakouri, K.; Behler, J. r.; Meyer, J. r.; Kroes, G.-J., Accurate neural network description of surface phonons in reactive gas–surface dynamics: N2+ Ru (0001). *The journal of physical chemistry letters* **2017,** *8* (10), 2131-2136.

32. Busnengo, H.; Dong, W.; Sautet, P.; Salin, A., Surface temperature dependence of rotational excitation of H 2 scattered from Pd (111). *Physical Review Letters* **2001,** *87* (12), 127601.

33. Busnengo, H. F.; Dong, W.; Salin, A., Trapping, molecular adsorption, and precursors for nonactivated chemisorption. *Physical review letters* **2004,** *93* (23), 236103.

34. Huang, Y.; Rettner, C. T.; Auerbach, D. J.; Wodtke, A. M., Vibrational promotion of electron transfer. *Science* **2000,** *290* (5489), 111-114.

35. Huang, Y.; Wodtke, A.; Hou, H.; Rettner, C.; Auerbach, D., Observation of vibrational excitation and deexcitation for NO (v= 2) scattering from Au (111): Evidence for electron-hole-pair mediated energy transfer. *Physical Review Letters* **2000,** *84* (13), 2985.

36. Li, S.; Guo, H., Monte Carlo wave packet study of negative ion mediated vibrationally inelastic scattering of NO from the metal surface. *The Journal of chemical physics* **2002,** *117* (9), 4499-4508.

37. Shenvi, N.; Roy, S.; Tully, J. C., Dynamical steering and electronic excitation in NO scattering from a gold surface. *Science* **2009,** *326* (5954), 829-832.

38. Mehta, N. A.; Murray, V. J.; Xu, C.; Levin, D. A.; Minton, T. K., Nonreactive scattering of N2 from layered graphene using molecular beam experiments and molecular dynamics. *The Journal of Physical Chemistry C* **2018,** *122* (18), 9859-9874.

39. Majumder, M.; Bhandari, H. N.; Pratihar, S.; Hase, W. L., Chemical dynamics simulation of low energy N2 collisions with graphite. *The Journal of Physical Chemistry C* **2018,** *122* (1), 612-623.

40. Zhou, L.-s.; Wang, Y.-q.; Guo, H., Dynamics studies of diglycine scattering from highly oriented pyrolytic graphite. *Chinese Journal of Chemical Physics* **2020,** *33* (2), 196-202.

41. Rettner, C.; Auerbach, D.; Lee, J., Dynamics of the formation of CD4 from the direct reaction of incident D atoms with CD3/Cu (111). *The Journal of chemical physics* **1996,** *105* (22), 10115-10122.

42. Zhou, L.; Jiang, B.; Alducin, M.; Guo, H., Communication: Fingerprints of reaction mechanisms in product distributions: Eley-Rideal-type reactions between D and CD3/Cu (111). *The Journal of Chemical Physics* **2018,** *149* (3), 031101.

43. Zhou, L.; Kandratsenka, A.; Campbell, C. T.; Wodtke, A.; Guo, H., Origin of Thermal and Hyperthermal CO2 from CO Oxidation on Platinum Surfaces: The Role of Post-Transition-State Dynamics, Active Sites, and Chemisorbed CO2. *Angewandte Chemie* **2019**.

44. Jiang, B.; Guo, H., Relative efficacy of vibrational vs. translational excitation in promoting atom-diatom reactivity: Rigorous examination of Polanyi's rules and proposition of sudden vector projection (SVP) model. *The Journal of Chemical Physics* **2013,** *138* (23), 234104.

45. Guo, H.; Jiang, B., The sudden vector projection model for reactivity: mode specificity and bond selectivity made simple. *Acc Chem Res* **2014,** *47* (12), 3679-3685.

46. Møller, K. B.; Henriksen, N. E.; Zewail, A. H., On the role of coherence in the transition from kinetics to dynamics: Theory and application to femtosecond unimolecular reactions. *The Journal of Chemical Physics* **2000,** *113* (23), 10477-10485.

47. Zener, C., Non-adiabatic crossing of energy levels. *Proceedings of the Royal Society of London. Series A, Containing Papers of a Mathematical and Physical Character* **1932,** *137* (833), 696-702.

48. Wittig, C., The landau− zener formula. *The Journal of Physical Chemistry B* **2005,** *109* (17), 8428-8430.

49. Kleyn, A. W.; Los, J.; Gislason, E. A., Vibronic coupling at intersections of covalent and ionic states. *Physics Reports* **1982,** *90* (1), 1-71.

50. Li, Y.; Wahnström, G., Nonadiabatic effects in hydrogen diffusion in metals. *Physical review letters* **1992,** *68* (23), 3444.

51. Head-Gordon, M.; Tully, J. C., Molecular dynamics with electronic frictions. *The Journal of chemical physics* **1995,** *103* (23), 10137-10145.

52. Hellsing, B.; Persson, M., Electronic damping of atomic and molecular vibrations at metal surfaces. *Physica Scripta* **1984,** *29* (4), 360.

53. Juaristi, J.; Alducin, M.; Muiño, R. D.; Busnengo, H. F.; Salin, A., Role of electron-hole pair excitations in the dissociative adsorption of diatomic molecules on metal surfaces. *Physical review letters* **2008,** *100* (11), 116102.

54. Puska, M. J.; Nieminen, R. M., Atoms embedded in an electron gas: Phase shifts and cross sections. *Physical Review B* **1983,** *27* (10), 6121.

55. Kato, K.; Uda, T.; Terakura, K., Backbond oxidation of the Si (001) surface: narrow channel of barrierless oxidation. *Physical review letters* **1998,** *80* (9), 2000.

56. Kato, K.; Uda, T., Chemisorption of a single oxygen molecule on the Si (100) surface: Initial oxidation mechanisms. *Physical Review B* **2000,** *62* (23), 15978.

57. Österlund, L.; Zoric-Acute, I.; Kasemo, B., Dissociative sticking of O 2 on Al (111). *Physical Review B* **1997,** *55* (23), 15452.

58. Yourdshahyan, Y.; Razaznejad, B.; Lundqvist, B. I., Adiabatic potential-energy surfaces for oxygen on Al (111). *Physical Review B* **2002,** *65* (7), 075416.

59. Behler, J.; Delley, B.; Lorenz, S.; Reuter, K.; Scheffler, M., Dissociation of O 2 at Al (111): The role of spin selection rules. *Physical review letters* **2005,** *94* (3), 036104.

60. Carbogno, C.; Behler, J.; Groß, A.; Reuter, K., Fingerprints for spin-selection rules in the interaction dynamics of O 2 at Al (111). *Physical review letters* **2008,** *101* (9), 096104.

61. Libisch, F.; Huang, C.; Liao, P.; Pavone, M.; Carter, E. A., Origin of the energy barrier to chemical reactions of O 2 on Al (111): Evidence for charge transfer, not spin selection. *Physical review letters* **2012,** *109* (19), 198303.

62. Katz, G.; Kosloff, R.; Zeiri, Y., Abstractive dissociation of oxygen over Al (111): A nonadiabatic quantum model. *The Journal of chemical physics* **2004,** *120* (8), 3931-3948.

63. Perdew, J. P.; Parr, R. G.; Levy, M.; Balduz Jr, J. L., Density-functional theory for fractional particle number: derivative discontinuities of the energy. *Physical Review Letters* **1982,** *49* (23), 1691.

64. Perdew, J.; McMullen, E.; Zunger, A., Density-functional theory of the correlation energy in atoms and ions: a simple analytic model and a challenge. *Physical Review A* **1981,** *23* (6), 2785.

65. Huang, C.; Pavone, M.; Carter, E. A., Quantum mechanical embedding theory based on a unique embedding potential. *The Journal of chemical physics* **2011,** *134* (15), 154110.

66. Yin, R.; Zhang, Y.; Libisch, F.; Carter, E. A.; Guo, H.; Jiang, B., Dissociative chemisorption of O2 on Al (111): dynamics on a correlated wave-function-based potential energy surface. *The journal of physical chemistry letters* **2018,** *9* (12), 3271-3277.

67. Jensen, F., *Introduction to computational chemistry*. John wiley & sons: 2017.

68. Leach, A. R.; Leach, A. R., *Molecular modelling: principles and applications*. Pearson education: 2001.

69. Senftle, T. P.; Hong, S.; Islam, M. M.; Kylasa, S. B.; Zheng, Y.; Shin, Y. K.; Junkermeier, C.; Engel-Herbert, R.; Janik, M. J.; Aktulga, H. M., The ReaxFF reactive force-field: development, applications and future directions. *npj Computational Materials* **2016,** *2* (1), 1-14.

70. Møller, C.; Plesset, M. S., Note on an approximation treatment for many-electron systems. *Physical review* **1934,** *46* (7), 618.

71. Szabo, A.; Ostlund, N. S., *Modern Quantum Chemistry: Introduction to Advanced Electronic Structure Theory*. Courier Corporation: 1996.

72. Roos, B. O.; Taylor, P. R.; Sigbahn, P. E., A complete active space SCF method (CASSCF) using a density matrix formulated super-CI approach. *Chemical Physics* **1980,** *48* (2), 157-173.

73. Thomas, L. H. In *The calculation of atomic fields*, Mathematical proceedings of the Cambridge philosophical society, Cambridge University Press: 1927; pp 542-548.

74. Hohenberg, P.; Kohn, W., Inhomogeneous electron gas. *Physical review* **1964,** *136* (3B), B864.

75. Kohn, W.; Sham, L. J., Self-consistent equations including exchange and correlation effects. *Physical review* **1965,** *140* (4A), A1133.

76. Bloch, F., Über die quantenmechanik der elektronen in kristallgittern. *Zeitschrift für physik* **1929,** *52* (7-8), 555-600.

77. Blöchl, P. E., Projector augmented-wave method. *Physical review B* **1994,** *50* (24), 17953.

78. Jönsson, J., *Electronic transitions and correlation effects: From pure elements to complex materials*. Linköping University Electronic Press: 2020; Vol. 2053.

79. Teter, M. P.; Payne, M. C.; Allan, D. C., Solution of Schrödinger's equation for large systems. *Physical Review B* **1989,** *40* (18), 12255.

80. Bylander, D.; Kleinman, L.; Lee, S., Self-consistent calculations of the energy bands and bonding properties of B 12 C 3. *Physical Review B* **1990,** *42* (2), 1394.

81. Jónsson, H.; Mills, G.; Jacobsen, K. W., Nudged elastic band method for finding minimum energy paths of transitions. **1998**.

82. Henkelman, G.; Jónsson, H., Improved tangent estimate in the nudged elastic band method for finding minimum energy paths and saddle points. *The Journal of chemical physics* **2000,** *113* (22), 9978-9985.

83. Henkelman, G.; Uberuaga, B. P.; Jónsson, H., A climbing image nudged elastic band method for finding saddle points and minimum energy paths. *The Journal of chemical physics* **2000,** *113* (22), 9901-9904.

84. Behler, J., Atom-centered symmetry functions for constructing high-dimensional neural network potentials. *The Journal of chemical physics* **2011,** *134* (7), 074106.

85. Rumelhart, D. E.; Hinton, G. E.; Williams, R. J. *Learning internal representations by error propagation*; California Univ San Diego La Jolla Inst for Cognitive Science: 1985.

86. Zhang, Y.; Hu, C.; Jiang, B., Embedded atom neural network potentials: Efficient and accurate machine learning with a physically inspired representation. *The journal of physical chemistry letters* **2019,** *10* (17), 4962-4967.

87. Daw, M. S.; Baskes, M. I., Semiempirical, quantum mechanical calculation of hydrogen embrittlement in metals. *Physical review letters* **1983,** *50* (17), 1285.

88. Daw, M. S.; Baskes, M. I., Embedded-atom method: Derivation and application to impurities, surfaces, and other defects in metals. *Physical Review B* **1984,** *29* (12), 6443.

89. Boys, S. F., Electronic wave functions-I. A general method of calculation for the stationary states of any molecular system. *Proceedings of the Royal Society of London. Series A. Mathematical and Physical Sciences* **1950,** *200* (1063), 542-554.

90. Zhu, L.; Zhang, Y.; Zhang, L.; Zhou, X.; Jiang, B., Unified and transferable description of dynamics of H 2 dissociative adsorption on multiple copper surfaces via machine learning. *Physical Chemistry Chemical Physics* **2020,** *22* (25), 13958-13964.

91. Hu, C.; Zhang, Y.; Jiang, B., Dynamics of H2O adsorption on Pt (110)-(1× 2) based on a neural network potential energy surface. *The Journal of Physical Chemistry C* **2020,** *124* (42), 23190-23199.

92. 殷蓉蓉. 开壳层分子 NO 和 O_2 的表面散射动力学理论研究. 中国科学技术大学, 2021.

93. Kresse, G.; Furthmüller, J., Efficient iterative schemes for ab initio total-energy calculations using a plane-wave basis set. *Physical review B* **1996,** *54* (16), 11169.

94. Kresse, G.; Furthmüller, J., Efficiency of *ab-initio* total energy calculations for metals and semiconductors using a plane-wave basis set. *Comput. Mater. Sci.* **1996,** *6* (1), 15-50.

95. Verlet, L., Computer" experiments" on classical fluids. I. Thermodynamical properties of Lennard-Jones molecules. *Physical review* **1967,** *159* (1), 98.

96. Haile, J. M., *Molecular dynamics simulation: elementary methods*. John Wiley & Sons, Inc.: 1992.

97. Berendsen, H. J.; Postma, J. v.; Van Gunsteren, W. F.; DiNola, A.; Haak, J. R., Molecular dynamics with coupling to an external bath. *The Journal of chemical physics* **1984,** *81* (8), 3684-3690.

98. Waite, J. H.; Lewis, W.; Kasprzak, W.; Anicich, V.; Block, B.; Cravens, T. E.; Fletcher, G.; Ip, W.-H.; Luhmann, J. G.; McNutt, R., The Cassini ion and neutral mass spectrometer (INMS) investigation. *Space Science Reviews* **2004,** *114* (1), 113-231.

99. Mahaffy, P. R.; Benna, M.; King, T.; Harpold, D. N.; Arvey, R.; Barciniak, M.; Bendt, M.; Carrigan, D.; Errigo, T.; Holmes, V., The neutral gas and ion mass spectrometer on the Mars atmosphere and volatile evolution mission. *Space Science Reviews* **2015,** *195* (1), 49-73.

100. Fenselau, C.; Caprioli, R.; Nier, A.; Hanson, W.; Seiff, A.; Mcelroy, M.; Spencer, N.; Duckett, R.; Knight, T.; Cook, W., Mass spectrometry in the exploration of Mars. *Journal of mass spectrometry* **2003,** *38* (1), 1-10.

101. Murray, V. J.; Pilinski, M. D.; Smoll Jr, E. J.; Qian, M.; Minton, T. K.; Madzunkov, S. M.; Darrach, M. R., Gas–surface scattering dynamics applied to concentration of gases for mass spectrometry in tenuous atmospheres. *The Journal of Physical Chemistry C* **2017,** *121* (14), 7903-7922.

102. Pilinski, M. D. Dynamic gas-surface interaction modeling for satellite aerodynamic computations. University of Colorado at Boulder, 2011.

103. Murray, V. J.; Xu, C.; Poovathingal, S. J.; Minton, T. K., Scattering Dynamics of Nitromethane and Methyl Formate on Highly Oriented Pyrolytic Graphite (HOPG). *The Journal of Physical Chemistry C* **2018,** *122* (28), 16178-16188.

104. Meroueh, S. O.; Wang, Y.; Hase, W. L., Direct dynamics simulations of collision-and surface-induced dissociation of N-protonated glycine. Shattering fragmentation. *The Journal of Physical Chemistry A* **2002,** *106* (42), 9983-9992.

105. Kay, B. D.; Raymond, T.; Coltrin, M. E., Observation of Direct Multiquantum Vibrational Excitation in Gas-Surface Scattering: N H 3 on Au (111). *Physical review letters* **1987,** *59* (24), 2792.

106. Wang, Y.; Hase, W. L.; Song, K., Direct dynamics study of N-protonated diglycine surface-induced dissociation. Influence of collision energy. *Journal of the American Society for Mass Spectrometry* **2003,** *14* (12), 1402-1412.

107. Andersson, M. B.; Petterson, J. B., Vibrational excitation of SF6 scattering from graphite. *Chemical physics letters* **1996,** *250* (5-6), 555-559.

108. Andersson, M. B.; Pettersson, J. B.; Marković, N., Vibrational excitation of CF3Br scattering from graphite. *Surface science* **1997,** *384* (1-3), L880-L885.

109. Liang, S.; Hemberger, P.; Neisius, N. M.; Bodi, A.; Grützmacher, H.; Levalois-Grützmacher, J.; Gaan, S., Elucidating the thermal decomposition of dimethyl methylphosphonate by vacuum ultraviolet (VUV) photoionization: pathways to the PO radical, a key species in flame-retardant mechanisms. *Chemistry–A European Journal* **2015,** *21* (3), 1073-1080.

110. Gibson, K.; Sibener, S., Scattering Dynamics, Survival, and Dispersal of Dimethyl Methylphosphonate Interacting with the Surface of Multilayer Graphene. *The Journal of Physical Chemistry A* **2016,** *120* (27), 4863-4871.

111. Rahaman, A.; Zhou, J. B.; Hase, W. L., Effects of projectile orientation and surface impact site on the efficiency of projectile excitation in surface-induced dissociation: Protonated diglycine collisions with diamond {1 1 1}. *International Journal of Mass Spectrometry* **2006,** *249*, 321-329.

112. Park, K.; Song, K.; Hase, W. L., An ab initio direct dynamics simulation of protonated glycine surface-induced dissociation. *International Journal of Mass Spectrometry* **2007,** *265* (2-3), 326-336.

113. Majumder, M.; Gibson, K.; Sibener, S. J.; Hase, W. L., Chemical dynamics simulations and scattering experiments for O2 collisions with graphite. *The Journal of Physical Chemistry C* **2018,** *122* (28), 16048-16059.

114. Head-Gordon, M.; Tully, J. C.; Rettner, C. T.; Mullins, C. B.; Auerbach, D. J., On the nature of trapping and desorption at high surface temperatures. Theory and experiments for the Ar–Pt (111) system. *The Journal of chemical physics* **1991,** *94* (2), 1516-1527.

115. Brink, G. O., Electron bombardment molecular beam detector. *Review of Scientific Instruments* **1966,** *37* (7), 857-860.

116. Daly, N., Scintillation type mass spectrometer ion detector. *Review of Scientific Instruments* **1960,** *31* (3), 264-267.

117. Weiss, I. M.; Muth, C.; Drumm, R.; Kirchner, H. O., Thermal decomposition of the amino acids glycine, cysteine, aspartic acid, asparagine, glutamic acid, glutamine, arginine and histidine. *BMC biophysics* **2018,** *11* (1), 1-15.

118. Bryan, A.; Olafsson, P., Analysis of thermal decomposition patterns of aromatic and heteroaromatic amino acids. *Analytical Letters* **1969,** *2* (10), 505-513.

119. Contarini, S.; Wendlandt, W., Thermovoltaic detection. III. Thermal decomposition of some amino acids. *Thermochimica acta* **1983,** *70* (1-3), 283-290.

120. Löfgren, P.; Krozer, A.; Lausmaa, J.; Kasemo, B., Glycine on Pt (111): a TDS and XPS study. *Surface science* **1997,** *370* (2-3), 277-292.

121. Simon, S.; Gil, A.; Sodupe, M.; Bertrán, J., Structure and fragmentation of glycine, alanine, serine and cysteine radical cations. A theoretical study. *Journal of Molecular Structure: THEOCHEM* **2005,** *727* (1-3), 191-197.

122. Van Duin, A. C.; Dasgupta, S.; Lorant, F.; Goddard, W. A., ReaxFF: a reactive force field for hydrocarbons. *The Journal of Physical Chemistry A* **2001,** *105* (41), 9396-9409.

123. Chenoweth, K.; Van Duin, A. C.; Goddard, W. A., ReaxFF reactive force field for molecular dynamics simulations of hydrocarbon oxidation. *The Journal of Physical Chemistry A* **2008,** *112* (5), 1040-1053.

124. Goverapet Srinivasan, S.; van Duin, A. C., Molecular-dynamics-based study of the collisions of hyperthermal atomic oxygen with graphene using the ReaxFF reactive force field. *The Journal of Physical Chemistry A* **2011,** *115* (46), 13269-13280.

125. Rahaman, O.; Van Duin, A. C.; Goddard III, W. A.; Doren, D. J., Development of a ReaxFF reactive force field for glycine and application to solvent effect and tautomerization. *The Journal of Physical Chemistry B* **2011,** *115* (2), 249-261.

126. Plimpton, S., Fast parallel algorithms for short-range molecular dynamics. *Journal of computational physics* **1995,** *117* (1), 1-19.

127. Logan, R. M.; Stickney, R., Simple classical model for the scattering of gas atoms from a solid surface. *The Journal of Chemical Physics* **1966,** *44* (1), 195-201.

128. Rettner, C.; Barker, J.; Bethune, D., Angular and velocity distributions characteristic of the transition between the thermal and structure regimes of gas-surface scattering. *Physical review letters* **1991,** *67* (16), 2183.

129. Ma, J.; Michaelides, A.; Alfe, D.; Schimka, L.; Kresse, G.; Wang, E., Adsorption and diffusion of water on graphene from first principles. *Physical Review B* **2011,** *84* (3), 033402.

130. Puri, B.; Walker, P., Chemistry and physics of carbon. *Chemistry and Physics of Carbon. Marcel Dekker, New York* **1970**, 191-282.

131. Kurita, T.; Okada, S.; Oshiyama, A., Energetics of ice nanotubes and their encapsulation in carbon nanotubes from density-functional theory. *Physical Review B* **2007,** *75* (20), 205424.

132. Takeuchi, K.; Yamamoto, S.; Hamamoto, Y.; Shiozawa, Y.; Tashima, K.; Fukidome, H.; Koitaya, T.; Mukai, K.; Yoshimoto, S.; Suemitsu, M., Adsorption of CO2 on graphene: a combined TPD, XPS, and vdW-DF study. *The Journal of Physical Chemistry C* **2017,** *121* (5), 2807-2814.

133. Vidali, G.; Ihm, G.; Kim, H.-Y.; Cole, M. W., Potentials of physical adsorption. *Surface Science Reports* **1991,** *12* (4), 135-181.

134. Larijani, H. T.; Ganji, M. D.; Jahanshahi, M., Trends of amino acid adsorption onto graphene and graphene oxide surfaces: a dispersion corrected DFT study. *RSC advances* **2015,** *5* (113), 92843-92857.

135. Rubes, M.; Nachtigall, P.; Vondrasek, J.; Bludsky, O., Structure and stability of the water− graphite complexes. *The Journal of Physical Chemistry C* **2009,** *113* (19), 8412-8419.

136. Raukema, A.; Dirksen, R. J.; Kleyn, A. W., Probing the (dual) repulsive wall in the interaction of O2, N2, and Ar with the Ag (111) surface. *The Journal of chemical physics* **1995,** *103* (14), 6217-6231.

137. Frenkel, J., Theorie der Adsorption und verwandter Erscheinungen. *Zeitschrift für Physik* **1924,** *26* (1), 117-138.

138. Meroueh, O.; Hase, W. L., Energy transfer pathways in the collisional activation of peptides. *International Journal of Mass Spectrometry* **2000,** *201* (1-3), 233-244.

139. Maultzsch, J.; Reich, S.; Thomsen, C.; Requardt, H.; Ordejón, P., Phonon dispersion in graphite. *Physical review letters* **2004,** *92* (7), 075501.

140. Nitzan, A.; Mukamel, S.; Jortner, J., Some features of vibrational relaxation of a diatomic molecule in a dense medium. *The Journal of Chemical Physics* **1974,** *60* (10), 3929-3934.

141. Liu, L.; Guo, H., Theoretical study of vibrational excitation of ammonia scattered from Cu. *Chemical physics* **1996,** *205* (1-2), 179-190.

142. Mahaffy, P. R.; Benna, M.; King, T.; Harpold, D. N.; Arvey, R.; Barciniak, M.; Bendt, M.; Carrigan, D.; Errigo, T.; Holmes, V.; Johnson, C. S.; Kellogg, J.; Kimvilakani, P.; Lefavor, M.; Hengemihle, J.; Jaeger, F.; Lyness, E.; Maurer, J.; Melak, A.; Noreiga, F.; Noriega, M.; Patel, K.; Prats, B.; Raaen, E.; Tan, F.; Weidner, E.; Gundersen, C.; Battel, S.; Block, B. P.; Arnett, K.; Miller, R.; Cooper, C.; Edmonson, C.; Nolan, J. T., The neutral gas and ion mass spectrometer on the Mars atmosphere and volatile evolution mission. *Space Sci. Rev.* **2015,** *195* (1), 49-73.

143. Milos, F. S.; Chen, Y. K., Ablation and thermal response property model validation for phenolic impregnated carbon ablator. *J. Spacecr. Rockets* **2010,** *47* (5), 786-805.

144. Zhluktov, S. V.; Abe, T., Viscous shock-layer simulation of airflow past ablating blunt body with carbon surface. *J. Thermophys. Heat Transf.* **1999,** *13* (1), 50-59.

145. Alba, C. R.; Greendyke, R. B.; Marschall, J., Development of a nonequilibrium finite-rate ablation model for radiating earth reentry flows. *J. Spacecraft Rockets* **2015,** *53* (1), 98-120.

146. Poovathingal, S.; Schwartzentruber, T. E.; Murray, V. J.; Minton, T. K.; Candler, G. V., Finite-rate oxidation model for carbon surfaces from molecular beam experiments. *AIAA J.* **2017,** *55* (5), 1644-1658.

147. Swaminathan-Gopalan, K.; Borner, A.; Murray, V. J.; Poovathingal, S.; Minton, T. K.; Mansour, N. N.; Stephani, K. A., Development and validation of a finite-rate model for carbon oxidation by atomic oxygen. *Carbon* **2018,** *137*, 313-332.

148. Krishna Sandeep, P.; Thomas E., S.; Timothy, M., *Air-carbon ablation model for hypersonic flight from molecular beam data*. ChemRxiv: 2020.

149. Nicholson, K. T.; Minton, T. K.; Sibener, S. J., Spatially anisotropic etching of graphite by hyperthermal atomic oxygen. *J. Phys. Chem. B* **2005,** *109* (17), 8476-8480.

150. Paci, J. T.; Upadhyaya, H. P.; Zhang, J.; Schatz, G. C.; Minton, T. K., Theoretical and experimental sudies of the reactions between hyperthermal $O(^3P)$ and graphite: Graphene-based direct dynamics and beam-surface scattering approaches. *J. Phys. Chem. A* **2009,** *113* (16), 4677-4685.

151. Morón, V.; Martin-Gondre, L.; Gamallo, P.; Sayós, R., Dynamics of the oxygen molecules scattered from the graphite (0001) surface and comparison with experimental data. *J. Phys. Chem. C* **2012,** *116* (40), 21482-21488.

152. Morón, V.; Martin-Gondre, L.; Gamallo, P.; Sayós, R., Quasiclassical trajectory dynamics study of atomic oxygen collisions on an O-preadsorbed graphite (0001) surface with a new analytical potential energy surface. *J. Phys. Chem. C* **2012,** *116* (24), 13092-13103.

153. Murray, V. J.; Marshall, B. C.; Woodburn, P. J.; Minton, T. K., Inelastic and reactive scattering dynamics of hyperthermal O and O_2 on hot vitreous carbon surfaces. *J. Phys. Chem. C* **2015,** *119* (26), 14780-14796.

154. Murray, V. J.; Smoll, E. J.; Minton, T. K., Dynamics of graphite oxidation at high temperature. *J. Phys. Chem. C* **2018,** *122* (12), 6602-6617.

155. Hariharan, S.; Majumder, M.; Edel, R.; Grabnic, T.; Sibener, S. J.; Hase, W. L., Exploratory direct dynamics Simulations of $^3O_2$ reaction with graphene at high temperatures. *J. Phys. Chem. C* **2018,** *122* (51), 29368-29379.

156. Paci, J. T.; Paci, I., Theoretical studies of the reactions between hyperthermal O(^{3}P) and Graphite: Holes and the second layer. *J. Phys. Chem. C* **2019,** *123* (49), 29647-29655.

157. Murray, V. J.; Minton, T. K., Gas-surface interactions of atomic nitrogen with vitreous carbon. *Carbon* **2019,** *150*, 85-92.

158. Murray, V. J.; Recio, P.; Caracciolo, A.; Miossec, C.; Balucani, N.; Casavecchia, P.; Minton, T. K., Oxidation and nitridation of vitreous carbon at high temperatures. *Carbon* **2020,** *167*, 388-402.

159. Nieman, R.; Spezia, R.; Jayee, B.; Minton, T. K.; Hase, W. L.; Guo, H., Exploring reactivity and product formation in N(4S) collisions with pristine and defected graphene with direct dynamics simulations. *J. Chem. Phys.* **2020,** *153* (18), 184702.

160. Murray, V. J.; Pilinski, M. D.; Smoll, E. J.; Qian, M.; Minton, T. K.; Madzunkov, S. M.; Darrach, M. R., Gas–surface scattering dynamics applied to concentration of gases for mass spectrometry in tenuous atmospheres. *J. Phys. Chem. C* **2017,** *121* (14), 7903-7922.

161. Rivero Santamaría, A.; Alducin, M.; Díez Muiño, R.; Juaristi, J. I., Ab initio molecular dynamics study of alignment-resolved O_2 scattering from highly oriented pyrolytic graphite. *J. Phys. Chem. C* **2019,** *123* (51), 31094-31102.

162. Cullis, C. F.; Yates, J. G., Reaction of carbon with nitrogen. *Trans. Faraday Soc.* **1964,** *60* (0), 141-148.

163. Goldsmith, B. R.; Sanderson, E. D.; Ouyang, R.; Li, W.-X., CO- and NO-induced disintegration and redispersion of three-way catalysts rhodium, palladium, and platinum: An ab initio thermodynamics study. *J. Phys. Chem. C* **2014,** *118* (18), 9588-9597.

164. McCarroll, B.; McKee, D. W., The reactivity of graphite surfaces with atoms and molecules of hydrogen, oxygen and nitrogen. *Carbon* **1971,** *9* (3), 301-311.

165. Park, C.; Bogdanoff, D. W., Shock-tube measurement of nitridation coefficient of solid carbon. *J. Thermophys. Heat Transf.* **2006,** *20* (3), 487-492.

166. Suzuki, T.; Fujita, K.; Ando, K.; Sakai, T., Experimental study of graphite ablation in nitrogen flow. *J. Thermophys. Heat Transf.* **2008,** *22* (3), 382-389.

167. Zhang, L.; Pejaković, D. A.; Marschall, J.; Dougherty, M.; Fletcher, D. G., Laboratory investigation of the active nitridation of graphite by atomic nitrogen. *J. Thermophys. Heat Transf.* **2012,** *26* (1), 10-21.

168. Xu, Y.-J.; Li, J.-Q., The interaction of N_2 with active sites of graphite: A theoretical study. *Chem. Phys. Lett.* **2005,** *406* (1-3), 249-253.

169. Ma, Y.; Foster, A. S.; Krasheninnikov, A.; Nieminen, R. M., Nitrogen in graphite and carbon nanotubes: Magnetism and mobility. *Phys. Rev. B* **2005,** *72* (20), 205416.

170. Zhechkov, L.; Heine, T.; Seifert, G., Physisorption of N_2 on graphene platelets: An ab initio study. *Int. J. Quant. Chem.* **2006,** *106* (6), 1375-1382.

171. Wu, M.; Liu, E.-Z.; Jiang, J. Z., Magnetic behavior of graphene absorbed with N, O, and F atoms: A first-principles study. *Applied Physics Letters* **2008,** *93* (8), 082504.

172. Rubeš, M.; Kysilka, J.; Nachtigall, P.; Bludský, O., DFT/CC investigation of physical adsorption on a graphite (0001) surface. *Phys. Chem. Chem. Phys.* **2010,** *12* (24), 6438-6444.

173. Chen, L.; Hu, H.; Ouyang, Y.; Pan, H. Z.; Sun, Y. Y.; Liu, F., Atomic chemisorption on graphene with Stone–Thrower–Wales defects. *Carbon* **2011,** *49* (10), 3356-3361.

174. Nakada, K.; Ishii, A., Migration of adatom adsorption on graphene using DFT calculation. *Solid State Commun.* **2011,** *151* (1), 13-16.

175. Li, Y.; Ren, J.-C.; Zhang, R.-Q.; Lin, Z.; Van Hove, M. A., Atomic nitrogen chemisorption on graphene with extended line defects. *J. Mater. Chem.* **2012,** *22* (39), 21167-21172.

176. Pašti, I. A.; Jovanović, A.; Dobrota, A. S.; Mentus, S. V.; Johansson, B.; Skorodumova, N. V., Atomic adsorption on graphene with a single vacancy: systematic DFT study through the periodic table of elements. *Phys. Chem. Chem. Phys.* **2018,** *20* (2), 858-865.

177. Elstner, M.; Porezag, D.; Jungnickel, G.; Elsner, J.; Haugk, M.; Frauenheim, T.; Suhai, S.; Seigert, G., Self-consistent-charge density-functional tight-binding method for simulations of complex materials properties. *Phys. Rev. B* **1998,** *58*, 7260-7268.

178. Bhimanapati, G. R.; Lin, Z.; Meunier, V.; Jung, Y.; Cha, J.; Das, S.; Xiao, D.; Son, Y.; Strano, M. S.; Cooper, V. R.; Liang, L.; Louie, S. G.; Ringe, E.; Zhou, W.; Kim, S. S.; Naik, R. R.; Sumpter, B. G.; Terrones, H.; Xia, F.; Wang, Y.; Zhu, J.; Akinwande, D.; Alem, N.; Schuller, J. A.; Schaak, R. E.; Terrones, M.; Robinson, J. A., Recent advances in two-dimensional materials beyond graphene. *ACS Nano* **2015,** *9* (12), 11509-11539.

179. Moon, S.; Hijikata, Y.; Irle, S., Structural transformations of graphene exposed to nitrogen plasma: quantum chemical molecular dynamics simulations. *Phys. Chem. Chem. Phys.* **2019,** *21* (23), 12112-12120.

180. Goverapet Srinivasan, S.; van Duin, A. C. T., Molecular-dynamics-based study of the collisions of hyperthermal atomic oxygen with graphene using the ReaxFF reactive force field. *J. Phys. Chem. A* **2011,** *115* (46), 13269-13280.

181. Mehta, N. A.; Murray, V. J.; Xu, C.; Levin, D. A.; Minton, T. K., Nonreactive scattering of N_2 from layered graphene using molecular beam experiments and molecular dynamics. *J. Phys. Chem. C* **2018,** *122* (18), 9859-9874.

182. Murray, V. J.; Zhou, L.; Xu, C.; Wang, Y.; Guo, H.; Minton, T. K., Scattering dynamics of glycine, H_2O, and CO_2 on highly oriented pyrolytic graphite. *J. Phys. Chem. C* **2019,** *123* (6), 3605-3621.

183. Zhou, L.-s.; Wang, Y.-q.; Guo, H., Dynamics studies of diglycine scattering from highly oriented pyrolytic graphite. *Chin. J. Chem. Phys.* **2020,** *33* (2), 196-202.

184. Majumder, M.; Gibson, K. D.; Sibener, S. J.; Hase, W. L., Chemical dynamics simulations and scattering experiments for O_2 collisions with graphite. *J. Phys. Chem. C* **2018,** *122* (28), 16048-16059.

185. Blöchl, P. E., Projector augmented-wave method. *Phys. Rev. B* **1994,** *50*, 17953-17979.

186. Monkhorst, H. J.; Pack, J. D., Special points for Brillouin-zone integrations. *Phys. Rev. B* **1976,** *13*, 5188-5192.

187. Kresse, G.; Furthmuller, J., Efficient iterative schemes for ab initio total-energy calculations using plane wave basis set. *Phys. Rev. B* **1996,** *54*, 11169-11186.

188. Kresse, G.; Furthmuller, J., Efficiency of ab initio total energy calculations for metals and semiconductors using plane wave basis set. *Comp. Mater. Sci.* **1996,** *6*, 15-50.

189. Perdew, J. P.; Burke, K.; Ernzerhof, M., Generalized gradient approximation made simple. *Phys. Rev. Lett.* **1996,** *77*, 3865-3868.

190. Klimeš, J.; Michaelides, A., Perspective: Advances and challenges in treating van der Waals dispersion forces in density functional theory. *J. Chem. Phys.* **2012,** *137* (12), 120901.

191. Klimeš, J.; Bowler, D. R.; Michaelides, A., Chemical accuracy for the van der Waals density functional. *J. Phys. Condens. Mat.* **2009,** *22* (2), 022201.

192. Henkelman, G.; Arnaldsson, A.; Jónsson, H., Theoretical calculations of CH_4 and H_2 associative desorption from Ni(111): Could subsurface hydrogen play an important role? *J. Chem. Phys.* **2006,** *124*, 044706.

193. Henkelman, G.; Arnaldsson, A.; Jónsson, H., A fast and robust algorithm for Bader decomposition of charge density. *Comput. Mater. Sci.* **2006,** *36* (3), 354-360.

194. Henkelman, G.; Jónsson, H., A dimer method for finding saddle points on high dimensional potential surfaces using only first derivatives. *J. Chem. Phys.* **1999,** *111* (15), 7010-7022.

195. Guo, H.; Jiang, B., The sudden vector projection model for reactivity: Mode specificity and bond selectivity made simple. *Acc. Chem. Res.* **2014,** *47* (12), 3679-3685.

196. Jiang, B.; Yang, M.; Xie, D.; Guo, H., Quantum dynamics of polyatomic dissociative chemisorption on transition metal surfaces: Mode specificity and bond selectivity. *Chem. Soc. Rev.* **2016,** *45*, 3621-3640.

197. Jiang, B.; Guo, H., Dynamics in reactions on metal surfaces: A theoretical perspective. *J. Chem. Phys.* **2019,** *150* (18), 180901.

198. Slonczewski, J. C.; Weiss, P. R., Band structure of graphite. *Phys. Rev.* **1958,** *109* (2), 272-279.

199. Ulbricht, H.; Zacharia, R.; Cindir, N.; Hertel, T., Thermal desorption of gases and solvents from graphite and carbon nanotube surfaces. *Carbon* **2006,** *44* (14), 2931-2942.

200. Smith, R. S.; May, R. A.; Kay, B. D., Desorption kinetics of Ar, Kr, Xe, N_2, O_2, CO, methane, ethane, and propane from graphene and amorphous solid water surfaces. *J. Phys. Chem. B* **2016,** *120* (8), 1979-1987.

201. Saha, D.; Nelson, K.; Chen, J.; Lu, Y.; Ozcan, S., Adsorption of CO_2, CH_4, and N_2 in micro-mesoporous nanographene: a comparative study. *J. Chem. Engin. Data* **2015,** *60* (9), 2636-2645.

202. Wei, F.; Wan, Q.; Lin, S.; Guo, H., Origin of confined catalysis in nanoscale reactors between two-dimensional covers and metal substrates: Mechanical or electronic? *J. Phys. Chem. C* **2020,** *124* (21), 11564-11573.

203. Zhou, L.; Kandratsenka, A.; Campbell, C. T.; Wodtke, A. M.; Guo, H., Origin of thermal and hyperthermal CO_2 from CO oxidation on Pt surfaces: The role of post-transition-state dynamics, active sites, and chemisorbed CO_2. *Angew. Chem. Int. Ed.* **2019,** *58* (21), 6916-6920.

204. Jackson, B.; Persson, M., A quantum-mechanical study of recombinative desorption ot atomic hydrogen on a metal surface. *J. Chem. Phys.* **1992,** *96* (3), 2378-2386.

205. Quattrucci, J. G.; Jackson, B., Quasiclassical study of Eley–Rideal and hot atom reactions of H atoms with Cl adsorbed on a Au(111) surface. *J. Chem. Phys.* **2005,** *122* (7), 074705.

206. Pétuya, R.; Larrégaray, P.; Crespos, C.; Aurel, P.; Busnengo, H. F.; Martínez, A. E., Scattering of atomic hydrogen off a H-covered W(110) surface: Hot-atom versus Eley–Rideal abstraction dynamics. *J. Phys. Chem. C* **2015,** *119* (6), 3171-3179.

207. Galparsoro, O.; Pétuya, R.; Juaristi, J. I.; Crespos, C.; Alducin, M.; Larrégaray, P., Energy dissipation to tungsten surfaces upon Eley–Rideal recombination of N_2 and H_2. *J. Phys. Chem. C* **2015,** *119* (27), 15434-15442.

208. Zhou, L.; Zhou, X.; Alducin, M.; Zhang, L.; Jiang, B.; Guo, H., Ab initio molecular dynamics study of the Eley-Rideal reaction of H + Cl–Au(111) → HCl + Au(111): Impact of energy dissipation to surface phonons and electron-hole pairs. *J. Chem. Phys.* **2018,** *148* (1), 014702.

209. Zhou, L.; Jiang, B.; Alducin, M.; Guo, H., Communication: Fingerprints of reaction mechanisms in product distributions: Eley-Rideal-type reactions between D and CD_3/Cu(111). *J. Chem. Phys.* **2018,** *149* (3), 031101.

210. Alagia, M.; Balucani, N.; Cartechini, L.; Casavecchia, P.; Van Kleef, E.; Volpi, G.; Kuntz, P.; Sloan, J., Crossed molecular beams and quasiclassical trajectory studies of the reaction O (1 D)+ H 2 (D 2). *The Journal of chemical physics* **1998,** *108* (16), 6698-6708.

211. Garton, D. J.; Minton, T. K.; Maiti, B.; Troya, D.; Schatz, G. C., A crossed molecular beams study of the O (3 P)+ H 2 reaction: comparison of excitation function with accurate quantum reactive scattering calculations. *The Journal of chemical physics* **2003,** *118* (4), 1585-1588.

212. Marian, C. M., Understanding and controlling intersystem crossing in molecules. *Annual Review of Physical Chemistry* **2021,** *72*, 617-640.

213. Cui, Q.; Morokuma, K.; Bowman, J. M.; Klippenstein, S. J., The spin-forbidden reaction CH (2 Π)+ N 2→ HCN+ N (4 S) revisited. II. Nonadiabatic transition state theory and application. *The Journal of chemical physics* **1999,** *110* (19), 9469-9482.

214. Behler, J.; Reuter, K.; Scheffler, M., Nonadiabatic effects in the dissociation of oxygen molecules at the Al (111) surface. *Physical Review B* **2008,** *77* (11), 115421.

215. Kretchmer, J. S.; Chan, G. K.-L., The fate of atomic spin in atomic scattering off surfaces. *The Journal of Physical Chemistry Letters* **2018,** *9* (11), 2863-2868.

216. Zhu, Y. F.; Gordon, R. J., The production of O (3 P) in the 157 nm photodissociation of CO2. *The Journal of chemical physics* **1990,** *92* (5), 2897-2901.

217. Quan, J.; Chang, Y.; Li, Z.; Zhao, Y.; Luo, Z.; Wu, Y.; Zhang, S.; Chen, Z.; Yang, J.; Yuan, K., A free electron laser-based 1+ 1′ Resonance-Enhanced Multiphoton Ionization scheme for rotationally resolved detection of OH radicals with correct relative intensities. *Journal of Molecular Spectroscopy* **2021,** *380*, 111509.

218. Lu, I.-C.; Huang, W.-J.; Chaudhuri, C.; Chen, W.-K.; Lee, S.-H., Development of a stable source of atomic oxygen with a pulsed high-voltage discharge and its application to crossed-beam reactions. *Review of Scientific Instruments* **2007,** *78* (8), 083103.

219. Harding, D. J.; Neugebohren, J.; Auerbach, D. J.; Kitsopoulos, T.; Wodtke, A. M., Using ion imaging to measure velocity distributions in surface scattering experiments. *The Journal of Physical Chemistry A* **2015,** *119* (50), 12255-12262.

220. Harding, D. J.; Neugebohren, J.; Hahn, H.; Auerbach, D.; Kitsopoulos, T.; Wodtke, A. M., Ion and velocity map imaging for surface dynamics and kinetics. *The Journal of Chemical Physics* **2017,** *147* (1), 013939.

221. Park, G. B.; Kitsopoulos, T. N.; Borodin, D.; Golibrzuch, K.; Neugebohren, J.; Auerbach, D. J.; Campbell, C. T.; Wodtke, A. M., The kinetics of elementary thermal reactions in heterogeneous catalysis. *Nature Reviews Chemistry* **2019,** *3* (12), 723-732.

222. Perdew, J. P.; Burke, K.; Ernzerhof, M., Generalized gradient approximation made simple. *Physical review letters* **1996,** *77* (18), 3865.

223. Incze, A.; Pasturel, A.; Chatillon, C., First-principles study of the atomic oxygen adsorption on the (0 0 0 1) graphite surface and dissolution. *Applied surface science* **2001,** *177* (4), 226-229.

224. Moron, V.; Martin-Gondre, L.; Crespos, C.; Larregaray, P.; Gamallo, P.; Sayós, R., Classical dynamics study of atomic oxygen over graphite (0 0 0 1) with new interpolated and analytical potential energy surfaces. *Computational and Theoretical Chemistry* **2012,** *990*, 132-143.

225. Moron, V.; Martin-Gondre, L.; Gamallo, P.; Sayós, R., Quasiclassical trajectory dynamics study of atomic oxygen collisions on an O-preadsorbed graphite (0001) surface with a new analytical potential energy surface. *The Journal of Physical Chemistry C* **2012,** *116* (24), 13092-13103.

226. Xu, S.; Chen, H.-L.; Lin, M.-C., Quantum chemical prediction of reaction pathways and rate constants for the reactions of O x (x= 1 and 2) with pristine and defective graphite (0001) surfaces. *The Journal of Physical Chemistry C* **2012,** *116* (2), 1841-1849.

227. Jayee, B.; Nieman, R.; Minton, T. K.; Hase, W. L.; Guo, H., Direct Dynamics Simulations of Hyperthermal O (3P) Collisions with Pristine, Defected, Oxygenated, and Nitridated Graphene Surfaces. *The Journal of Physical Chemistry C* **2021,** *125* (18), 9795-9808.

228. Murray, V. J.; Smoll Jr, E. J.; Minton, T. K., Dynamics of graphite oxidation at high temperature. *The Journal of Physical Chemistry C* **2018,** *122* (12), 6602-6617.

229. Even, U.; Jortner, J.; Noy, D.; Lavie, N.; Cossart-Magos, C., Cooling of large molecules below 1 K and He clusters formation. *J. Chem. Phys.* **2000,** *112* (18), 8068-8071.

230. Bamford, D. J.; Jusinski, L. E.; Bischel, W. K., Absolute two-photon absorption and three-photon ionization cross sections for atomic oxygen. *Phys. Rev. A* **1986,** *34* (1), 185-198.

231. Pratt, S. T.; Dehmer, P. M.; Dehmer, J. L., Double-resonance spectroscopy of transitions between autoionizing levels of atomic oxygen. *Phys. Rev. A* **1991,** *43* (9), 4702-4711.

232. Gebhardt, C. R.; Rakitzis, T. P.; Samartzis, P. C.; Ladopoulos, V.; Kitsopoulos, T. N., Slice imaging: A new approach to ion imaging and velocity mapping. *Rev. Sci. Instrum.* **2001,** *72* (10), 3848-3853.

233. Harding, D. J.; Neugebohren, J.; Auerbach, D. J.; Kitsopoulos, T. N.; Wodtke, A. M., Using Ion Imaging to Measure Velocity Distributions in Surface Scattering Experiments. *J. Phys. Chem. A* **2015,** *119* (50), 12255-12262.

234. Kresse, G.; Furthmüller, J., Efficient iterative schemes for *ab initio* total-energy calculations using a plane-wave basis set. *Phys. Rev. B* **1996,** *54* (16), 11169-11186.

235. Perdew, J. P.; Burke, K.; Ernzerhof, M., Generalized Gradient Approximation Made Simple. *Phys. Rev. Lett.* **1996,** *77* (18), 3865-3868.

236. Blöchl, P. E., Projector augmented-wave method. *Phys. Rev. B* **1994,** *50* (24), 17953-17979.

237. Matsumi, Y.; Shafer, N.; Tonokura, K.; Kawasaki, M.; Huang, Y. L.; Gordon, R. J., Doppler profiles and fine-structure branching ratios of $O(^3P_j)$ from photodissociation of carbon dioxide at 157 nm. *J. Chem. Phys.* **1991,** *95* (10), 7311-7316.

238. Stolow, A.; Lee, Y. T., Photodissociation dynamics of CO_2 at 157.6 nm by photofragment-translational spectroscopy. *J. Chem. Phys.* **1993,** *98* (3), 2066-2076.

239. Tully, J. C., Perspective on "zur quantentheorie der molekeln". *Theoretical Chemistry Accounts* **2000,** *103* (3), 173-176.

240. Bünermann, O.; Kandratsenka, A.; Wodtke, A. M., Inelastic scattering of H atoms from surfaces. *The Journal of Physical Chemistry A* **2021,** *125* (15), 3059-3076.

241. Hertl, N.; Kandratsenka, A.; Bünermann, O.; Wodtke, A. M., Multibounce and Subsurface Scattering of H Atoms Colliding with a van der Waals Solid. *The Journal of Physical Chemistry A* **2021,** *125* (26), 5745-5752.

242. Jiang, H.; Kammler, M.; Ding, F.; Dorenkamp, Y.; Manby, F. R.; Wodtke, A. M.; Miller III, T. F.; Kandratsenka, A.; Bünermann, O., Imaging covalent bond formation by H atom scattering from graphene. *Science* **2019,** *364* (6438), 379-382.

243. Wille, S.; Jiang, H.; Bünermann, O.; Wodtke, A. M.; Behler, J.; Kandratsenka, A., An experimentally validated neural-network potential energy surface for H-atom on free-standing graphene in full dimensionality. *Physical Chemistry Chemical Physics* **2020,** *22* (45), 26113-26120.

244. Jiang, H.; Tao, X.; Kammler, M.; Ding, F.; Wodtke, A. M.; Kandratsenka, A.; Miller III, T. F.; Bünermann, O., Small nuclear quantum effects in scattering of H and D from graphene. *The Journal of Physical Chemistry Letters* **2021,** *12* (7), 1991-1996.

245. Jiang, H.; Dorenkamp, Y.; Krüger, K.; Bünermann, O., Inelastic H and D atom scattering from Au (111) as benchmark for theory. *The Journal of Chemical Physics* **2019,** *150* (18), 184704.

246. Kandratsenka, A.; Jiang, H.; Dorenkamp, Y.; Janke, S. M.; Kammler, M.; Wodtke, A. M.; Bünermann, O., Unified description of H-atom–induced chemicurrents and inelastic scattering. *Proceedings of the National Academy of Sciences* **2018,** *115* (4), 680-684.

247. Amirav, A.; Cardillo, M. J., Electron-hole pair creation by atomic scattering at surfaces. *Physical review letters* **1986,** *57* (18), 2299.

248. Amirav, A.; Lambert, W.; Cardillo, M.; Trevor, P.; Luke, P.; Haller, E., Electron-hole pair creation at a Ge (100) surface by ground-state neutral Xe atoms. *Journal of applied physics* **1986,** *59* (6), 2213-2215.

249. Weiss, P.; Amirav, A.; Trevor, P.; Cardillo, M., Hyperthermal gas–surface scattering. *Journal of Vacuum Science & Technology A: Vacuum, Surfaces, and Films* **1988,** *6* (3), 889-894.

250. Chadi, D.; Chiang, C., New c− 2× 8 unit cell for the Ge (111) surface. *Physical Review B* **1981,** *23* (4), 1843.

251. Feenstra, R. M.; Lee, J.; Kang, M.; Meyer, G.; Rieder, K., Band gap of the Ge (111) c (2× 8) surface by scanning tunneling spectroscopy. *Physical review B* **2006,** *73* (3), 035310.

252. Bünermann, O.; Jiang, H.; Dorenkamp, Y.; Auerbach, D. J.; Wodtke, A. M., An ultrahigh vacuum apparatus for H atom scattering from surfaces. *Review of Scientific Instruments* **2018,** *89* (9), 094101.

253. Schnieder, L.; Seekamp-Rahn, K.; Liedeker, F.; Steuwe, H.; Welge, K., Hydrogen exchange reaction H+ D 2 in crossed beams. *Faraday Discussions of the Chemical Society* **1991,** *91*, 259-269.

254. Kresse, G.; Joubert, D., From ultrasoft pseudopotentials to the projector augmented-wave method. *Physical review b* **1999,** *59* (3), 1758.

255. Hase, W. L.; Duchovic, R. J.; Hu, X.; Komornicki, A.; Lim, K. F.; Lu, D.-h.; Peslherbe, G. H.; Swamy, K. N.; Linde, S. V.; Varandas, A., A general chemical dynamics computer program. *QCPE* **1996,** *16*, 671.